Memory Effects in the Permeation of Molecules through Lipid Bilayers

am Fachbereich Physik der Freien Universität Berlin
eingereichte Dissertation

zur Erlangung des akademischen Grades
eines Doktors der Naturwissenschaften (Dr. rer. nat.)

vorgelegt von

Bartosz G. Kowalik

Berlin, Januar 2018

1. Gutachter / Betreuer:

Prof. Dr. Roland R. Netz
Freie Universität Berlin
Fachbereich Physik
Arnimallee 14
D-14195 Berlin

2. Gutachter:

Prof. Dr. Felix Höfling
Freie Universität Berlin
Fachbereich Mathematik und Informatik
Arnimallee 6
D-14195 Berlin

Tag der Disputation: 17.09.2018

Contents

Chapter 1

Introduction

In order to maintain their metabolism, cells require mechanisms for the transport of molecules through their outermost layers, which for the majority of cells consist of lipid bilayers with embedded proteins [1]. These bilayers constitute a barrier which keeps molecules that are crucial for the function of the cell inside and toxic molecules outside the cell, but on the other hand, allow other molecules, which are metabolized by the cells, to pass into the cell interior. Thus, lipid bilayers have to be selective permeable membranes [2]. Depending on their properties, molecules pass through a lipid bilayer by three different mechanisms: Large molecules are transported into cells via endocytosis [3], where the lipid bilayer actively engulfs the molecules such that they become incorporated into a lipid vesicle (phagosome), which then enters the cell interior. Ions [4] and medium-sized, polar molecules like amino acids [5] are actively pumped through channel proteins which are integrated in the lipid bilayer. Small, uncharged molecules like oxygen or carbon dioxide can diffuse passively through the membrane [6]. Thus, for any living cell, the permeability of lipid membranes is a key parameter which controls the rate at which these small molecules are exchanged with the environment outside the cell.

The permeability of lipid bilayers is determined by their structure: The vast majority of lipid bilayers in human cells contain high fractions of phospholipids, which consist of two hydrophobic hydrocarbon chains and a polar headgroup [7]. The interaction of the hydrocarbon chains with water is unfavorable compared to the interaction of chains with each other, which causes lipids to aggregate such that the chains are separated from water [8]. Depending on parameters like the lipid concentration in water or temperature, lipids assemble to micelles, bilayers or more complicated structures like hexagonal lattices [9, 10]. Structures which consist of water enclosed by lipid bilayers are called vesicles and are speculated to be predecessors of the first cells [11]. In cells, the lipid bilayers incorporate proteins, which for example function as surface receptors [12, 13] or control the adhesion of the cell to surfaces or other cells [14]. Regarding the numerous tasks they fulfill, it becomes clear why the formation of lipid bilayers is widely regarded as being a key factor for the development of life [15, 16].

Even within bilayers, lipids can adopt various phases depending on the pressure, temperature and lipid composition [9]. Another important quantity that influences the lipid phase

of bilayers is the thickness of the water layer between them, which is called hydration level [17]. The lipid phases are characterized by the ordering of the chains and the headgroups and differ by their lateral lipid mobility, bilayer flexibility or area per lipid [18]. The transitions between the phases have been measured in experiments [19, 20] and modeled theoretically [21–23], which resulted in well-understood phase diagrams. Two phases of major physiological relevance are the gel (L_β) phase, which is mainly found in human skin [24], and the fluid (L_α) phase, which is assumed by most membranes inside the human body [1]. In the gel phase, the hydrocarbon chains exhibit a distorted-hexagonal ordering with the dihedral angles between their carbon atoms predominantly adopting a trans configuration [25], whereas in the fluid phase, the chains are disordered with a high density of gauche dihedrals. The increased order inside bilayers in the gel phase compared to the fluid phase leads to a lower lateral diffusivity of the lipids and a higher permeation resistance for molecules [26], which is essential for the barrier function of the lipid matrix of the outermost skin layer, the stratum corneum [27]. The investigation of differences and similarities in structure, dynamics and interactions between gel and fluid membranes is thus of primary importance for the understanding of diffusion processes through skin, and in particular for transdermal drug delivery [28, 29].

In order to obtain a complete picture of permeation processes through membranes, also a theoretical framework is necessary, which yields a connection to the field of statistical physics. The first attempts to understand permeation processes resulted in the homogeneous solubility–diffusion model [30, 31], where a solute first dissolves from the water phase into the membrane, then diffuses through the membrane and finally enters the water phase on the other side. In this model, only two parameters enter, which are the partition coefficient of the solute between the water phase and the membrane and the diffusion coefficient of the solute inside the membrane. The numerical values of these two quantities are taken from measurements of the solubility and diffusion of the solute in liquid alkanes, thus the membrane is assumed to be an alkane wall. Although being very simple, already this model was able yield to quantitative agreement with experiments in some cases [32]. A further step was made by the assumption that the diffusivity and the free energy are not constant, but exhibit maxima and minima inside the membrane, and the permeability of a membrane then results as an integral over the diffusivity and free energy profiles [33]. With the emergence of powerful computers, simulations made it possible to investigate the permeation process in molecular detail and compute these profiles for a series of solutes [34–37]. The extraction of the profiles from the solute trajectories creates the link between molecular biology and statistical physics.

The modeling of the time evolution of dynamic variables in a system with a large number of degrees of freedom, which in this work is the motion of a solute through a lipid bilayer, marks a central problem in the field of statistical physics. Starting from a many particle system whose microscopic dynamics satisfy the principles of Hamiltonian mechanics, the main idea of solving this task is the reduction of the number of degrees of freedom. This leads to a description where only the dynamic variables of interest appear explicitly and the influence of all other degrees of freedom is projected onto effective friction and noise

terms. In the simplest case, this projection yields the one-dimensional Langevin equation [38–40]

$$m\ddot{x}(t) = -\frac{k_B T}{D}\dot{x}(t) - \nabla U(x(t)) + F_R(t)\,. \tag{1.1}$$

This equation is a stochastic differential equation for single particle trajectories $x(t)$ including an external potential $U(x)$ and assuming a constant diffusivity D and temperature T. The coupling of the dynamics of the particle to its environment is accomplished by the random force $F_R(t)$, which is the sum of the forces on the particle from all other degrees of freedom. The Langevin equation, as it is formulated in Eq. 1.1, is based on the assumption that the time scale, on which the correlation function of the random force $F_R(t)$ decays, is much smaller than the time scale of the particle dynamics. Furthermore, the amplitude of the correlation of $F_R(t)$ is related to the diffusivity D, which is the main statement of the fluctuation-dissipation theorem [41]:

$$\langle F_R(t) F_R(t')\rangle = 2k_B T\gamma\delta(t-t')\,, \tag{1.2}$$

where $\delta(t)$ is the Dirac delta-function and γ is the friction coefficient $\gamma = k_B T/D$. In 1965, Mori considered a system without the separation of time scales between the dynamics of the particles and the environment [42], which led to the formulation of the generalized Langevin equation

$$m\ddot{x}(t) = -\int_0^t \mathrm{d}t'\,\Gamma(t')\dot{x}(t-t') - \nabla U(x(t)) + F_R(t)\,. \tag{1.3}$$

In this equation, retardation effects in the interactions between the particle and its environment are taken into account by the memory kernel $\Gamma(t)$. The diffusion constant D then results from the integral $k_B T/D = \int_0^\infty \mathrm{d}t\;\Gamma(t)$. As a consequence of the finite time scales which occur in the dynamics of the environment, also the random force has a finite correlation time and is related to the memory kernel via

$$\langle F_R(t) F_R(t')\rangle = k_B T\Gamma(t-t'). \tag{1.4}$$

The generalized Langevin equation has been applied to various problems in physics, for example the scattering of gas molecules at solid surfaces [43] or polymer dynamics [44]. Obviously, also a lipid bilayer constitutes a system which demands the introduction of memory into the dynamics of the solute particle, since the dynamics within a lipid bilayer covers a huge span of time scales from picoseconds to microseconds [45].

In this work, we will apply the Langevin formalism with memory to the trajectories of water molecules in lipid bilayers obtained from molecular dynamics simulations in order to compute the permeability of the membranes. As the permeability strongly depends on the phase of the bilayer, we begin in Chapter 2 with the characterization of interactions between hydrated membranes in the gel and fluid phase. In Chapter 3 we investigate the influence of confining potentials on the memory kernels of solutes in liquids. The techniques developed there are then used in Chapter 4 to compute the diffusivity of water in Dipalmitoylphosphatidylcholine (DPPC) membranes, where we explicitly consider memory effects.

1.1 Hydration Repulsion

An important property of hydrated lipid bilayers is their mutual repulsion at distances in the nanometer range. This so-called hydration repulsion, which was first discussed by Langmuir in 1938 [46], universally acts between all kinds of lipid membranes, thus ensuring a lubrication of cells at pressures up to the kilobar regime [47]. The hydration repulsion is quantified in pressure–distance curves, where the water layer thickness between the membranes is measured as a function of the applied pressure, which is either osmotic or mechanical [48, 49]. In general, an exponential relation between the pressure and the membrane separation is found, with decay lengths in the range from 0.1 nm to 0.4 nm [50–52]. Although a large amount of experimental data exists for various bilayer systems [48, 53], the actual mechanism was under debate until very recently, with several theoretical concepts that served as a possible explanation [54–56]. In the last years, molecular dynamics (MD) simulations provided insight into this question and indicated that it is an interplay of entropic and enthalpic forces that results in the hydration repulsion [57, 58], however not all details have been settled yet. The investigation of hydration forces in systems, which only differ by their lipid phase, paves the way for the in-depth understanding of membrane interactions, since the chemical surface composition of these system is identical. This allows for a separation of their influence on the hydration repulsion from other factors.

In Chapter 2 we review all experimental data for the hydration repulsion between DPPC bilayers in the gel and the fluid phase, which is a common lipid in the human tissue [59]. In order to quantify the membrane separation, the repeat distance D_r, which is the sum of the water layer thickness D_w and the lipid membrane thickness D_l, is measured by scattering experiments. Both D_w and D_l cannot be measured directly, hence a theoretical model for the bilayer thickness D_l under applied pressure is required to determine D_w. Since in literature these models differ from each other, no standard definition of D_w has been established, which results in inconsistent pressure–distance curves [60]. Therefore we first back-transform the experimental data into a representation of the pressure p as a function of the repeat distance D_r, which is the sum of the bilayer thickness and D_w. In a next step, we perform atomistic MD simulations of such hydrated bilayer systems in both phases and measure the hydration pressure at constant chemical potential [57, 58]. Using an unique transformation from D_r to D_w for all experiments, which is consistent with the definition via the Gibbs dividing surface in our simulations, we compare our results to the experiments. In order to gain insight into the underlying mechanism of the hydration repulsion, we then decompose the hydration pressure p into a direct membrane–membrane interaction p_dir and an indirect water-mediated interaction p_ind. The results of the decomposition are then discussed in the scope of the theoretical models found in literature.

1.2 Friction and Memory in Confinement

The Langevin equation in Eq. 1.3 is based on the assumption that the memory kernel $\Gamma(t)$, and thus the diffusivity D, is independent of the position x and the potential $U(x)$. If this equation is used to model the dynamics of a particle in an inhomogeneous system

with a position-dependent diffusivity $D(x)$, as it the case in a lipid bilayer, a confining potential $U(x)$ has to be applied to the particle such that the variation of $D(x)$ within the potential is negligible. In earlier MD simulation studies, this has been accomplished by completely restraining the particle dynamics during the computation of the diffusivity via Eq. 1.2 [34–36]. The investigation of the dynamics of molecules in confinement is not restricted to simulations: For example the dynamics of interfacial water at proteins or membranes is influenced by an interaction potential, leading to the formation of solvation shells or layers [61, 62]. This makes the effect of confining potentials on the diffusivity worth being analyzed in detail both from a methodological as well as physical point of view.

In Chapter 3 we measure the friction coefficient γ for five molecules (methane, water, Na^+, Na^- and glycerol) in water, which are subject to harmonic potentials of varying stiffness. We discuss the dependence of the friction on the potential stiffness on the basis of the memory kernels of the solutes, which are extracted from the solute trajectories via a modified iterative scheme based on the method of Berne et al. [63]. For the glycerol molecule as solute, we increase the viscosity of the solvent by replacing water with three different water–glycerol mixtures. This leads to a magnification of the confinement-dependence of the friction, which we explain by comparing the time scales of the solute motion with the time scales of the solvent relaxation.

1.3 Permeation of Water through a Lipid Bilayer

Since in general particle fluxes are too small to be measured directly in MD simulations, it is necessary to relate the permeability to quantities which can be extracted from such simulations. From the diffusion equation it can be deduced that the permeability P is given by [33]

$$\frac{1}{P} = \int_{z_1}^{z_2} \mathrm{d}z \, \frac{\mathrm{e}^{\Delta\mathcal{F}(z)/k_\mathrm{B}T}}{D(z)}\,, \tag{1.5}$$

where $\Delta\mathcal{F}(z)$ is the free energy profile and $D(z)$ is the diffusivity profile of the membrane. The upper and lower boundary of the membrane, z_1 and z_2, are chosen such that they are located in the water phase outside the membrane. This equation has been applied in various studies to determine the permeation coefficient of solutes through membranes [34–37]. For water molecules it was shown that the permeation barrier is mainly due to the free energy $\mathcal{F}(z)$, which exhibits a pronounced maximum in the membrane center, while the diffusion profile $D(z)$ only yields a minor contribution to this barrier.

In Chapter 4, we perform MD simulation of water molecules in DPPC bilayers and implement our technique introduced in Chapter 3 to compute the memory kernels $\Gamma(t)$ of both the transversal and lateral water dynamics. Following a quantitative analysis of the long time behavior of the mean-squared displacements in lateral direction, we develop a model for the long time behavior of $\Gamma(t)$, which is then integrated to obtain the diffusivity D. By comparing this result to the diffusivity profile computed from round-trip times, a method

derived on the basis of the memoryless Fokker-Planck equation [64, 65], and to literature [34, 35], we study how the consideration of memory affects the diffusion coefficient of water molecules inside the membrane. This is followed by an analysis of the contributions of the free energy and the diffusivity to the permeation resistance of lipid bilayers.

Chapter 2

Characterization of Hydration Interactions between Lipid Membranes in Gel and Fluid Phase

Bibliographic information: Parts of this chapter have previously been published. Reprinted with permission from Ref. i. Copyright 2017 American Chemical Society.

2.1 Introduction

Even electrically neutral polar surfaces repel in water and exhibit for small separations, when the last water layers are removed, a repulsive force that is commonly called hydration force [55]. The mechanism behind this force and even its name are intensely debated [67]; what is generally acknowledged, however, is that it is ubiquitous and acts between self-assembled membranes and surfactant layers [50], colloids [68], clays and biomolecules such as DNA [69] and proteins [70]. Hydration forces are thus important for diverse processes such as membrane fusion and adhesion [71], soap bubble stability, protein adsorption [72] as well as lubrication of biological [73] and synthetic materials [74].

Different concepts were invoked to rationalize hydration forces. As early discussed by Langmuir [46], an effective surface repulsion was suggested to arise from the removal of strongly bound hydration layers, hence the name hydration force (to which we stick for historic reasons without reference to the implied mechanism). The overlap of water ordering profiles at two opposing surface was theoretically shown to produce an exponentially decaying repulsion [54, 75] and reasoned to explain the universality of hydration forces observed for different surfaces [55]. On the other hand, the presence of oscillatory forces between stiff surfaces measured with the surface-force apparatus [76], and in particular the huge spectrum of observed hydration force amplitudes and decay lengths for different surfaces, was used to argue that additional, direct surface interactions (encompassing entropic effects due to the perturbation of conformational surface degrees of freedom) must play an equally important role for small surface separations [56].

Historically, experiments on lipid bilayers for several reasons played a pivotal role: For given lipid chemistry and temperature, and in the absence of cosolutes, the self-assembled bilayer structure uniquely depends on a single parameter, namely the mixing ratio of water and lipids, thereby excluding ambiguities related to different preparations or compositions as for most solid surfaces. Besides, for neutral lipids there is no need to subtract the electrostatic double-layer repulsion, a procedure which adds significant arbitrariness to the definition of the hydration force for charged surfaces [77]. In addition, osmotic stress techniques allow to measure the repeat distance in a multilamellar stack as a function of the imposed osmotic pressure with high precision and over a vast range of pressures [78]. Finally, the presence of many surfaces dilutes contaminations and increases accuracy due to the parallel detection of multiple repeat distances in one measurement. As a matter of fact, supported bilayers exhibit similar hydration forces as free bilayer stacks [79], demonstrating that undulation forces (which are suppressed for supported bilayers) are negligible for small bilayer separations and only become important at large separations near the swelling limit [80, 81].

However, one of the key experiments on phospholipid bilayers led to puzzling results, which still severely hampers the complete understanding of hydration forces. Phospholipid membranes display a main transition from an ordered gel-like state at low temperature to a disordered fluid state at high temperature, which is well studied due to its physiological relevance [7, 82, 83]. The chemical surface composition does not change during this transition, only the surface structure; the comparison of hydration forces in the gel and fluid states is thus of paramount importance since it should allow to decide whether direct surface interactions or water ordering, the latter presumably being similar in the gel and fluid states, are the dominating contributor to hydration forces. The first experimental study indeed yielded different hydration force curves as a function of surface separation in the gel and fluid states, suggesting that hydration forces are not solely caused by water effects [48]. However, later experiments with the same phospholipid gave dissonant results [84–86]. It was early on suggested that this comes from different definitions of the interface position between water and bilayers used in the analysis of the experimental data [60], but this was never settled.

In this paper we first demonstrate that all five published experimental hydration pressure curves for Dipalmitoylphosphatidylcholine (DPPC), some of which in the gel and some in the fluid state, are consistent when plotted as a function of the bilayer repeat distance D_r, which is the primary quantity measured in scattering experiments. For this we undo the conversion of experimentally measured repeat distances D_r to reported surface separations, for which different definitions have been used. We then convert D_r to the water slab thickness D_w using the thermodynamic definition of the Gibbs dividing surface. We next show that the experimental data quantitatively agree with simulations of DPPC bilayers performed at low temperature in the gel state and at high temperature in the fluid state when plotted as a function of D_w. This comparison reveals that not only the pressure amplitudes but also the decay lengths are vastly different in the gel and fluid states, hinting that hydration forces are not solely caused by water ordering effects. Finally, and most importantly, further analysis of the simulation results shows that the total interaction pressure results from the near cancellation of attractive direct membrane–membrane

interaction and repulsive indirect interaction, the latter being comprised of water–water and water–membrane interactions. Curiously, direct and indirect interactions have almost the same magnitude, both in the gel and the fluid states, and for separations $D_w > 1$ nm exhibit similar exponential decay lengths of about $\lambda \approx 0.2$ nm. The sum of direct and indirect forces, which together make up what is called the hydration force, is smaller than both direct and indirect force by a factor of roughly ten. The hydration force decay length turns out to be $\lambda_{gel} \approx 0.2$ nm in the gel and $\lambda_{fluid} \approx 0.4$ nm in the fluid state. Thus, the hydration force cannot be explained by water-ordering or direct surface–surface interactions alone, simply because it is the sum of these two competing contributions of almost equal magnitude. Due to the near-cancellation of the direct and indirect contributions, the resulting hydration force depends on fine details of both contributions in a very subtle manner. It comes at no surprise that the hydration force behaves very differently from these contributions, both in terms of its amplitude but also in terms of its range (i.e., its exponential decay length). This should be kept in mind when trying to explain hydration forces in terms of simple theoretical concepts (which typically consider only one part of the problem) and is vividly demonstrated by the deviating hydration forces in the gel and fluid states.

2.2 Results

In Fig. 2.1 (a) we reproduce all available experimental data [48, 84–86] for the osmotic pressure p of DPPC multilamellar stacks as a function of the published water slab thickness D_w in a log–lin representation, two data sets correspond to the gel state (squares) and three to the fluid state (crosses). Most strikingly, different data sets in the gel and fluid states disagree among each other, as was noted before [87], and give rise to significantly different decay lengths $\lambda_{gel} = 0.11$ nm, 0.18 nm and $\lambda_{fluid} = 0.18$ nm, 0.22 nm, 0.26 nm (indicated by straight lines, see Table 2.1 in Sec. 2.4.2) as extracted from fits to a single exponential $p = p_0 e^{-D_w/\lambda}$. Thus, while the decay lengths in the gel and fluid states differ, the inconsistencies among different experiments preclude any interpretation of these results.

In fact, different experiments used different methods to convert the experimentally measured lamellar repeat distance D_r, which is the sum of the water slab thickness D_w and the lipid membrane thickness D_l, to the water slab thickness D_w: In one method, D_w is derived from the known lipid–water mixing ratio and assuming water and lipids to be incompressible [48]. In a different treatment the lipid membrane thickness D_l is determined from electron density profiles derived from X-ray diffraction and from that $D_w = D_r - D_l$ is computed. In the third treatment D_w follows from the bilayer area compressibility on the basis of D_l at one reference pressure [85, 86] (see Sec. 2.4.3 for details on the different conversion methods).

In Fig. 2.1 (b) we present the same experimental pressure data as a function of the lamellar repeat distance D_r. Note that in one case the $p(D_r)$ data was not given in the original publication [48], so we converted the data from D_w to D_r. We also include microcalorimetry data [88] that reports the osmotic pressure p as a function of the water–lipid ratio. Excellent

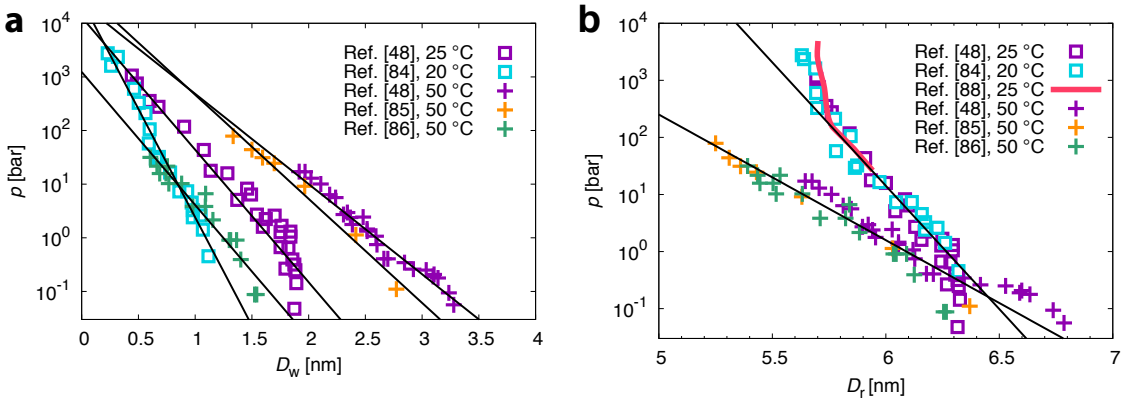

FIGURE 2.1: **Experimental osmotic pressure data for DPPC multilamellar stacks.** (**a**), Pressure data for DPPC in the gel (squares) and fluid (crosses) states as a function of the reported water slab thickness D_w. Black lines indicate exponential fits. (**b**), Pressures as a function of the reconstructed lamellar repeat distance D_r. Black lines represent exponentials with decay lengths $\lambda_{fluid} = 0.20$ nm and $\lambda_{gel} = 0.10$ nm.

agreement between all available experimental data is observed, which endorses that multilamellar systems constitute exceptionally robust experimental systems. We conclude that deviations between experiments in Fig. 2.1 (a) are indeed caused by different conversion methods used to derive D_w from the experimentally measured repeat distance D_r. Clearly, for pressures below 500 bars Fig. 2.1 (b) suggests an exponential pressure decay versus D_r with decay lengths that are very different in the gel and fluid states, $\lambda_{gel} = 0.10$ nm and $\lambda_{fluid} = 0.20$ nm (indicated by black lines), whereas in the gel phase for pressures above 500 bars the experimental data deviate from single exponential, as was noted before [88]. Whenever we fit single exponentials to experimental and simulation data, we do not imply that hydration pressures are in fact purely exponential, we rather intend to quantify the decay of the hydration pressure in simple terms.

Actually, the membrane thickness D_l depends sensitively on pressure, reflected by the fact that the relation between D_r and D_w is highly non-linear (see Sec. 2.4.3). The function $p(D_r)$ in Fig. 2.1 (b) includes hydration force and membrane compression effects, only the function $p(D_w)$ corresponds to the hydration force per se, which thus requires careful definition of D_w.

Molecular dynamics (MD) simulations are able to accurately model hydrated bilayer systems [89] and thus became an eminent tool for connecting theory with experiment [90]. A major difficulty for the investigation of the hydration repulsion is the fixed chemical potential of water, which is solved either by explicitly simulating a large water reservoir [91] or by grand–canonical simulations [91–93], however at the expense of large computation resources. The recently developed thermodynamic extrapolation method [57] allows us to efficiently perform simulations at prescribed chemical potential and thus to obtain the interaction forces between membranes with high precision, both in the fluid and in the gel state. Due to the finite size of our simulation box, which in lateral directions typically measures 4 nm, our atomistic MD simulations do not account for membrane undulations with wave lengths larger than approximately 4 nm, thus the repulsive undulation force is reduced in our simulation setup. However, the undulation force has been shown to

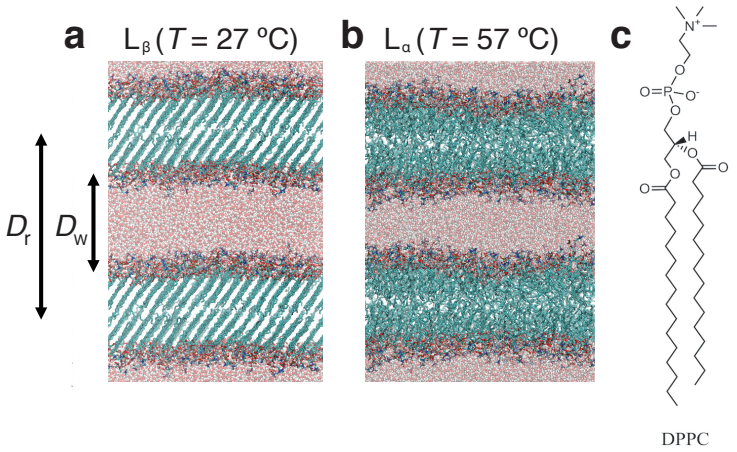

FIGURE 2.2: **Simulation setup.** Simulation snapshots of a DPPC lipid bilayer in the (**a**) gel L_β phase at $D_r = 6.28$ nm and $D_w = 1.85$ nm and in the (**b**) fluid L_α phase at $D_r = 5.19$ nm and $D_w = 1.48$ nm. The simulation box contains one periodically replicated hydrated bilayer, which for clarity is duplicated in the z direction. (**c**), Chemical structure of a DPPC lipid.

be negligible compared to the hydration repulsion for separations below 1.5 nm [80], so our simulations allow to realistically model the bilayer forces at low hydration. Snapshots of our simulations in fluid and gel states together with the DPPC chemical structure are presented in Fig. 2.2.

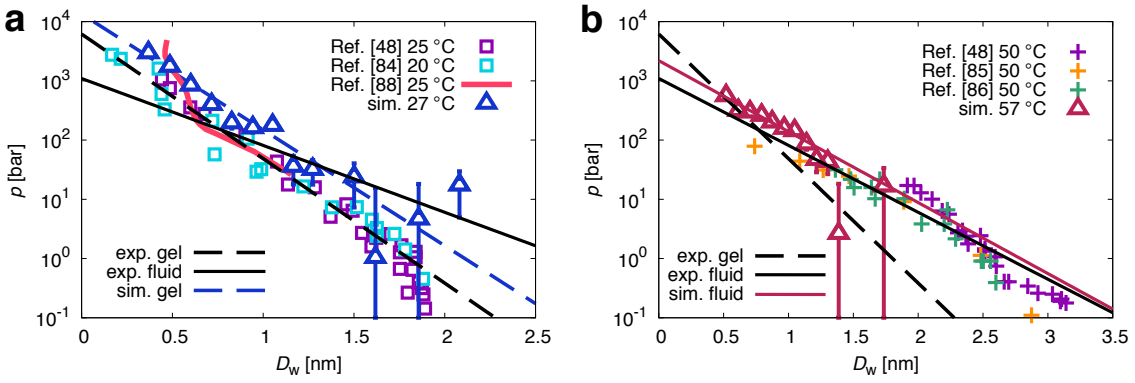

FIGURE 2.3: **Osmotic pressure data using a consistent definition of the water slab thickness.** Comparison of bilayer pressure from simulations (triangles) and experiments (squares and crosses) as a function of the water slab thickness D_w in the (**a**) gel and (**b**) fluid states. Exponential fits to the experimental data give decay lengths $\lambda_{gel} = 0.21 \pm 0.01$ nm (black broken line) for a fit range [0, 1.8 nm] and $\lambda_{fluid} = 0.38 \pm 0.02$ nm (black solid line) for a fit range [0, 2.6 nm]. Fits to the simulation data yield decay lengths $\lambda_{gel} = 0.22 \pm 0.02$ nm (blue broken line) and $\lambda_{fluid} = 0.36 \pm 0.02$ nm (red solid line) for fit ranges [0, 1.3 nm] and [0, 1.4 nm], respectively, restricted to the distance range where pressures are strictly positive.

In Fig. 2.3 we compare the interaction pressure from simulations in the osmotic pressure ensemble at fixed hydrostatic pressure of 1 bar (triangles) with experimental data (squares and crosses) in (a) gel and (b) fluid states as a function of the water slab thickness D_w. We calculate D_w based on the Gibbs-dividing surface position, which amounts to $D_w = N_w v_w^0 / A$, where N_w is the number of water molecules in one layer, v_w^0 is the

volume per water molecule in bulk, and A is the system area. Incidentally, this is the same conversion used in one experiment [48] and is based on the unambiguous thermodynamic definition of the membrane–water interface position. We use the same conversion for all experimental data sets. For both gel and fluid states, we observe excellent agreement among experimental and simulated pressure curves. The experimental decay length in the gel state is $\lambda_{\mathrm{gel}} = 0.21$ nm, in the fluid state we obtain $\lambda_{\mathrm{fluid}} = 0.38$ nm. Thus the experimental decay lengths for $p(D_{\mathrm{w}})$ differ among fluid and gel states and at the same time deviate significantly from the decay lengths of $p(D_{\mathrm{r}})$ in Fig. 2.1 (b). This clearly rules out a pure water-mediated mechanism for the hydration repulsion, because in this case not the decay length but only the hydration force amplitude should differ in the gel and fluid states. Fits to the simulation data yield $\lambda_{\mathrm{gel}} = 0.22$ nm and $\lambda_{\mathrm{fluid}} = 0.36$ nm, hence in good agreement with the experiments. This validates our further simulation analysis.

In order to gain insight into the origin of the hydration force and into its pronounced difference in the gel and fluid states, we decompose the total pressure p into the direct p_{dir} and indirect parts p_{ind} using our previously introduced decomposition scheme [57], where p_{dir} contains all membrane–membrane interactions, and $p_{\mathrm{ind}} = p - p_{\mathrm{dir}}$ contains the remaining water–water and water–membrane forces. For the calculation of the direct pressure contribution we explicitly add the z-components of the forces that act between all atoms in two bilayers across a water slab, while the indirect contribution contains all forces between one bilayer and an adjacent water slab (see Sec. 2.4.6 for details). This corresponds to a pressure decomposition on a dividing surface that is deformed such that it does not cut into lipid molecules. Note that this splitting is independent of the position and shape of the dividing surface and thus adds minimal ambiguity to the decomposition. Since the water chemical potential can not be uniquely separated into direct and indirect contributions, the pressure decomposition is done in the hydrostatic ensemble at fixed water chemical potential (see Sec. 2.4.5 for details). We have previously shown that the two ensembles at fixed pressure and at fixed water chemical potential give rise to quite similar pressure curves [58].

In Fig. 2.4 we plot the total pressure p together with the indirect pressure p_{ind} and (since it is attractive) the negative direct pressure $-p_{\mathrm{dir}}$ in the gel and fluid states. The attractive nature of the direct pressure has been explained by dipole–dipole interactions between lipid headgroups on two adjacent bilayers [94], whereas the indirect pressure has been demonstrated to arise from a combination of several force contributions that involve water adsorption on the bilayer surface as well as bilayer-induced water ordering [57].

We observe that $-p_{\mathrm{dir}}$ and p_{ind} are very similar to each other and thus nearly cancel, consequently, the total pressure $p = p_{\mathrm{ind}} + p_{\mathrm{dir}}$ is much reduced and smaller by roughly an order of magnitude. This holds for both gel and fluid data. The direct and indirect pressures exhibit for separations $D_{\mathrm{w}} > 1$ nm an exponential decay which is characterized by surprisingly similar decay lengths, roughly given by $\lambda_{\mathrm{gel}} = 0.19$ nm in the gel state and $\lambda_{\mathrm{fluid}} = 0.22$ nm in the fluid state (indicated by blue and red solid lines). The sum of these contributions, the total pressure p, however shows different exponential decay lengths of $\lambda_{\mathrm{gel}} = 0.22$ nm in the gel and $\lambda_{\mathrm{fluid}} = 0.36$ nm in the fluid states, as already shown and discussed in Fig. 2.3. The significant difference between the gel and fluid total pressures is thus caused by relatively tiny differences in the direct and indirect contributions, which

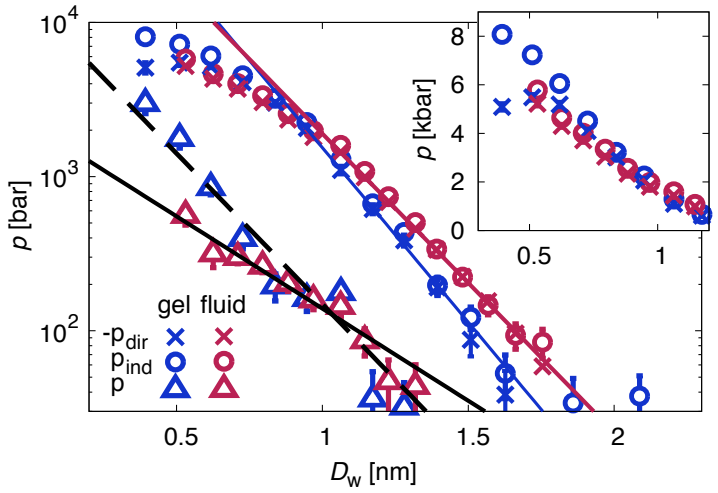

FIGURE 2.4: **Pressure decomposition.** Decomposition of the simulated pressure (triangles) into direct interactions between DPPC membranes $-p_{\mathrm{dir}}$ (crosses) and the indirect contribution $p_{\mathrm{ind}} = p - p_{\mathrm{dir}}$ (circles) in the gel (blue) and fluid states (red). Colored lines are simultaneous exponential fits to the direct and indirect contributions for $D_{\mathrm{w}} > 1$ nm with decay lengths $\lambda_{\mathrm{gel}} = 0.19$ nm in the gel (blue line) and $\lambda_{\mathrm{fluid}} = 0.22$ nm in the fluid state (red line). The exponential fits to the total pressures from Fig. 2.3 are included as black lines. In the inset $-p_{\mathrm{dir}}$ and p_{ind} are shown in linear scale.

are massively amplified since p_{dir} and p_{ind} almost exactly cancel. To look into this, we plot $-p_{\mathrm{dir}}$ and p_{ind} in a lin–lin representation in the inset of Fig. 2.4. There it is seen that $-p_{\mathrm{dir}}$ in the fluid and gel states are rather similar to each other, while the indirect (water-mediated) contributions p_{ind} differ substantially for small separations. We conclude that the difference between the total pressures p in fluid and gel states is mainly caused by a relatively small difference in the water-mediated indirect contribution p_{ind}. The different decay lengths of the total pressure p in fluid and the gel states comes as a surprise, since the decay lengths of the direct and indirect contributions do not differ much between the gel and fluid states. Given the similarity of the direct and indirect contributions, it becomes clear why an understanding of the hydration force could not be gained from theoretical consideration of the water-mediated or the direct membrane–membrane interactions alone, which has been the prevalent mode of thinking in the literature so far. It transpires that elucidating the origin of hydration forces requires simultaneous description of direct and indirect pressure contributions. Because of the near cancellation of the opposing pressure contributions theoretical descriptions must be very accurate in order not to make wrong predictions for the net hydration pressure.

2.3 Methods

We use the Gromacs simulation package [95] with the Berger lipid force field [96–98] and the SPC/E water model [99]. A comparison with simulations results that use different force fields for lipids and water is shown in the Sec. 2.4.7, which demonstrates that our results are robust with respect to force field variations. The assisted freezing method [100]

is used for the construction of fully hydrated membranes in the L_β (gel) phase (Fig. 2.2 (a)) at a temperature of $T = 270$ K, controlled by the v–rescale thermostat [101]. This fully hydrated membrane consists of 2×36 DPPC lipids hydrated by 40 water molecules per lipid. The structure is equilibrated at $T = 300$ K and afterwards gradually dehydrated by one molecule per lipid and each time equilibrated for 5 ns down to a hydration level of 3 waters per lipid molecule. All equilibrations are performed in the NpT ensemble (See Sec. 2.4.1 for details). To improve sampling, we use four different starting configurations, which are independently dehydrated five times with different random seeds, giving 20 different systems per hydration level. For production runs in the L_α fluid phase (Fig. 2.2 (b)) the temperature in the gel state is increased to 330 K, above the melting temperature of DPPC membranes in experiments and in simulations [23, 102–104].

All simulations are performed with periodic boundary conditions and a time step of 2 fs. An anisotropic pressure coupling is employed using the Berendsen barostat [105] with a time constant of $\tau_P = 2$ ps. The dispersion part of the van-der-Waals interactions is modeled via Lennard-Jones potentials with a cut-off at 0.9 nm. This treatment does not capture the long-range van-der-Waals attraction, but this effect is negligible in the separation range relevant for the present work [58]. Electrostatics are simulated by the Particle–Mesh–Ewald (PME) method [90, 106] with a 0.9 nm real-space cutoff. Prior to the production run, fluid and gel membranes at all hydration levels are equilibrated for at least 5ns. In the osmotic ensemble, the pressure is set to $p = 1$ bar and the chemical potential μ is measured using the Test Particle Insertion method [107] for the van-der-Waals contribution and thermodynamic integration with 18 values along the TI reaction coordinate for the electrostatic contribution, which is processed by the Multistate Bennett Acceptance Ratio (MBAR) method [108]. Each system is simulated for 5 ns, so that the total simulation time is 100 ns per hydration level and one value of the TI reaction coordinate. As we run simulations for 17 hydration levels in the gel phase and 16 in the fluid phase, our total simulation time exceeds 60 μs. From the 20 different systems per hydration level the statistical error of the chemical potential and thus of the osmotic pressure is estimated.

In the MD simulations, the water slab thickness D_w is defined by $D_w = N v_w / A$, where N is the number of water molecules in the system, v_w is the volume of one water molecule in bulk and A is the simulation box area. We measured $\rho_{bulk}(T = 300\ \mathrm{K}) = 985\ \mathrm{kg/m^3}$ and $\rho_{bulk}(T = 330\ \mathrm{K}) = 967\ \mathrm{kg/m^3}$ in water bulk simulations, which correspond to $v_w = 0.0304\ \mathrm{nm^3}$ for $T = 300$ K and $v_w = 0.0309\ \mathrm{nm^3}$ for $T = 330$ K. With this definition, the water slab thickness equals the distance between the Gibbs dividing surfaces that are located on both sides of the water slab.

Using the equation $\Delta\mu = -v_w^0 p$ (see Sec. 2.4.5 for the derivation), the results for μ are converted into equivalent osmotic pressures. The hydrostatic simulations, used to decompose the pressure into direct and indirect parts, employ the predicted osmotic pressure. We explicitly verified that the resulting chemical potential equals the bulk water chemical potential.

2.4 Supplementary Material

2.4.1 Equilibration and Sampling

Sampling of the phase space is a major issue in all MD simulations of hydrated membranes, especially when it comes to low hydration levels. In Fig. 2.5 we demonstrate that our system is equilibrated, since there is no drift in any of the structural quantities, represented by the mean tilt angle $\langle\theta\rangle$ of the P-N-vector in the headgroup, the simulation box area A and the lamellar repeat distance D_r. Also the system enthalpy H is constant, which means that there are no major rearrangements of the bilayer structure occurring. On the other hand, we see fluctuations around the mean in these structural quantities on time scales of more than 100 ns. This is quantified in Fig. 2.6, where the autocorrelation functions

$$C(t) = \frac{1}{C_0\,(T-t)} \int_0^{T-t} \mathrm{d}t' X(t'+t)X(t') \qquad \text{with} \qquad C_0 = \frac{1}{T}\int_0^T \mathrm{d}t' X^2(t') \tag{2.1}$$

are shown. Here, T denotes the simulation length and X the quantity of interest. All autocorrelations decay on time scales of approximately $100 - 200$ ns, hence a trajectory that sufficiently samples all configurations would require to be of a length of several hundred nanoseconds. For this reason we base our analysis on 20 independently constructed structures that are each simulated for 5 ns to assure that we are sampling the entire configuration space in a reasonable computation time.

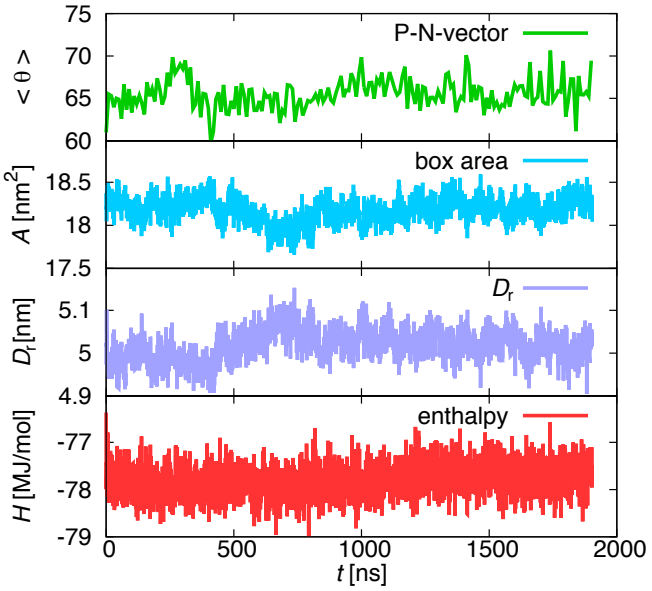

FIGURE 2.5: From top to bottom: The average tilt angle $\langle\theta\rangle$ of the P-N–vector, the simulation box area A, the lamellar repeat distance D_r and the system enthalpy H as a function of time for a 1.9 ¯s long simulation of a lipid bilayer in the gel phase with 4 water molecules per lipid.

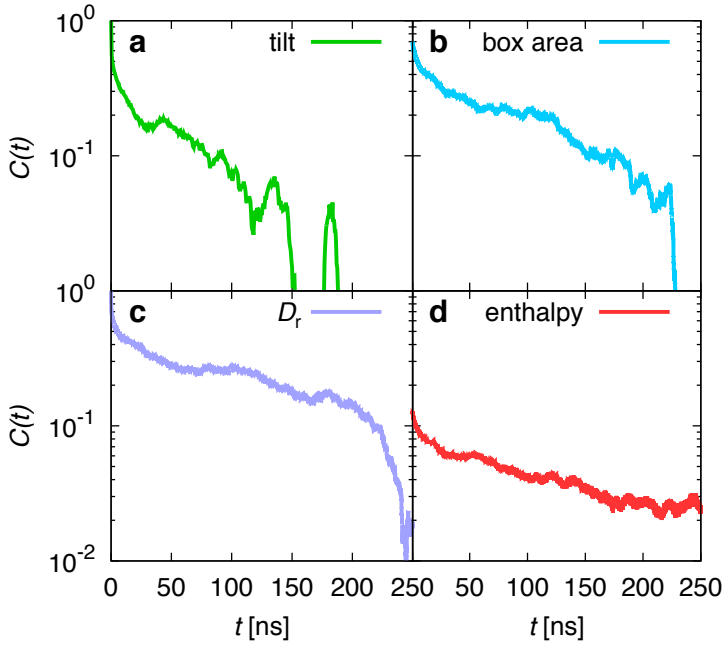

FIGURE 2.6: Normalized autocorrelation functions defined in Eq. 2.1 of the average tilt angle $\langle\theta\rangle$ of the P-N–vector (**a**), the simulation box area A (**b**), the lamellar repeat distance D_r (**c**) and the system enthalpy H (**d**) as a function of time for a 1.9 ¯s long simulation of a lipid bilayer in the gel phase with 4 water molecules per lipid.

2.4.2 Exponential Fits to Published Experimental Pressure Data

In Table 2.1 the parameters for fits of $p = p_0 \exp(-D_w/\lambda)$ to the published experimental pressure data in Fig. 1 are presented.

group	λ [nm]	$\Delta\lambda$ [nm]	$\ln p_0$ [ln bar]	$\Delta \ln p_0$ [ln bar]
Lis 25 °C	0.176	0.011	9.47	0.57
McIntosh 20 °C	0.108	0.004	10.18	0.27
Lis 50 °C	0.258	0.010	10.06	0.39
Gawrisch 50 °C	0.224	0.013	10.61	0.50
Petrache 50 °C	0.175	0.012	7.12	0.43

TABLE 2.1: Parameters for fits of $p = p_0 \exp(-D_w/\lambda)$ to the published experimental data in Fig. 1 (a) (main text).

2.4.3 Conversion of D_r to D_w

2.4.3.1 Method by Lis et al.

Lis et al. [48] use lipid–water mixtures of known lipid weight fraction Φ_L and measure the lamellar repeat distance D_r by X-ray diffraction. The water slab thickness is then given by

$$D_w^{Lis} = \frac{D_r}{1 + \frac{\Phi_L v_L}{(1-\Phi_L) v_w}}, \tag{2.2}$$

where v_w and v_L denote the partial specific volumes of water and lipids, respectively. For water, a value of $v_w = 1\ \mathrm{cm}^3/\mathrm{g}$ is used independent of D_w, whereas for the lipids in the gel and the fluid phase the values from the work of Tardieu et al. are taken [109]. There it is assumed that a hydrocarbon chain in the gel state takes 0.95 the volume of a chain in the fluid state. Since the inverse density of a membrane in the fluid state is $v_L^{fluid} = 1\ \mathrm{cm}^3/\mathrm{g}$, we hence arrive at a value of $v_L^{gel} = 0.95\ \mathrm{cm}^3/\mathrm{g}$ for the gel phase. Furthermore, it is assumed that the membrane is incompressible in both phases, thus these values do not change with hydration. From our simulations we obtain values of $v_L^{gel} = 0.94 - 0.95\ \mathrm{cm}^3/\mathrm{g}$ and $v_L^{fluid} = 1.03 - 1.04\ \mathrm{cm}^3/\mathrm{g}$, which are not too different from these assumptions (see Fig. 2.7).

Lis et al. [48] report the molecular force between two lipids instead of the pressure. From the area per lipid as a function of the lipid weight concentration, which is also measured in their work, we transform the reported force into a pressure.

As already mentioned in the main text, we choose the method introduced by Lis et al. to transform all experimental data from D_r to D_w, since it allows for an unambiguous determination of the water content between the membranes. In all other works the exact water content between the membranes is not determined.

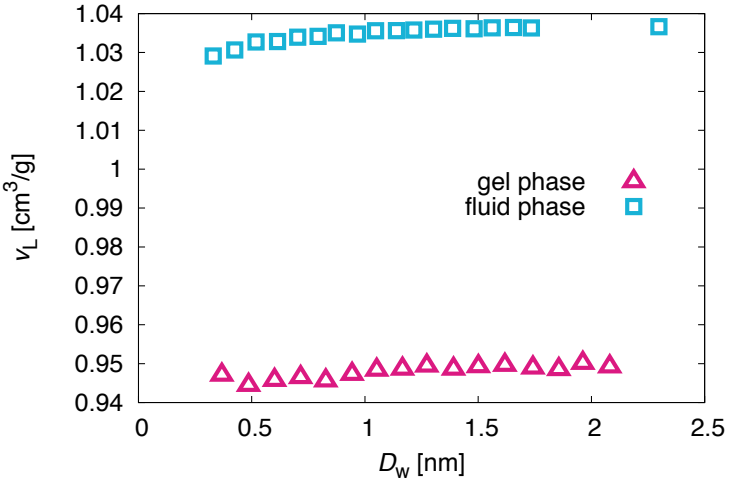

FIGURE 2.7: Partial specific volume v_L of DPPC as obtained from the simulations in the gel state (triangles) and the fluid state (squares) under the assumption that v_w is independent of D_w.

2.4.3.2 Method by McIntosh and Simon

McIntosh et al. [84] determine the water slab thickness from X-ray diffraction experiments. In their work, they fit continuous structure amplitude functions to the measured data. These functions are then Fourier transformed to obtain electron density profiles for egg phosphatidylcholine bilayers that are used to calculate the bilayer thickness D_l as well as the bilayer repeat distance D_r. Specifically, using space-filling models, it is assumed that the distance between the electron density peaks 1 nm equals the membrane thickness D_l. The water slab thickness then follows as $D_w^{McInt.} = D_r - D_l$. Our simulations (Fig. 2.8) are consistent with a constant membrane peak distance for the lipid density profiles in the gel phase, in agreement with experiments [110]. Only pressures larger than 1000 bar lead to a slight increase of the peak distance in z-direction, which is also in agreement with experimental findings [84].

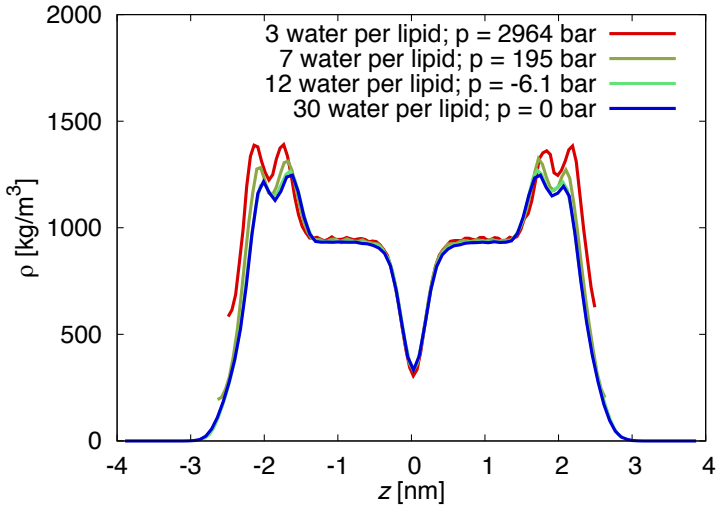

FIGURE 2.8: Density profiles of DPPC lipids obtained from simulations at four hydration levels in the gel phase.

2.4.3.3 Methods by Petrache et al. and Gawrisch et al.

Petrache et al. [86] as well as Gawrisch et al. [85] use the bilayer area compressibility K to calculate the bilayer thicknesses [50]. They derive the relation

$$D_l / D_l^\star = \frac{K + (p - p^\star) D_r}{K + (p - p^\star) D_l^\star} \tag{2.3}$$

with which they obtain the bilayer thickness D_l without measuring the lipid weight fraction Φ_L of the lipids. In order to apply this formula, they use the bilayer thickness $D_l^\star$ for one reference pressure $p^\star$. The reference values $D_l^\star$ and $p^\star$ are obtained either by a measurement at one reference weight fraction (Gawrisch et al. [85]) or by X-ray diffraction (Petrache et al. [86]).

2.4.3.4 Back Conversion

As shown above, each experimental group uses a different method to convert D_r to D_w, which relies on structural quantities or additional assumptions. However, a transformation from $p(D_r)$ data to $p(D_w)$ data using one conversion method for all data sets is not straightforward, since the needed experimental specifications are not published in all papers. Hence, for example, the conversion method of Lis et al. [48] cannot be applied directly to the published $p(D_r)$ data by McIntosh and Simon [84], since the weight fractions are not published. We thus use a quadratic function of the form $D_r(D_w) = aD_w^2 + bD_w + c$ to fit the relation between D_r and D_w for each experimental data set, which allows to interconvert all experimental data between different definitions of D_w. The resulting graphs are presented in Fig. 2.9 and the fitting parameters are listed in Table 2.2.

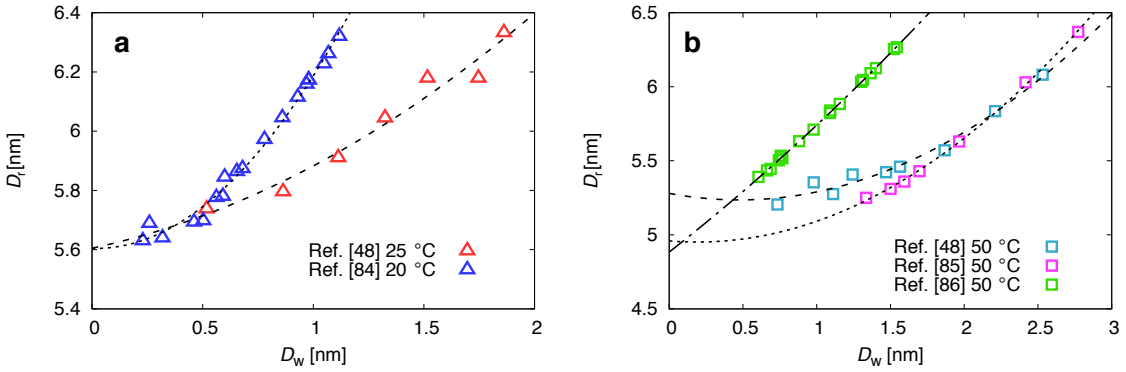

FIGURE 2.9: Lamellar repeat distance D_r as a function of the water slab thickness D_w for the gel phase (**a**) and the fluid phase (**b**) obtained from different experiments. To all data sets we fit a function of the form $D_r(D_w) = aD_w^2 + bD_w + c$. Note that for the data representation in Fig. 3 in the main text, only the fits to the data of Lis et al. are needed.

group	a [1/nm]	b	c [nm]
Lis 25 °C	0.119	0.159	5.60
McIntosh 20 °C	0.603	−0.020	5.60
Lis 50 °C	0.197	−0.187	5.28
Gawrisch 50 °C	0.214	−0.081	4.96
Petrache 50 °C	0.078	0.780	4.88

TABLE 2.2: Parameters of fits according to $D_r(D_w) = aD_w^2 + bD_w + c$ of experimental data in Fig. 2.9.

2.4.4 Data Conversion Using the Method of Lis et al.

Table 2.3 shows the results of the fits of the function $p = p_0 \exp(-D_w/\lambda)$ to the pressure distance curves after application of the conversion method used by Lis et al [48].

	Experiments gel	Simulation 300 K	Experiments fluid	Simulation 330 K
ln p_0 [ln bar]	8.72	9.51	7.00	7.69
$\Delta \ln p_0$ [ln bar]	0.20	0.31	0.37	0.18
λ [nm]	0.207	0.222	0.384	0.363
$\Delta\lambda$ [nm]	0.007	0.021	0.026	0.028

TABLE 2.3: Parameters of fits according to $p = p_0 \exp(-D_w/\lambda)$ of the experimental and simulation data in Fig. 3 in the main text.

2.4.5 Thermodynamic Extrapolation

The Gibbs–Duhem equation for bulk water, $N_w d\mu = -S dT + V dp$, evaluated at constant temperature yields

$$\left(\frac{\partial \mu}{\partial p}\right)_T = \frac{V}{N_w} = v_w(p)$$
$$\Rightarrow \quad \Delta\mu = \mu_\infty - \mu = \int_p^{p_\infty} v_w(p')\, dp' , \tag{2.4}$$

with the molar volume of water v_w and the interaction pressure p that acts between the membranes. For pressures up to kilobars the water compressibility can be practically neglected [57], hence Eq. 2.4 simplifies to

$$\Delta\mu = v_w (p_\infty - p) = -v_w^0 p , \tag{2.5}$$

where the pressure p_∞ in the bulk reference system can be neglected and is set to zero. Thus in bulk water a reduced chemical potential is equivalent to a reduced pressure. We use the same equation to convert measured chemical potentials in the osmotic ensemble at $p = 1$ bar to equivalent osmotic pressures, exactly as is done in experiments that use osmotic pressure techniques.

2.4.6 Technical Details on the Interaction Decomposition

The decomposition of the hydration repulsion is done by rerunning simulation trajectories where the simulation box is expanded in the z-direction such that on each side of the water slab, which is in the center of the box, there is only one monolayer of the membrane. This way interactions with periodic images are eliminated. In order to measure the direct contribution p_{dir}, also the water slab is removed, thus only the opposing membrane monolayers that interact with each other across free space are left, see Fig. 2.10 (b). The force acting on one of the monolayers divided by the area gives the direct contribution to the hydration pressure. In order to obtain the indirect contribution p_{ind}, one monolayer is

removed instead of the water, and again the force acting on the remaining monolayer is measured (Fig. 2.10 (c)). As a consistency check of our decomposition scheme, we compare the total pressure p from the simulations with the sum of the pressure contributions $p_{\text{dir}} + p_{\text{ind}}$ and find perfect agreement.

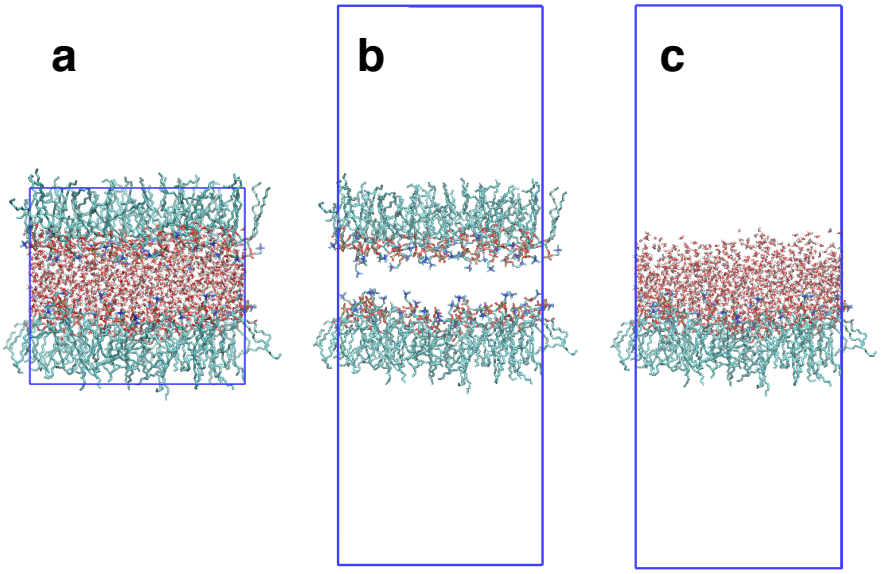

FIGURE 2.10: Decomposition of the original system (**a**) into a system without water (**b**), in which the direct contribution p_{dir} is measured, and a system with only one monolayer (**c**), in which the indirect contribution p_{ind} to the hydration pressure is measured. The blue boxes indicate the size of the simulation box.

Because a decomposition of the chemical potential into direct and indirect contributions is not possible, the composition into direct and indirect pressure contributions is done in the hydrostatic ensemble, where the pressure of the system is chosen such that the water chemical potential is constant.

2.4.7 Force field Dependence of the Simulation Results

In order to investigate the dependence of our results on the employed force field, we also performed simulations with the CHARMM36UA [111] lipid force field and using the TIP3P water model [112], which carries additional Lennard-Jones sites on the H-atoms. In order to determine the chemical potential of this water model, also for the van-der-Waals interactions the TI method is used. For the CHARMM36UA force field, the input parameters from the NMRLipid project [113, 114] are converted with the PyTopol script in order to make this force field compatible with Gromacs. In Fig. 2.11 (a) we compare the data from Fig. 3 (b) in the main text, including experimental data for fluid membranes and our simulation results obtained with the Berger force field, with simulation results using the CHARMM36UA force field. Both simulation results are in very good agreement with each other and also with the experimental data.

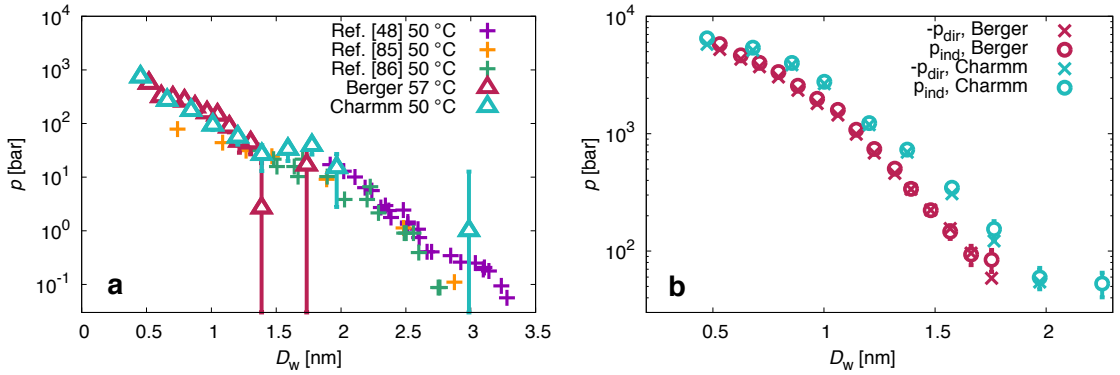

FIGURE 2.11: Comparison of the Berger force field and the CHARMM36UA force field: (**a**), Hydration pressures obtained from both force fields in the fluid phase compared to the experimental results taken from Fig. 3 (b) in the main text. (**b**), Decomposition of the pressures from both force fields into direct and indirect contributions $-p_{\mathrm{dir}}$ and p_{ind}.

In Fig. 2.11 (b) we compare simulation data for the direct and indirect pressures using the CHARMM36UA force field with the pressures from Fig. 4. Here we observe that both pressure contributions $-p_{\mathrm{dir}}$ and p_{ind} have a slightly larger decay length in the CHARMM36UA force field compared to the Berger force field. But qualitatively the picture does not change: Both pressure contributions nearly cancel each other and have a much larger amplitude than the total pressure p in Fig. 2.11 (a). We hence conclude that our results are robust with respect to changes in the force field.

A measurement in the osmotic ensemble with a constant pressure of 1 bar requires a calculation of the chemical potential in both systems presented in Fig. 2.10 and a subsequent thermodynamic extrapolation. The systems in Fig. 2.10 (b) and (c) are not stable and therefore the interaction pressures are calculated in reruns, whereas a thermodynamic integration cannot be applied to a rerun since it would not capture the changes in the dynamics of the integrated particle.

2.4.8 Validation of the Thermodynamic Extrapolation

In order to prove that the linear thermodynamic extrapolation holds in our simulations, we perform four simulations of membranes in the gel phase at pressures p obtained by the extrapolation procedure, Eq. 2.5, using the chemical potential which is determined from simulations at 1 bar. The measured chemical potential μ of the water molecules is shown in Fig. 2.12. We observe that indeed μ is constant within the errors and equal to the chemical potential in excess water μ_{e}, which is defined as the chemical potential in the center of the water slab at the highest hydration level.

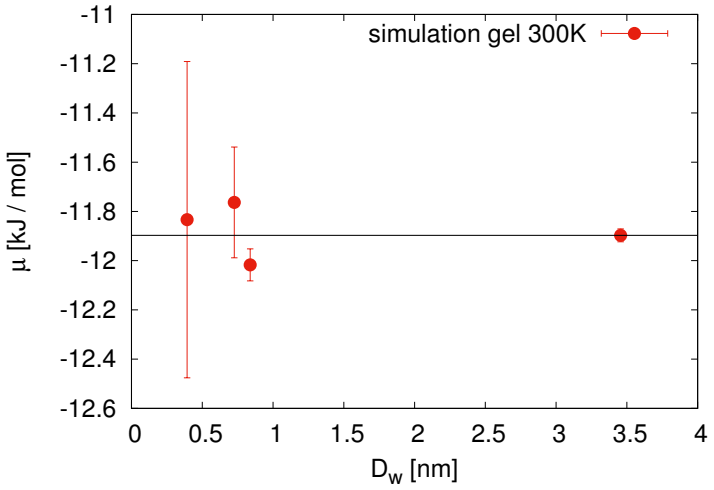

FIGURE 2.12: Chemical potential for gel systems performed at extrapolated pressure p computed via Eq. 2.5. The black solid line indicates the chemical potential μ_e at excess water.

2.4.9 Entropy vs. Enthalpy

Further insight into the mechanism of the hydration repulsion can be obtained from a decomposition into its entropic and enthalpic contributions. These can be calculated as follows: At excess hydration $N = N_e$ the chemical potential of water confined between two membranes equals the bulk chemical potential, $\mu(N = N_e) = \mu_e$. Using the definition of the chemical potential as the derivative of the Gibbs free energy with respect to the particle number at constant temperature T and pressure p_0, we can therefore express the excess Gibbs free energy for a bilayer system with N_w water molecules as

$$\begin{aligned}\Delta G(p = p_0, N_w) &= \int_{N_e}^{N_w} \mu(N_w')\mathrm{d}N_w' - \int_{N_e}^{N_w} \mu_\infty \mathrm{d}N_w' \\ &= -\int_{N_w}^{N_e} \left(\mu(N_w') - \mu_e\right) \mathrm{d}N_w' \,. \end{aligned} \tag{2.6}$$

In this equation, $\Delta G(p = p_0, N_w)$ is the Gibbs free energy which is needed to transfer water molecules from a fully hydrated membrane to a bulk reservoir such that there are N_w water molecules left between the membranes.

Assuming that water is incompressible we can transform the Gibbs free energy at constant pressure to a Gibbs free energy at constant chemical potential $\mu = \mu_0$:

$$\begin{aligned}\Delta G(\mu = \mu_e, N_w) &= -\int_{N(D_w)}^{N_e} \left(\mu(N_w') - \mu_\infty\right) \mathrm{d}N_w' = \int_{D_w}^{D_{w,e}} v_w \Delta p(D_w') \frac{\mathrm{d}N_w}{\mathrm{d}D_w'} \mathrm{d}D_w' \\ &= \int_{D_w}^{D_{w,e}} \Delta p(D_w') A(D_w') \mathrm{d}D_w' \\ &= \int_{D_w}^{D_{w,e}} F(D_w') \mathrm{d}D_w' \,, \end{aligned} \tag{2.7}$$

where $D_{w,e}$ is the separation of the membranes at excess hydration and F is the force acting on the membrane surface. In simulations in the osmotic ensemble, i.e. at a constant pressure of $p = 1$ bar, the free energy can be computed by Eq. 2.6, whereas in the hydrostatic ensemble, i.e. at extrapolated pressure according to Eq. 2.5 and constant chemical potential $\mu = \mu_e$, Eq. 2.7 should be used. The equivalency of both methods is checked numerically in Fig. 2.13, where indeed only deviations within the error bars are visible between the two expressions.

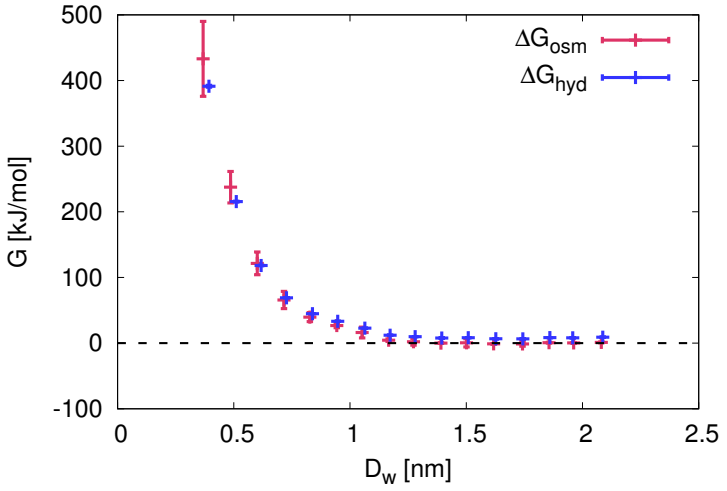

FIGURE 2.13: Comparison between the Gibbs free energy $\Delta G_{\text{osm.}}$ from an osmotic simulation ($p = 1$ bar) using Eq. 2.6 (red) and the Gibbs free energy $\Delta G_{\text{hyd.}}$ from a hydrostatic simulation (p according to Eq. 2.5 and $\mu = \mu_e$) using Eq. 2.7 (blue).

In order to compute the entropy S, we use the thermodynamic relation $G = U + pV - TS$ between the Gibbs free energy G and the energy U. For ΔG we arrive at

$$\Delta G = \Delta U + V\Delta p + p\Delta V - T\Delta S\,. \tag{2.8}$$

Since water as well as the membrane are incompressible at the pressure scales we are interested in [48], we can neglect the term $p\Delta V$. In the simulations at constant pressure $p = p_0$ (osmotic ensemble), also the term $V\Delta p$ vanishes, hence we only need to evaluate the remaining contribution ΔU. This quantity corresponds to the energetic contribution to the free energy which is stored in the system hydrated with N_w water molecules due to the hydration repulsion. We evaluate ΔU by the following procedure: In our simulations, we can extract the total energy $U(N_w)$ of our system hydrated with N_w water molecules. A hydration of this system with additional water molecules from a bulk reservoir to a fully hydrated state with N_e water molecules increases its energy by $U(N_e) - U(N_w)$. On the other hand, the bulk reservoir reduces its energy by $U_b = \varepsilon_{\text{bulk}}(N_e - N_w)$, where $\varepsilon_{\text{bulk}} = (\partial U/\partial N_w)^{\text{bulk}}_{p,T}$ corresponds to the energy of one water molecule in the bulk at pressure p_0. The total energy change (membrane system plus reservoir) upon hydration

thus equals

$$-\Delta U = U(N_\infty) - U(N_\mathrm{w}) - U_\mathrm{b}\,, \tag{2.9}$$

where the minus sign comes from the fact that in this description the energy is being released from the membrane system. As all quantities on the right hand side of Eq. 2.9 can be extracted from simulations, we can use Eq. 2.8 to determine the entropy of the system.

In Fig. 2.14 the Gibbs free energy in the osmotic ensemble is presented with its decomposition into the entropic contribution $-T\Delta S$ and the contribution ΔU from the internal energy for the gel and the fluid membrane. Qualitatively we observe a similar behavior for both systems: The Gibbs free energy is approximately zero for separations $D_\mathrm{w} \gtrsim 1.0$ nm and increases for $D_\mathrm{w} \approx 0.4$ nm to about 400 kJ/mol in the gel phase and 300 kJ/mol in the fluid phase. The internal energy ΔU is slightly negative in the fluid phase for separations $D_\mathrm{w} > 0.8$ nm, with a minimum at $D_\mathrm{w} \approx 1.0$ nm. In the gel phase, a similar behavior of the internal energy is observed for $D_\mathrm{w} > 0.8$ nm. For both phases, the internal energy turns positive for $D_\mathrm{w} < 0.8$ nm and and increases strongly for smaller separations. In contrast, the contribution $-T\Delta S$ shows exactly the opposite behavior, as it is positive for $D_\mathrm{w} > 0.8$ nm with a maximum at $D_\mathrm{w} \approx 1.0$ nm and becomes increasingly negative at small separations. The fact that the entropy ΔS is positive for small separations, where we expect the configuration space of the headgroups as well as the water molecules to be highly restricted, might be surprising at first sight. However, one has to keep in mind that the entropy difference ΔS corresponds to the increase of entropy when water, which is confined between the membranes, is transferred into the bulk reservoir. Indeed, at small separations, the water molecules which move from the membrane system to the reservoir experience a large increase of their conformational space, resulting in a higher entropy of the total system (membrane system plus reservoir).

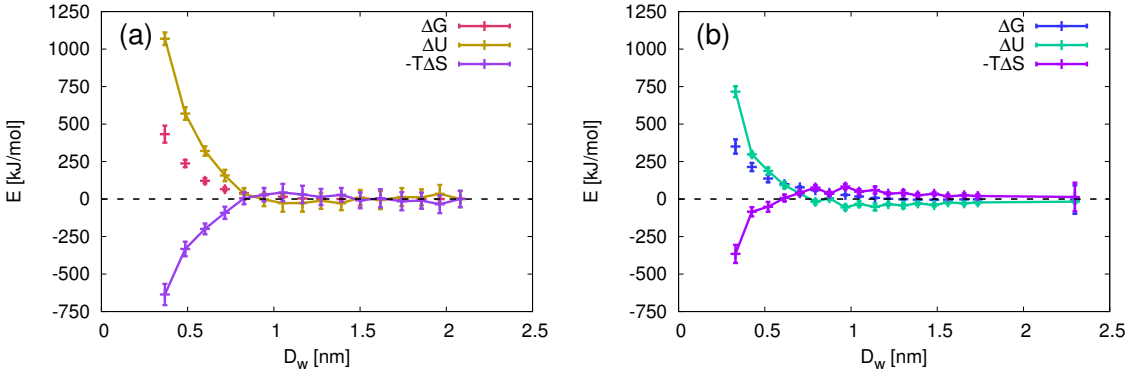

FIGURE 2.14: Decomposition of the Gibbs free energy G into the internal energy ΔU and entropy $-T\Delta S$ for the system in gel phase (a) and fluid phase (b).

Our findings lead to the following interpretation of the energetic behavior of the system (See Fig. 2.15 for a summary): Starting at small separations, both the entropy as well as the internal energy of the total system decrease upon hydration (increasing D_w), hence the transfer of water from the reservoir to the membrane system is energy-driven. This

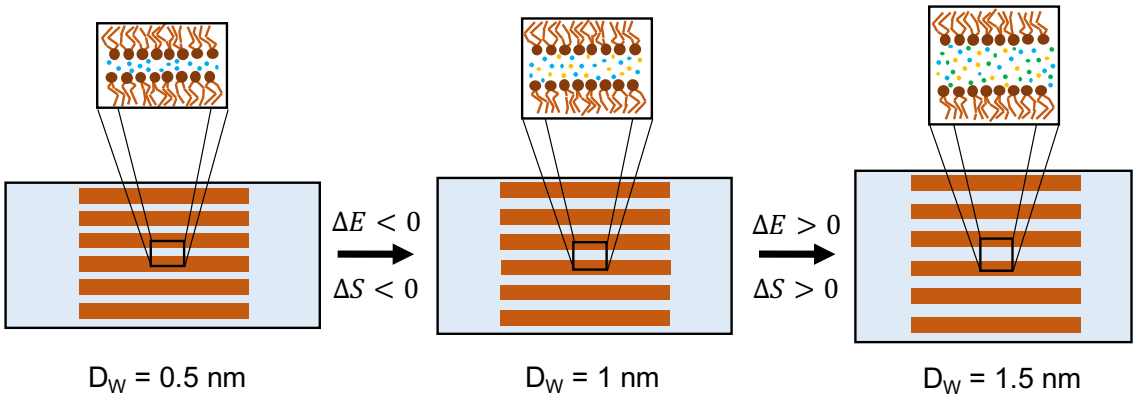

FIGURE 2.15: Hydration of lipid membranes: The thermodynamic quantities G, U and S all refer to a system containing lipid membranes and a bulk reservoir, whereas in our simulation we only simulate the systems which are zoomed in. In the first step, water molecules (yellow) from the bulk insert the water slab of a dehydrated membrane. By doing this, they reduce their configurational space (and thus their entropy), but also reduce the energy of the system, as the hydration of the headgroups is energetically favorable [88]. Thus, the hydration is energy-driven. In the second step, a further hydration with water molecules (green) from the reservoir increases the energy and entropy of the entire system. In this case, the hydration is entropy-driven. Note that the volume of the entire system (bilayers plus bulk water) remains constant.

changes at a separation of $D_w \approx 1.0$ nm, where the energy is minimal. Further hydration of the membranes increases the energy and the entropy, hence from that point on the hydration is entropy-driven. This picture is qualitatively in good agreement with calorimetric experiments of phospholipid hydration [88], however with the transition from energy-driven to entropy-driven hydration occurring at slightly smaller hydration levels.

Chapter 3

Memory Effects in the Dynamics of Confined Small Molecules

Bibliographic information: The content of this chapter is in preparation to be submitted to a peer-reviewed journal (Ref. ii).

3.1 Introduction

Molecular friction plays an essential role in a multitude of processes in biology, chemistry and physics like the lubrication of solids [115] or the permeation through nanopores [116]. The simplest model for the friction coefficient γ in a solvent with viscosity η is Stokes' law $\gamma = 6\pi\eta R$, which applies to a spherical particle of radius R with no-slip boundary conditions. Stokes' law describes particle friction down to the nanometer scale [117] and extensions have been proposed for particles of molecular size [118, 119]. Recently, a modification of Stokes' law due to a confinement potential acting on the particle was demonstrated [120]. On the basis of molecular dynamics (MD) simulations of a solvated methane molecule it was shown that the friction coefficient increases with the strength of the confining potential.

In the present work, we analyze how this increase of the friction is influenced by the solute properties. We perform MD simulations of five molecules (methane, water, Na^+, Na^- and glycerol), which are solvated in water and confined by a harmonic potential. The choice of the solutes is motivated by the aim to cover variations in hydrophilicity, charge, and size of the particles. In particular, by comparing the Na^+-ion with the negatively charged version Na^-, we investigate how the sign of the charge of a particle determines this anomalous friction effect. The confinement-induced increment of the friction coefficient is observed for all particles and the amplitude of this effect varies with the size, the charge, and hydrophilicity of the solute molecule. While for methane and water a change of the spring constant from $K = 0$ to $K = 25000\,\mathrm{kJ/(mol\,nm^2)}$ results in an increase of the friction coefficient by about 50 %, glycerol in water experiences a change of only 5 %. Connected with the increased friction is a slowdown of the orientational correlation time of water

molecules within the first hydration shell around the investigated particles. This is in agreement with measurements of water orientational relaxation in the hydration shells of proteins, which were undertaken in computer simulations [121] as well as NMR experiments [122].

Using water–glycerol mixtures as a solvent, we observe that the dependence of the friction on the confinement magnifies with increasing viscosity. In a water–glycerol mixture with 50 % mass fraction of glycerol the viscosity is about 7 times higher than in pure water and the friction of glycerol increases from 5 % for pure water to 25 %. The enhanced friction can be explained on the basis of the underlying time scales of the solvent relaxation as well as of the particle dynamics [120]. Generally, confinement-dependent friction is expected in the case when the longest relaxation time of the solvent is larger than the time scale at which the particle motion turns from inertial to diffusive. This indicates that confinement-dependent friction is not only limited to small molecules, but also complex macromolecules like proteins or DNA can experience this effect if solvated in a viscous medium.

The friction coefficient of the solute is determined from memory kernels in the framework of the generalized Langevin equation (GLE) [42]. The extraction of memory kernels from particle trajectories was pioneered by Berne [63], who developed an iterative method based on a reformulation of the GLE into a Volterra equation. Further methods include the solution of the GLE in Fourier space [123] or the fit of parametrized memory kernels to the observed correlation functions [120]. In the present work, we develop an integrated version of Berne's method and prove that this yields the best results for the memory kernels for our data.

3.2 Theory

In order to describe systems where the microscopic time scale of the fluid molecules is approximately of the same order of magnitude as the particle dynamics, Mori introduced the generalized Langevin equation (GLE), which contains a time-dependent memory kernel [42]. In his formalism, the friction force does not instantaneously act on the particle, but retardation effects are taken into account. The generalized Langevin equation is expressed by

$$m\ddot{x}(t) = -\int_0^t \mathrm{d}t'\, \Gamma(t')\dot{x}(t-t') - Kx(t) + F_\mathrm{R}(t)\,, \tag{3.1}$$

where the time evolution of the process starts at $t = 0$. Here, we included an external harmonic potential with spring constant K. The random force $F_\mathrm{R}(t)$ and the memory kernel $\Gamma(t)$ in this equation are connected by the fluctuation-dissipation theorem

$$\langle F_\mathrm{R}(t) F_\mathrm{R}(t')\rangle = k_\mathrm{B}T\Gamma(t-t')\,. \tag{3.2}$$

A different version of Eq. 3.1,

$$m\ddot{x}(t) = -\int_0^\infty \mathrm{d}t'\, \Gamma(t')\dot{x}(t-t') - Kx(t) + F_\mathrm{R}(t)\,, \tag{3.3}$$

with the upper integration limit $t = \infty$, has also been introduced in literature [41, 124]. This second version corresponds to a shift in the random force by $\Delta F_{\mathrm{R}}(t) = \int_t^\infty \mathrm{d}t'\, \Gamma(t')\dot{x}(t-t')$.

Equations 3.1 and 3.3 are difficult to handle in MD simulations, since it is not obvious how to split the total force acting on a particle, which can be extracted from the particle trajectory, into the random force $F_{\mathrm{R}}(t)$ and the friction force, which is given by the integral in both equations. A solution to this problem was first provided by Berne et al. [63, 125], who multiplied Eq. 3.1 with the initial velocity $\dot{x}(0) = v(0)$ of the particle and averaged the resulting equation over the random force. Using the fact that the initial velocity and the random force at any time are uncorrelated, $\langle v(0)F_{\mathrm{R}}(t)\rangle = 0$, this leads to a Volterra equation of first kind,

$$m\dot{C}^{vv}(t) = -\int_0^t \mathrm{d}t'\, \Gamma^\star(t')C^{vv}(t-t')\,, \tag{3.4}$$

which relates correlation functions of the particle motion to the memory kernel. In this equation, we introduced the effective memory kernel $\Gamma^\star(t) = \Gamma(t) + K$ and the velocity autocorrelation function $C^{vv}(t) = \langle v(0)v(t)\rangle$. The Volterra equation of first kind, which is a linear integro-differential equation, can generally be solved analytically via Laplace-transform for the memory kernel $\Gamma^\star(t)$. In Sec. 3.8.1 we show that Eq. 3.4 can equivalently be derived from Eq. 3.3 via the Kramers–Kronig relations. Algorithms based on Eq. 3.4 have frequently been used to extract memory kernels of unconfined particles ($K = 0$) from simulations [124, 126], however it has been argued that they lack stability [127]. Therefore, it is advantageous to reformulate Eq. 3.4 in order to develop more stable algorithms. In this work, we integrate Eq. 3.4 (see Sec. 3.8.3 for details), which yields

$$mC^{vv}(t) = -\int_0^t \mathrm{d}t'\, G(t')C^{vv}(t-t') + KC^{xx}(t)\,, \tag{3.5}$$

where $C^{xx}(t) = \langle x(0)x(t)\rangle$ and $G(t)$ is the running integral over the memory kernel defined as

$$G(t) = \int_0^t \mathrm{d}t'\, \Gamma(t')\,. \tag{3.6}$$

In the limit of $t \to \infty$, the integral $G(t)$ gives the friction coefficient γ, i.e. $G(t \to \infty) = \gamma$. Equation 3.5 again is a Volterra equation of first kind, which in this case relates $G(t)$ to the velocity and position autocorrelation functions of the particle. A discretized version of Eq. 3.5 is in the following used to extract memory kernels from trajectories.

3.3 Methods

3.3.1 Simulation Setup

All simulations consist of one solute molecule and the solvent molecules, which are set into a cubic box of 4.5 nm size in each dimension and period boundary conditions. As solute molecules methane, water, Na^+, Na^-, and glycerol are chosen. In the simulations with glycerol as solute, also water–glycerol mixtures as solvent are used in order to change the viscosity of the solvent. In these simulations, the mass fractions between glycerol and water are 0.333, 0.434 and 0.500.

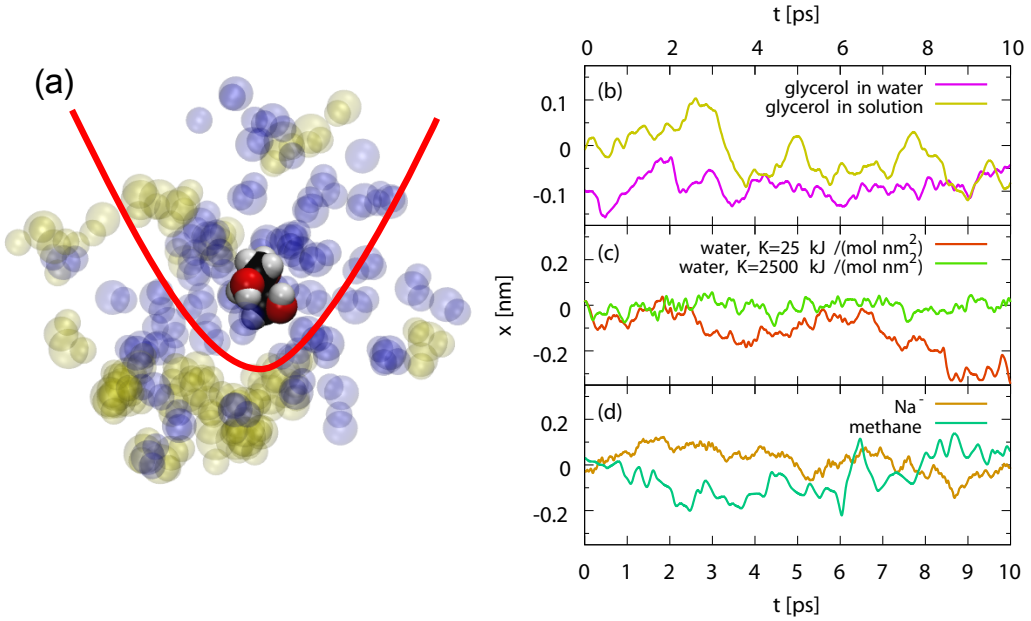

FIGURE 3.1: (a) Snapshot of a simulation of a glycerol molecule constrained by a harmonic potential (red) in a water-glycerol mixture, where the solvent water molecules are painted blue and the solvent glycerol molecules are painted yellow. Right: Trajectories of glycerol (b) in pure water (purple) and in a water–glycerol mixture (yellow) within a potential with $K = 250\ \mathrm{kJ/(mol\,nm^2)}$. In (c), we compare trajectories of a water molecule constrained by a potential with $K = 25\ \mathrm{kJ/(mol\,nm^2)}$ (red) and $K = 2500\ \mathrm{kJ/(mol\,nm^2)}$ (green). In (d), we show the trajectories of Na^- (brown) and methane (cyan) constrained by a potential with $K = 25\ \mathrm{kJ/(mol\,nm^2)}$.

All systems are simulated with the GROMACS 5.1 simulation package [95, 128]. For the water model we use SPC/E [99], the Lennard-Jones parameters for methane are taken from the GROMOS 53a6 force field [129], the parameters of the ions force fields are taken from the work of Dang et al. [130] and the glycerol force field is constructed by the Automated Topology Builder [131]. The Na^- has exactly the same parameters as the Na^+, only the sign of the charge is switched, thus representing an artificial ion, which in comparison to halogen ions has a smaller van-der-Waals radius by approximately 30 %.

All simulations are performed in an NVT ensemble with a time step of 2 fs at a temperature of $T = 300$ K, which is controlled by the velocity rescaling thermostat [101] coupled with a time constant of 0.5 ps to the solvent only. In Ref. [120] it was shown that the ensemble and the thermostat have no influence on the results. The simulation lengths vary from 268 to 537 ns ns for the simulations with pure water as solvent and from 800 ns to 2.68 μs for the water–glycerol mixtures, summing up to a total simulation time of 31 μs. Before the actual production runs, all systems are equilibrated for 5 ps in an NpT simulation using a Berendsen barostat [105] with $p = 1$ bar to adjust the box size. In the simulations with confined particles, we apply a three-dimensional harmonic potential with spring constants between $K = 25$ and $K = 25000\ \mathrm{kJ/(mol\,nm^2)}$ (up to $K = 2500\ \mathrm{kJ/(mol\,nm^2)}$ for water–glycerol mixtures) on the center of mass of the solute molecule. Additionally, we run simulations where we completely freeze the dynamics of the monoatomic molecules Na^+, Na^-, and methane (which in our simulations is modelled as a Lennard-Jones sphere). For water only the oxygen atom is frozen such that the rotational motion of the molecule is not

disturbed. In each simulation, we write out the position, the velocity, and the acceleration of the solute particle at every time step.

3.3.2 Memory Kernel Extraction

An iterative method for the extraction of memory kernels, which solves a discretized version of Eq. 3.4 for $\Gamma(t)$ with the correlation functions $\dot{C}^{vv}(t)$ and $C^{vv}(t)$ as input, was first discussed by Berne et al. in 1970 [63] for unconfined trajectories and later generalized to harmonically confined particles [125]. Already in Berne's original work it was remarked that it is advantageous in terms of stability to discretize the first derivative of Eq. 3.4, which leads to a Volterra equation of second kind (see Appendix 3.7.1). In the present work, we show that even better results are obtained when $G(t)$ instead of $\Gamma(t)$ is the function which is computed by an iterative algorithm, hence we employ a discretization of Eq. 3.5. Discretizing all functions as $G_i = G(i\Delta t)$, $C_i^{xx} = C^{xx}(i\Delta t)$ and $C_i^{vv} = C^{vv}(i\Delta t)$ with the time step Δt, the resulting iterative equation reads

$$G_i = \frac{2}{\Delta t\, C_0^{vv}} \left[m \frac{C_0^{vv}}{C_0^{xx}} C_i^{xx} - m C_i^{vv} - \sum_{j=0}^{i-1} \Delta t\, G_j C_{i-j}^{vv} w_{i,j} \right] , \tag{3.7}$$

where in the case of an unconfined particle the first term in brackets is replaced by mC_0^{vv}. We furthermore introduced the weighting factor $w_{i,j}$, with the values $w_{i,i} = w_{i,0} = 1/2$ and $w_{i,j} = 1$ otherwise, which comes from the trapezoidal integration rule. A derivation of the equation is provided in Sec. 3.8.6.

For $K = \infty$, where the solute molecule is frozen, the memory kernel is obtained by Eq. 3.2. As the solute molecule does not move in this case ($\dot{x} = 0$), the random force F_R acting on the molecule equals the total force F, which can easily be extracted from the simulations.

The performance of the algorithm in Eq. 3.7 is compared to Berne's original methods and shown to be improved (see Appendix 3.7.1). In Appendix 3.7.2 and 3.7.3, we review the direct computation of memory kernels via Fourier transform [123] and the parametrization of the memory kernels [120], respectively, and show that for particles in a harmonic potential the iterative method presented in this work yields the most robust results for the memory kernel.

Another iterative scheme can be derived for unconfined particles, as then Eq. 3.5 can be integrated twice more. The resulting equation

$$m\Delta x^2(t) - k_B T t^2 \; = - \int_0^t \mathrm{d}t''\, G(t'') \Delta x^2(t - t'') \, , \tag{3.8}$$

relates the memory kernel directly to the mean-squared displacement. In Appendix 3.7.4 we demonstrate that a discretized version of this equation can be used to compute memory kernels which are in perfect agreement with the results of Eq. 3.7.

3.4 Memory Kernels in Water

In the following, we investigate the memory kernels of methane, water, Na^+, Na^-, and glycerol in water. The choice of the molecules is motivated by the aim to analyze the effects of hydrophobicity (methane versus water), charge (Na^+ versus Na^-), and size (glycerol versus water) on the memory kernel. Spring constants are varied from $K = 25\,\mathrm{kJ/(mol\,nm^2)}$ to $K = 25000\,\mathrm{kJ/(mol\,nm^2)}$. According to the equipartition theorem, the corresponding positional fluctuations of the particle are in the range between $\sqrt{\langle x^2 \rangle} = \sqrt{k_B T/K} = 0.3$ nm for $K = 25\,\mathrm{kJ/(mol\,nm^2)}$, the length scale of van-der-Waals interactions, and $\sqrt{\langle x^2 \rangle} = 0.01$ nm for $K = 25000\,\mathrm{kJ/(mol\,nm^2)}$, the length scale of fluctuations in covalent bonds. Additionally, also the memory kernels of unconfined particles ($K = 0$) are computed.

In Fig. 3.2 (a) the results for $G(t)$ of methane in water are presented for all spring constants, which we compute using Eq. 3.7. The functions are monotonically increasing and reach a plateau for $t \to \infty$, which corresponds to the friction coefficient γ of the molecule. For the unconfined molecule ($K = 0$) the integral $G(t)$ saturates at a plateau value of $\gamma_0 = 1038\,\mathrm{g/(mol\,ps)}$, which is obtained by fitting a stretched exponential function to $G(t)$ in the interval $0.5\,\mathrm{ps} < t < 40\,\mathrm{ps}$ (see Sec. 3.8.7). In experiments, the diffusion coefficient of methane in water at $T = 298.15$ K [132] has been measured to be $D = 1.7 \cdot 10^{-5}\,\mathrm{cm^2/s}$, which corresponds to a friction coefficient of $1458\,\mathrm{g/(mol\,ps)}$, thus higher than the friction coefficient from our simulations. This difference presumably is mainly due to the force field, as the methane molecule in our simulations is modeled as a monoatomic Lennard-Jones sphere. Another source for deviations is the fact that SPC/E water has a reduced viscosity compared to experiments ($\eta_{\mathrm{SPC/E}} = 0.793 \cdot 10^{-3}$ Pa s [133] versus $\eta_{\mathrm{ex.}} = 0.86 \cdot 10^{-3}$ Pa s [134]) at 300 K, which according to Stokes' law leads to a reduced friction in the simulations.

We observe that the plateau height depends on the applied spring constant, with a ratio of 1.5 between the value of the frozen molecule γ_∞ and the unconfined molecule γ_0. Hence the confinement strongly modifies the friction which is acting between the methane molecule and the surrounding water. The same picture is also found for all other molecules in Fig. 3.2 (b)–(e). For unconfined water we measure a plateau value of $\gamma_0 = 0.924\,\mathrm{kg/(mol\,ps)}$ in $G(t)$, thus in very good agreement with the literature values of SPC/E water computed from mean-squared displacements at the temperature $T = 298.15$ K, which are between $0.996\,\mathrm{kg/(mol\,ps)}$ [135] and $0.901\,\mathrm{kg/(mol\,ps)}$ [136]. But again, with increasing confinement strength the plateaus of $G(t)$ shift to higher values, resulting in a ratio of $\gamma_\infty/\gamma_0 = 1.5$. For all other investigated molecules, the confinement-induced change of the friction is less pronounced, but still clearly detectable. Our results are summarized in Table 3.1, where the friction coefficients γ_0 of the unconfined molecules are displayed, and Fig. 3.3, where we present the relative change of the friction coefficient $\gamma(K)/\gamma_0$ for all investigated molecules. We observe that the ratio $\gamma(K)/\gamma_0$ decreases with increasing γ_0, i.e., molecules with large friction coefficients experience only small modifications. The dependence of γ_0 on molecule parameters however is complex: For example, both ions exhibit larger friction coefficients than water and methane, which are uncharged molecules of similar size, with the friction coefficient of Na^- being even larger than the

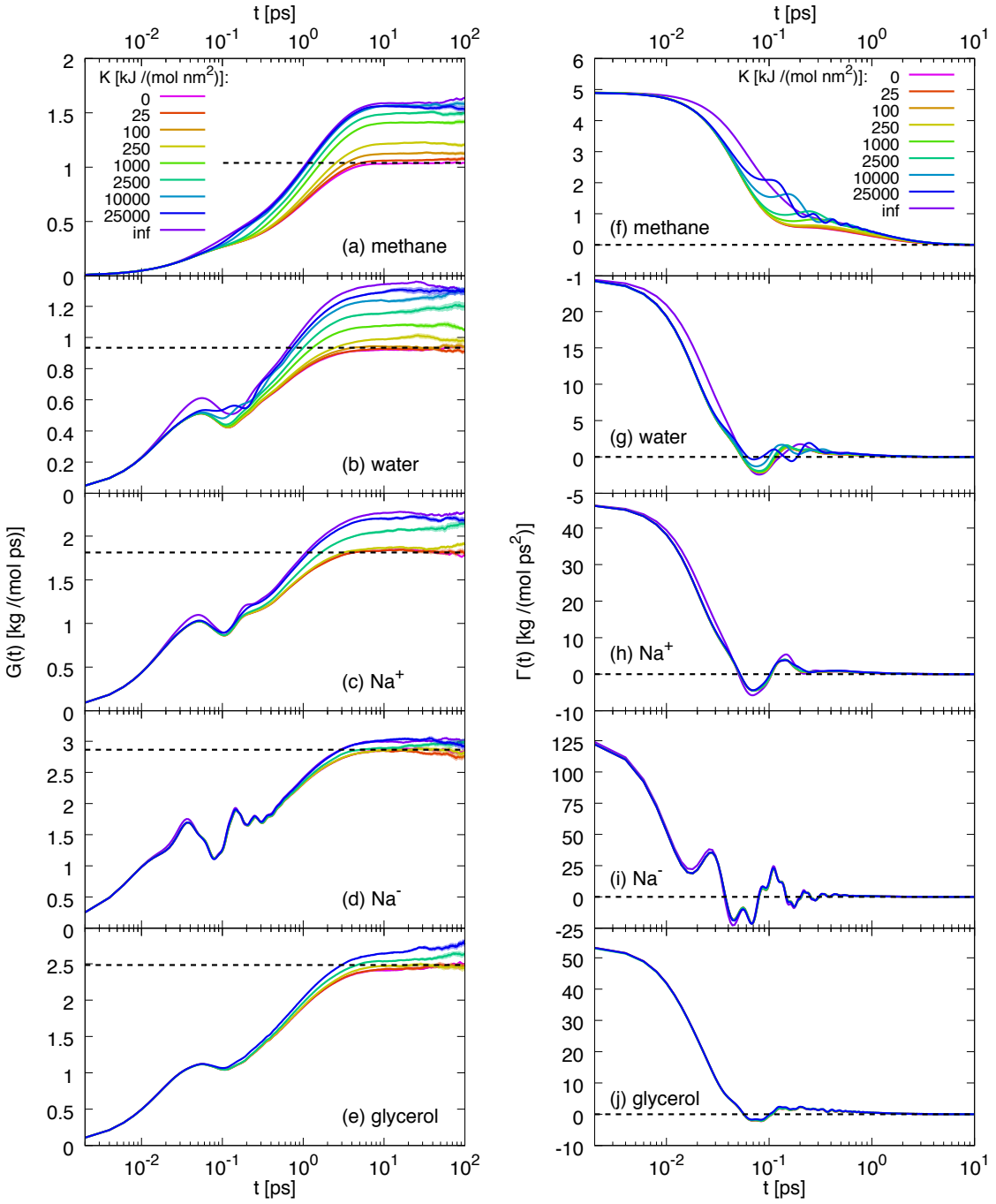

FIGURE 3.2: Left: $G(t)$ obtained by Eq. 3.7 for (a) methane, (b) water, (c) an Na^+-ion, (d) an Na^+-ion, and (e) glycerol for several spring constants between $K = 0$ and $K = 25000$ kJ/(mol nm^2), together with the $G(t)$ of the frozen solutes. Dashed black lines indicate the friction coefficient $\gamma = k_B T / \int_0^\infty \mathrm{d}t\, C^{vv}(t) = 2k_B T / \left(\mathrm{d}\Delta x^2/\mathrm{d}t\right)$ computed from the mean-squared displacements $\Delta x^2(t)$ of the unconfined molecules. Right: Corresponding memory kernels $\Gamma(t)$ computed by numerical differentiation of $G(t)$ using the midpoint formula.

one of glycerol. On the other hand, comparing the results of water and glycerol with each other, which both are hydrophilic and polar molecules, it transpires that also the molecular size alters γ_0, as expected from Stokes' law, and thus also $\gamma(K)/\gamma_0$. We therefore conclude that the confinement-dependence of the friction coefficient is not only a size effect, but also the charge is playing a significant role.

Molecule	methane	water	Na^+	Na^-	glycerol
γ_0 [kg/(mol ps)]	1.038	0.924	1.851	2.888	2.433

TABLE 3.1: Friction coefficients γ_0 for unconfined molecules.

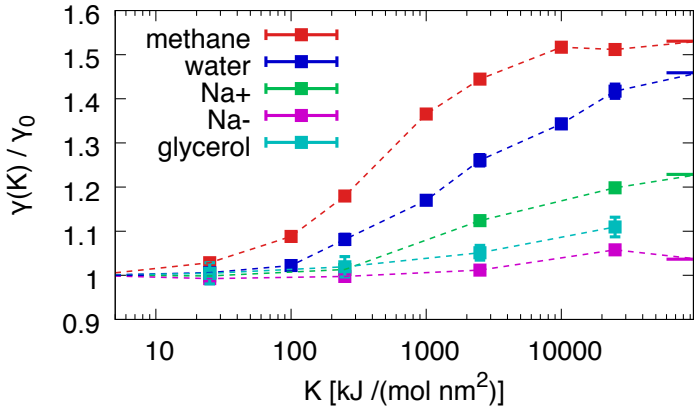

FIGURE 3.3: Rescaled friction coefficient $\gamma(K)/\gamma_0$ as a function of the spring constant K for methane (red), water (blue), Na^+ (green), Na^- (purple), and glycerol (cyan), where γ_0 refers to the friction coefficient of the unconfined particle.

In order to gain more insight into the mechanisms of the confinement-dependent friction, we take a look at the memory kernels $\Gamma(t)$ of all molecules, which we calculated from the $G(t)$ by numerical differentiation. Starting again with methane (Fig. 3.2 (f)), we observe that for small spring constants the memory kernels decay on two time scales with time constants of approximately $\tau_1 = 0.05$ ps and $\tau_2 = 1$ ps. For $K > 1000$ kJ/(mol nm^2), an additional shoulder in the memory kernel is developed at intermediate time scales. The shoulder was already observed in our previous work and was explained by a dynamic interplay of the harmonic oscillations of the methane molecule with the solvent relaxation [120]. This shoulder is followed by a small oscillation in the memory kernel for $K > 10000$ kJ/(mol nm^2), which is superposing the long time decay and is damped with increasing time. The memory kernels of the water molecule (see Fig. 3.2 (g)) exhibit a more complex time dependence than the methane molecules: All kernels exhibit a short time decay, followed by a minimum below zero at times $t \approx 0.08$ ps. Thereafter, a series of maxima and minima is formed in each kernel, whose positions and heights depend on the applied spring constant. Especially the memory kernels with spring constants $K > 10000$ kJ/(mol nm^2) deviate strongly from the rest of the memory kernels of water at times around $t \approx 0.1$ ps.

Unlike water and methane, the memory kernels of Na^+ (Fig. 3.2 (h)), Na^- (Fig. 3.2 (i)), and glycerol (Fig. 3.2 (j)) do not change their shape qualitatively at short time scales $t < 0.3$ ps when a harmonic potential is applied. Still, we observe the shift of the plateaus in $G(t)$, which can be understood by looking at Fig. 3.4, where exemplarily the memory kernels of a Na^+-ion are presented in a log-lin representation for the cases $K = 0$ and $K = 25000\ \mathrm{kJ/(mol\,nm^2)}$. For small spring constants the long time decay of the memory kernel, i.e. the decay for times longer than 1 ps, is located below the memory kernel of the strongly constrained particle. This is in agreement with the functions $G(t)$ of all molecules, as they mainly start to separate at times $t > 0.3$ ps. In other words, the confinement-dependence of the friction is to a large degree due to the slowest decay of the memory kernel. Note however that for the data obtained from the simulations it was not possible to distinguish whether it is the amplitude or the time constant of the slowest decay which is affected by the constraining potential (See Sec. 3.8.8).

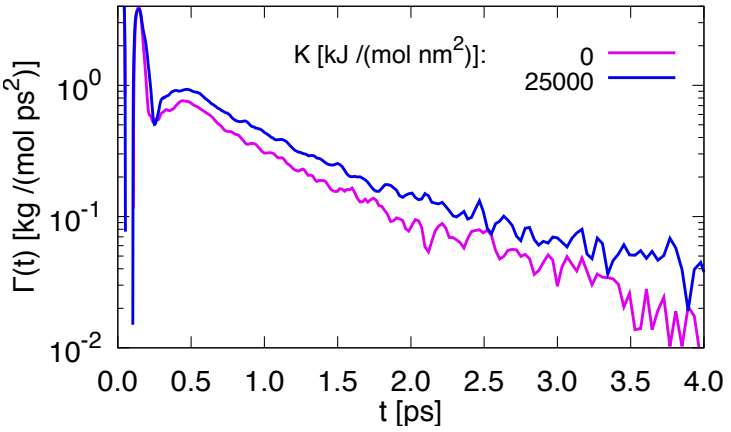

FIGURE 3.4: Memory kernels $\Gamma(t)$ of a Na^+-ion in the unconfined case ($K = 0$) and in a harmonic potential with $K = 25000\ \mathrm{kJ/(mol\,nm^2)}$ in a log-lin representation.

As amply discussed in literature, molecular friction is connected to hydration shell dynamics [137]. We thus analyze the orientational autocorrelation functions of the water molecules that are found in the first hydration shell of the solute at an initial time $t = 0$. We define the first hydration shell by all water molecules that are located relative to the solute within a distance d_0 given by the first minimum of the solute–water radial distribution function (shown in Sec. 3.8.9), i.e. $d_0 = 0.49$ nm for methane, $d_0 = 0.40$ nm for water, $d_0 = 0.32$ nm for Na^+, $d_0 = 0.32$ nm for Na^-, and $d_0 = 0.62$ nm for glycerol. The orientational autocorrelation functions are defined by

$$C_{\mathrm{rot}} = \langle P_2(\boldsymbol{u}(t)\boldsymbol{u}(0)) \rangle \ , \tag{3.9}$$

where $P_2(x) = (3x^2 - 1)/2$ denotes the second Legendre polynomial and $\boldsymbol{u}$ refers to each OH vector of the hydration water molecules, and they are shown exemplarily for methane in Fig. 3.5 (a). The rotational correlation functions exhibit a fast initial decay, followed by an exponential long time tail with the time constant τ_{rot}. The numerical value of this time constant is obtained by a fit of the function $C_{\mathrm{rot}}(t) = C_0 \exp(-t/\tau_{\mathrm{rot}})$ to the rotational correlation function. For all molecules, the decay time τ_{rot} increases with the strength of

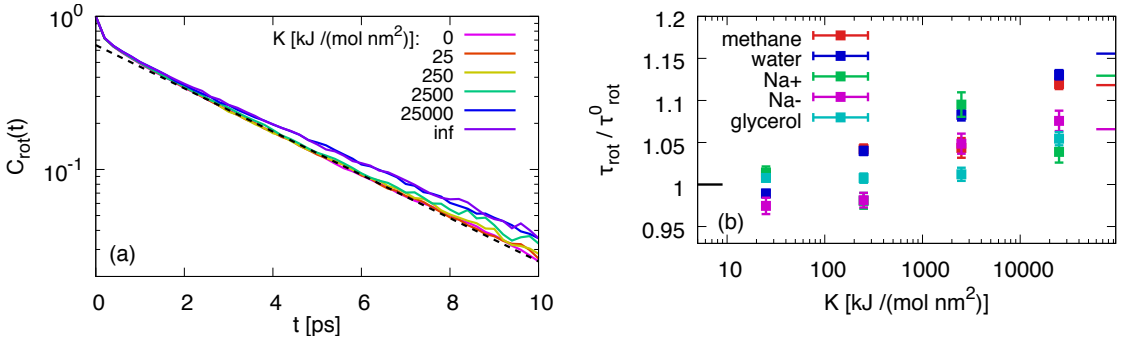

FIGURE 3.5: (a) Rotational autocorrelation functions $C_{\mathrm{rot}}(t)$ defined in Eq. (3.9) of water molecules found in the first hydration shell for methane for various potential strengths K. The black dashed line indicated a fit of the function $C_{\mathrm{rot}}(t) = C_0 \exp(-t/\tau_{\mathrm{rot}})$ to the data for $K = 0$. (b) Rescaled decay time $\tau_{\mathrm{rot}}/\tau^0_{\mathrm{rot}}$ of the orientational autocorrelation function for all molecules as a function of the spring constant, where $\tau^0_{\mathrm{rot}} = \tau_{\mathrm{rot}}(K = 0)$.

the confining potential, as can be seen in Fig. 3.5 (b). This increase is most pronounced for water, where it is about 15 %, while for glycerol and Na^- we still measure an increase of about 5 %. Thus, similar to the experiments, we observe a relative slowdown of the hydration shell dynamics that is correlated with the magnification of the friction in confinement.

3.5 Memory Kernels in Water–Glycerol Mixtures

In the following, we investigate the influence of the solvent viscosity on the memory kernels by solvating a glycerol molecule in mixtures of water and glycerol with four different mass ratios (See Table 3.2), hence obtaining solvents with four different viscosities. The values for the viscosities (denoted by η_{MD}) are taken from the work of Schulz et al. [133], where a Maxwell model is used to describe the full viscosity spectrum of water–glycerol mixtures in MD simulations. These values are in good agreement with the empirical formula by Cheng [138], which interpolates viscosities of water–glycerol mixtures based on data from experiments (denoted by $\eta_{\mathrm{ex.}}$)

System	mass fraction of glycerol	η_{MD} $[10^{-3}\ \mathrm{Ns/m^2}]$	$\eta_{\mathrm{ex.}}$ $[10^{-3}\ \mathrm{Ns/m^2}]$
1	0.0	0.77 ± 0.08	0.86
2	0.333	2.26 ± 0.25	2.27
3	0.434	3.70 ± 0.40	3.42
4	0.500	5.40 ± 0.50	4.67

TABLE 3.2: Composition of systems with water–glycerol mixture as solvent and their viscosities. The simulation values are taken from [133] and experimental values from [138].

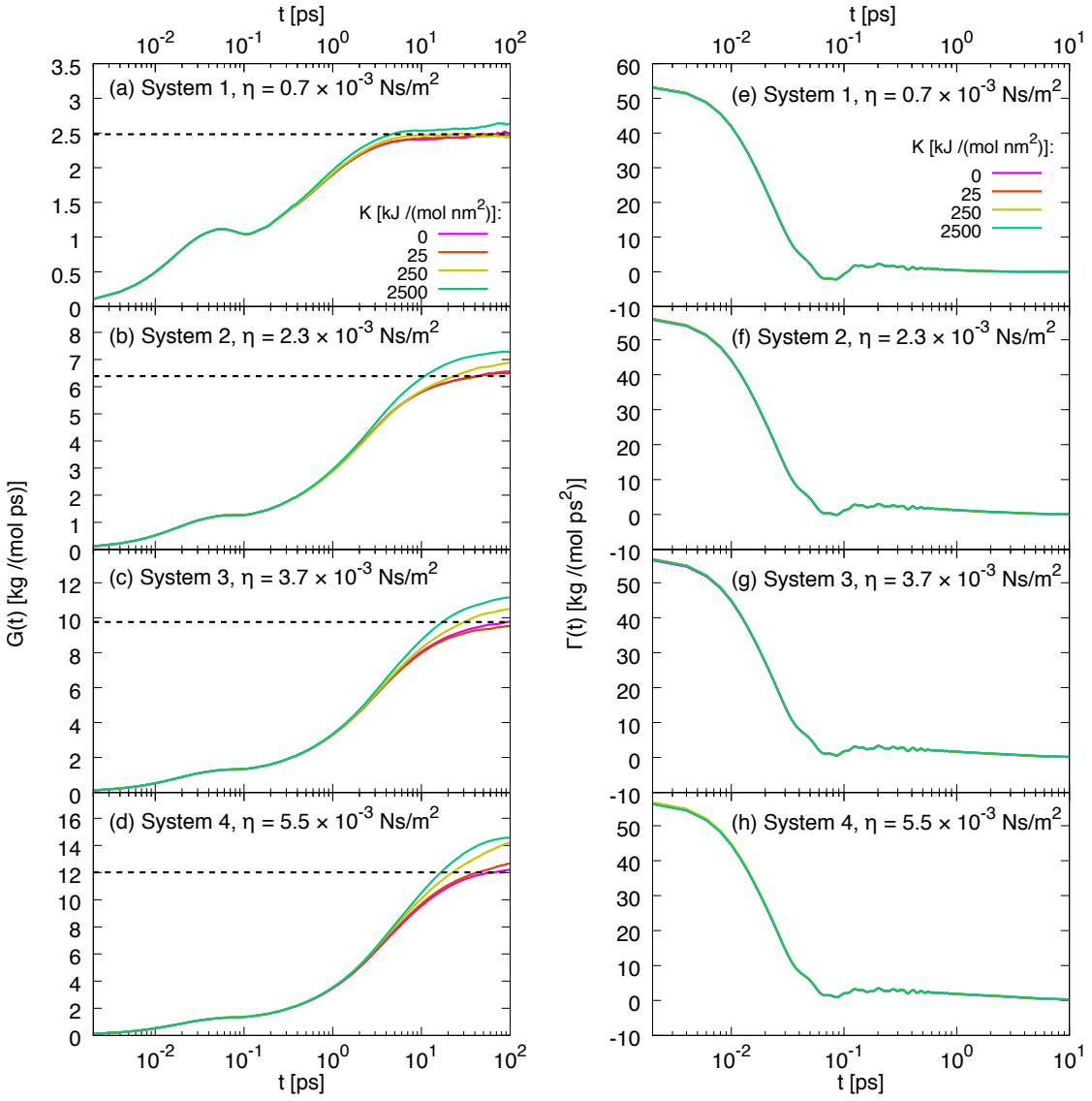

FIGURE 3.6: Left: $G(t)$ obtained by Eq. 3.7 for glycerol in the water–glycerol mixture with viscosities $\eta = 0.77 \cdot 10^{-3}$ Ns/m^2 (a), $\eta = 2.26 \cdot 10^{-3}$ Ns/m^2 (b), $\eta = 3.7 \cdot 10^{-3}$ Ns/m^2 (c), and $\eta = 5.4 \cdot 10^{-3}$ Ns/m^2 (d) for 4 spring constants between $K = 0$ and $K = 2500$ kJ/(mol nm^2). Dashed black lines indicate the friction coefficient $\gamma = k_B T / \int_0^\infty \mathrm{d}t\, C^{vv}(t) = 2k_B T / \left(\mathrm{d}\Delta x^2/\mathrm{d}t\right)$ computed from the mean-squared displacements $\Delta x^2(t)$ of the unconfined molecules. Right: Corresponding memory kernels $\Gamma(t)$ computed by numerical differentiation of $G(t)$.

In Fig. 3.6 we present the memory kernels $\Gamma(t)$ and their integrals $G(t)$ of a glycerol molecule in the water–glycerol mixtures characterized in Table 3.2. Again, $G(t)$ is computed via Eq. 3.7 and $\Gamma(t)$ by numerical differentiation of $G(t)$. We observe that there are two effects on the memory kernels, one related to the viscosity and one to the confinement:

The first effect corresponds to Stokes' law, as with increasing solvent viscosity the friction coefficient, represented by the plateau of $G(t)$, shifts to higher values. This is shown in Fig. 3.7 (b), where the total height of the bars corresponds to the friction coefficient γ_0 of the unconfined glycerol molecule at given solvent viscosity η. In this figure, γ_0 is

computed from fits of stretched exponential functions to $G(t)$ (see Sec. 3.8.7). The relation between friction coefficient and viscosity can within the error bars be described by Stokes' law $\gamma = 6\pi\eta R_{\text{hyd}}^{\text{sim}}$ and a least-square fit of this linear function (dashed line) to the data yields a hydrodynamic radius of $R_{\text{hyd}}^{\text{sim}} = 0.236 \pm 0.017$ nm for the glycerol molecule. The experimental value of $R_{\text{hyd}}^{\text{exp}} = 0.26$ nm [139], computed via the Stokes-Einstein relation from diffusion coefficients, is slightly larger, which goes in hand with a smaller friction coefficient of glycerol in simulations ($\gamma_0 = 2.433$ kg/(mol ps)) compared to experiments ($\gamma_{\text{ex.}} = 2.67$ kg/(mol ps) computed from the diffusion coefficient via Stokes-Einstein) [140]. The increase of the friction coefficient with the viscosity results from the long time behavior of the $\Gamma(t)$: As it is revealed in Fig. 3.7 (a), all memory kernels exhibit a very similar shape apart from a small constant offset for times $t \lesssim 0.5$ ps. Thus, the short time behavior of the memory kernels is nearly independent of the solvent viscosity. On the other hand, for times $t > 0.5$ ps all memory kernels differ in their long time decay, which is most strikingly visible in the log-lin representation in the inset of Fig. 3.7 (a). In this figure, fits of triple exponential functions,

$$\Gamma^{\text{exp}}(t) = \sum_{i=1}^{3} A_i \, \mathrm{e}^{-t/\tau_i^L} \,, \tag{3.10}$$

with $\tau_1^L < \tau_2^L < \tau_3^L$, to the to the long time decay of the memory kernels (see Sec. 3.8.8 for fitting details) are displayed as dashed lines. The integral over $\Gamma^{\text{exp}}(t)$ yields the long time contribution $\gamma^L = \gamma_1^L + \gamma_2^L + \gamma_3^L$ to the friction coefficient γ_0, where $\gamma_i^L = A_i \tau_i^L$ with $i = 1, 2, 3$. Each contribution γ_i^L is indicated in Fig. 3.7 (b) together with the short time contribution $\gamma_s = \gamma_0 - \gamma^L$. There we observe that γ_s and γ_1^L remain constant for all viscosities, whereas γ_2^L and γ_3^L increase with the viscosity. A comparison of the two contributions γ_2^L and γ_3^L with each other reveals that the more the viscosity increases, the more important the contribution of the longest decay becomes. The amplitudes A_i and decay times τ_i^L for the two longest decays are summarized in Table 3.3, where it can be seen that all fit parameters increase with the viscosity. For larger viscosities than simulated in this work,

System	1	2	3	4
η_{MD} [10^{-3} Ns/m^2]	0.77	2.26	3.70	5.4
A_2 [kJ/(mol ps^2)]	0.42	1.52	1.92	1.99
τ_2^L [ps]	1.71	2.11	2.47	2.80
A_3 [kJ/(mol ps^2)]	0.0	0.174	0.284	0.381
τ_3^L [ps]	-	8.75	11.56	13.03

TABLE 3.3: Amplitudes A_2, A_3 and decay times τ_2^L, τ_3^L from fits of the function Eq. 3.10 to the memory kernels $\Gamma(t)$ (see Fig. 3.7).

we assume that the value $\Gamma(0)$ remains independent of the viscosity, as it is observed in Fig. 3.6. This means that the amplitudes A_2 and A_3 will saturate by further increasing the viscosity, which is already observed for A_2 in our simulations. In this case, the only possibility to increase the friction coefficient γ_0 is then increasing the decay times τ_i^L. By

denoting the set of decay times τ_i^L by an effective decay time τ^L, this assumption then yields that $\tau^L \sim \gamma_0 \sim \eta$, where the last proportionality comes from Stokes' law.

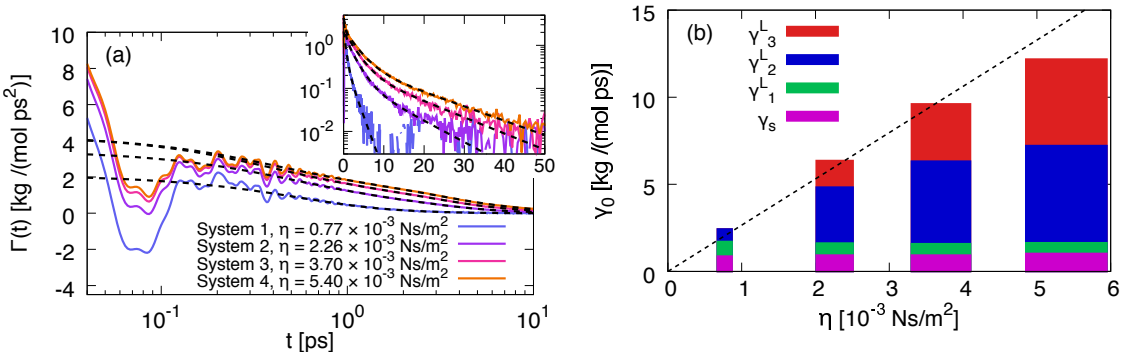

FIGURE 3.7: (a) Comparison of the memory kernels of unconfined glycerol molecules in four solvents composed of different mixtures of water and glycerol corresponding to four different viscosities. For times $t > 0.6$ ps, Eq. 3.10 is fitted to the kernels (black dashed lines). Inset: The same data in a log-lin representation. (b) Friction coefficient γ_0 of an unconfined glycerol molecule and its contributions for all simulated solvent viscosities η. The total height of each bar corresponds to the γ_0, which is computed from fits of stretched exponential functions to $G(t)$ (see Sec. 3.8.7). To this data, a linear function according to Stokes' law $\gamma(\eta) = 6\pi\eta R_{\mathrm{hyd}}$ is fitted (dashed line), with the result $R_{\mathrm{hyd}} = 0.236$ nm. For each γ_0, the long time contributions $\gamma_i = A_i\tau_i^L$, which are computed from fits of Eq. 3.10 to $\Gamma(t)$, and the short time contribution $\gamma_s = \gamma_0 - \gamma_1^L - \gamma_2^L - \gamma_3^L$ are indicated as colored areas.

We now turn to the confinement-related effect; we observe that confinement-dependent friction, which was already discussed in the previous section for particles solvated in water, is magnified with increasing solvent viscosity. This is shown in Fig. 3.8, where we compute the relative change of the friction coefficient $\gamma(K)/\gamma_0$ for all water–glycerol mixtures. In pure water, the friction coefficient increases only up to 5 % with confinement, whereas in system 4, where the viscosity is 7 times higher, this value changes to more than 20 %. This amplification can be understood by a scaling argument (see Fig. 3.9):

The transition between inertial and diffusive behavior of a solute particle takes place at a time scale $\tau_{\mathrm{m}} \simeq m/\gamma \sim \rho R^2/\eta$ with the solute mass density ρ, where the last proportionality comes from Stokes' law $\gamma = 6\pi\eta R$. The dependence of τ_{m} on the solute radius R and the viscosity η is indicated by a red arrow. Considering a solute particle that is confined by a harmonic potential, the transition between an oscillatory motion with the time scale $\tau_{\mathrm{osc}} \simeq 2\pi\sqrt{m/K}$ and overdamped motion with the time scale $\tau_\gamma \simeq 2\pi\gamma/K$ happens at the spring constant $K_{\mathrm{trans}} \simeq \gamma^2/m \simeq \gamma/\tau_{\mathrm{m}}$, where $\tau_{\mathrm{osc}} \simeq \tau_\gamma \simeq \tau_{\mathrm{m}}$. In other words, the time scale τ_m also determines the transition from oscillatory to overdamped motion.

The other relevant time scale is the solvent relaxation time τ^L, which we have argued to be proportional to the solvent viscosity $\tau^L \sim \eta$ (yellow arrow). With the two time scales τ_m and τ^L, there exist two possible scenarios: For $\tau_{\mathrm{m}} > \tau^L$, which is the case at low viscosities or for massive particles, the solvent relaxes before the transition from inertial to overdamped diffusive motion of the solute particle, hence there is no dynamic coupling between solute diffusion and solvent relaxation. In this limit, which corresponds to the upper left region of Fig. 3.9, we do not expect the friction to be affected by the confinement.

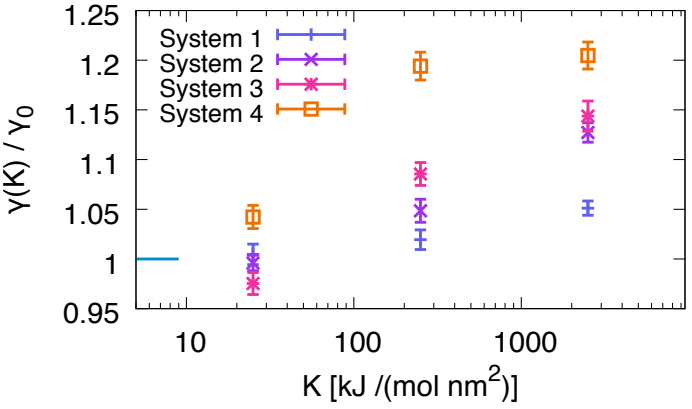

FIGURE 3.8: Friction coefficient of a glycerol molecule γ as a function of the applied confining potential K for four solvents with different viscosities. All values are normalized with respect to the unconfined case.

On the other hand, for $\tau_m \lesssim \tau^L$ the solute particle dynamics becomes diffusive and overdamped before the solvent relaxes and a dynamic coupling between the solvent relaxation and the particle motion emerges. This situation can be realized by either increasing the solvent viscosity or decreasing the solute size (lower right region in Fig. 3.9). The effects of changes in viscosity and solute size can be estimated by the relation $\tau^L \simeq \tau_m$, which leads to $R^2/\eta \sim \eta$ and thus $R^2 \sim \eta^2$. This means that, if all other parameters are left constant, an increase or decrease of the solute size R requires an adjustment of the viscosity η of the same order of magnitude in order to keep the confinement-dependence of the friction constant. This is indicated by the background color in Fig. 3.9, where for darker colors the confinement-dependence of the friction is expected to be more pronounced.

3.6 Conclusions

In this work, a novel method for the calculation of memory kernels from trajectories has been introduced in the framework of the generalized Langevin equation. This method is an integrated version of the iterative scheme published in [63] and it has been shown that, in the case of confined particles and complicated memory kernels, it yields more stable results compared to a computation via Fourier transform [123] or parametrization [120].

This method has been applied to compute memory kernels and the friction coefficient for five different solutes (methane, water, Na^+, Na^-, glycerol) in water. A confinement-dependent increase of the friction has been discovered for all investigated solutes. For molecules with a small friction coefficient this effect is most pronounced, still it is clearly present also for polyatomic molecules such as glycerol. An analysis of the memory kernels has disclosed that the increase of the friction mainly stems from their long time contribution. The confinement-dependent friction goes in hand with a slowdown of water dynamics in the hydration shell of the particles, which has been observed in the increase of the decay time of the orientational correlation functions. By increasing the viscosity of the

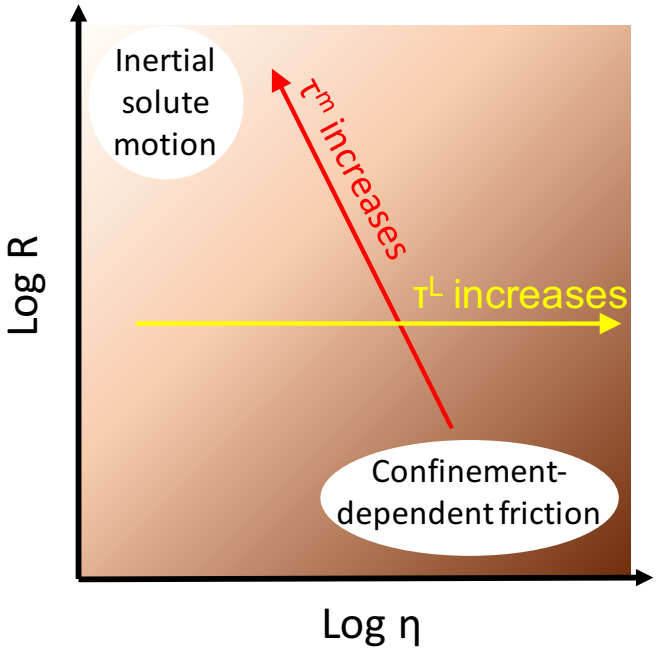

FIGURE 3.9: Schematic illustration of the dependence of τ_m and τ^L on the viscosity η and the particle radius R. The solvent relaxation time τ^L (yellow arrow) is proportional to the viscosity η. The dependence of the time scale τ_m, which marks the transition from an inertial to a diffusive behavior of the solute, on η and R is indicated by the red arrow. The importance of confinement-dependent friction is illustrated by the background color, with dark colors corresponding a pronounced dependence.

solvent the confinement-dependence of the friction coefficient is magnified, hence it is possible to expand this effect from the molecular to the microscale by using highly viscous fluids as solvents. In particular polymer melts provide a possibility to measure confinement-dependent friction in experiments, since the relaxation times of polymer melts, and thus also their viscosity, scale as a power law with the polymer length [141]. Furthermore, particles with a radius of down to 9 nm have been trapped [142] in optical tweezers, which is only one and a half orders of magnitude larger than the glycerol molecule investigated in our simulations. Thus, the combination of nanosized particles as solutes and polymer melts as solvents provides an excellent experimental setup [143], since, according to our estimation in the discussion section, an increase of the solvent viscosity by a factor of 50 compared to our simulations should be sufficient to induce confinement-dependent friction in such experiments.

Another important consequence of the confinement-dependent friction relates to the computation of diffusivities in simulations: Restraining the dynamics of particles in inhomogeneous systems, a method applied in simulations in order to compute spatially resolved diffusion profiles for example in lipid bilayers [34, 144], yields higher friction coefficients and thus lower diffusivities. A variation of the confinement strength in the simulations is advisable in order get an estimation of the confinement-dependence of the friction in such systems.

3.7 Appendix

3.7.1 Iterative Extraction of Memory Kernels

In order to capture the long-time behavior of the particle motion, it is important to resolve the plateaus of $G(t)$, which develop at times $t > 2$ ps. Here we show that this task is not always accomplished by iterative methods which are based on a direct extraction of $\Gamma(t)$ from the simulations and a subsequent integration in order to obtain $G(t)$. In literature, Volterra equations of first kind as well as second kind have been utilized as a basis for the iterative computation of $\Gamma(t)$. The Volterra equation of second kind can be derived from the Volterra equation of first kind in Eq. 3.4 by taking the time derivative, which leads to

$$C^{FF}(t) = \int_0^t \mathrm{d}t'\, \Gamma^\star(t') C^{vF}(t-t') + m\Gamma^\star(t) C^{vv}(0)\,, \tag{3.11}$$

where the total force acting on the particle is denoted by $F = m\dot{v}$. Discretizing the Eqs. 3.4 and 3.11 and solving them for $\Gamma_i^\star = \Gamma_i + K$ we arrive at

$$\Gamma_i^\star = -\frac{2}{\Delta t\, C_0^{vv}} \left[C_i^{vF} + \sum_{j=0}^{i-1} \Delta t\, \Gamma_j^\star C_{i-j}^{vv} w_{i,j} \right] \tag{3.12}$$

$$\Gamma_i^\star = \frac{1}{m C_0^{vv}} \left[C_i^{FF} - \sum_{j=0}^{i-1} \Delta t\, \Gamma_j^\star C_{i-j}^{vF} w_{i,j} \right]\,. \tag{3.13}$$

A derivation of these equations is given in Sec. 3.8.6. These equations are the iterative schemes that have been used to compute memory kernels from particle trajectories in previous works [124, 126]. In Fig. 3.10, we compare he performance of these two methods to our iterative scheme in Eq. 3.7 on the basis of the memory kernels of methane for the spring constants $K = 0$, $K = 100$ kJ/(mol nm^2) and $K = 25000$ kJ/(mol nm^2). In the subplots (a) to (c), where the memory kernels $\Gamma(t)$ are shown, it is visible that both methods Eqs. 3.12 and 3.13 suffer from numerical instabilities: While Eq. 3.12 produces oscillations in the memory kernel, seen most evidently for the unconfined methane molecule at times $t > 0.1$ ps, the memory kernel computed by Eq. 3.13 diverges for the highest spring constant. The picture is even more obvious for the integrals $G(t)$ of the memory kernels, which are shown in the subfigures (d) to (f). In these figures the dashed lines indicate the values $\gamma_{xx} = k_\mathrm{B}T / \int_0^\infty \mathrm{d}t\, C^{vv}(t)$ without confinement and $\gamma_{vv} = K^2 \int_0^\infty \mathrm{d}t\, C^{xx}(t)/k_\mathrm{B}T$ with confinement (See Sec. 3.8.5 for derivation). Only Eq. 3.7, which solves the Volterra equation for $G(t)$, reproduces plateau values γ_{xx} and γ_{vv}, whereas the other two methods, where first $\Gamma(t)$ is computed and then integrated, exhibit massive deviations for times $t > 10$ ps. We thus conclude that indeed the method based on Eq. 3.7 provides the numerically most stable results for the memory kernel among the iterative methods.

3.7.2 Computation of Memory Kernels via Fourier transform

Instead of using iterative algorithms, it is also possible to calculate the memory kernel directly from the correlation functions using Fourier transforms [123]. In Fourier space,

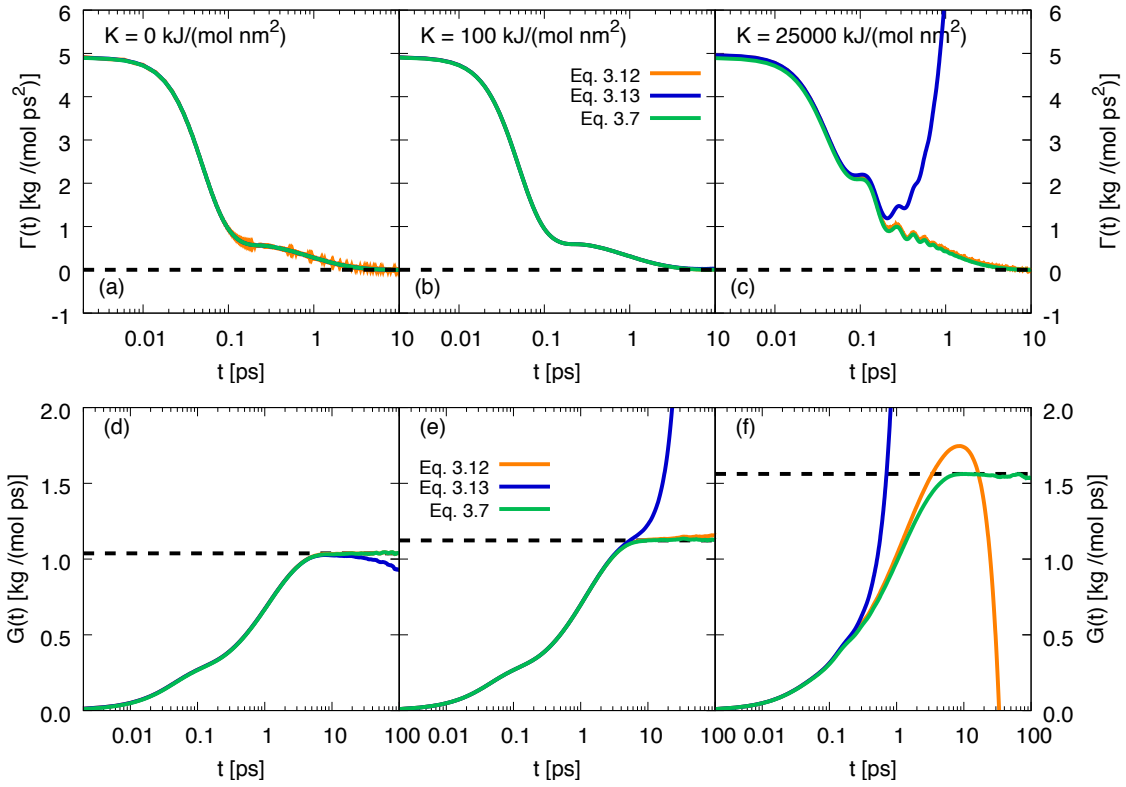

FIGURE 3.10: Memory kernels $\Gamma(t)$ of methane in water obtained from Eqs. 3.12 (orange), 3.13 (blue) and 3.7 (green) for three spring constants (a) $K = 0$, (b) $K = 100\ \mathrm{kJ/(mol\,nm^2)}$ and (c) $K = 25000\ \mathrm{kJ/(mol\,nm^2)}$. In the subfigures (d) to (f), the corresponding integrals $G(t)$ over the memory kernels are presented. Equations 3.12 and 3.13 yield $\Gamma(t)$, which has to be integrated numerically to obtain $G(t)$, whereas Eq. 3.7 yields $G(t)$, which has to be differentiated numerically to obtain $\Gamma(t)$. In the subfigures (d) to (f), the dashed lines indicate the values $\gamma = k_\mathrm{B}T / \int_0^\infty \mathrm{d}t\, C^{vv}(t)$ without confinement and $\gamma = K^2 \int_0^\infty \mathrm{d}t\, C^{xx}(t)/k_\mathrm{B}T$ with confinement.

the relation between the memory kernel and the velocity correlation function is given by

$$\tilde{\Gamma}(\omega) = 2\,\mathrm{Re}\left(\frac{k_B T}{\tilde{C}^{vv}_{+}(\omega)}\right) \tag{3.14}$$

$$\text{with} \qquad \tilde{C}^{vv}_{+}(\omega) = \int_0^\infty dt\, C^{vv}(t)\, \mathrm{e}^{-i\omega t}\,, \tag{3.15}$$

which is derived in Sec. 3.8.2. Hence, in order to obtain the memory kernel in the time domain, a Fourier transformation of the velocity correlation function according to Eq. 3.15 and a back Fourier transformation of the real part according to Eq. 3.14 is necessary.

The results of this method are presented in Fig. 3.11 (green lines) in the frequency domain ((a)-(c)), computed via Fast-Fourier transform, and the time domain ((d)-(f)) and compared to the iterative method based on Eq. 3.7 (blue lines) for the memory kernels of methane. For $K = 0$ and $K = 100\ \mathrm{kJ/(mol\,nm^2)}$, the results of both methods are indistinguishable from each other. Differences between the methods are visible for the spring constant $K = 25000\ \mathrm{kJ/(mol\,nm^2)}$. In frequency domain, we observe that at small frequencies, the memory kernel computed from the Fourier method suffers from heavy oscillations, which

are not seen in the other two kernels. In time domain, these oscillations correspond to a divergence of the kernel at large times. This instability has already been observed by Gottwald et al. [123], where a Gaussian filter was used in the Fourier transform to correct for it. We thus conclude that for small spring constants, both methods yield equivalent results, whereas for large spring constants, the Fourier-based method becomes unstable.

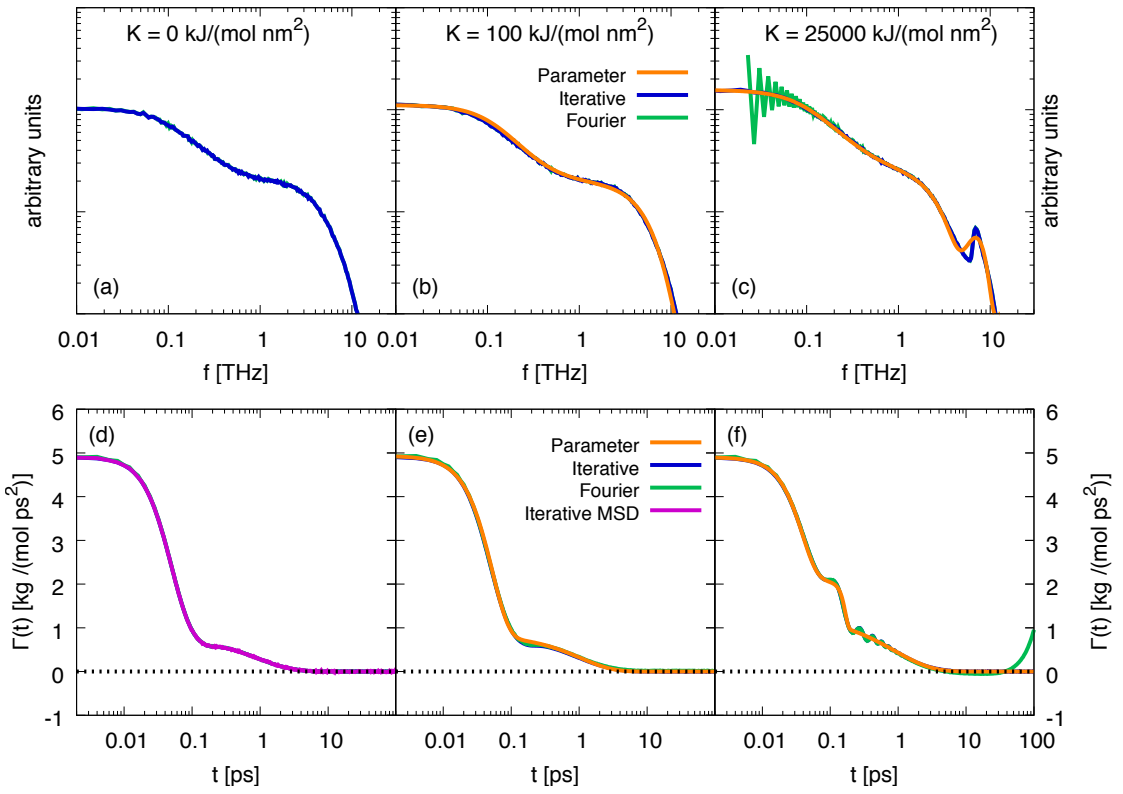

FIGURE 3.11: Fourier transforms of the memory kernels of methane obtained by the parameter-based method Eq. 3.20 (orange), the iterative method Eq. 3.7 (blue) and the Fourier-transform method Eq. 3.14 (green) for the spring constants (a) $K = 0$, (b) $K = 100$ kJ/(mol nm^2) and (c) $K = 25000$ kJ/(mol nm^2). In subfigures (d)-(f), the corresponding kernels in the time domain are presented. In (d), we additionally show the memory kernel $\Gamma(t)$ which results from the numerical differentiation of the $G(t)$ computed with MSD-based method in Eq. 3.22 (purple).

3.7.3 Parameter-based Extraction of Memory Kernels

A recently developed method utilizes a parameter-based ansatz function for the memory kernels, whose parameters are fitted such to reproduce the measured correlation functions [120]. Defining the force on a solute particle by

$$F_{\mathrm{sol}}(t) = m\ddot{x}(t) + Kx(t) \tag{3.16}$$

and the autocorrelation function of this force by

$$C_{FF}^{\mathrm{sol}}(t) = \langle F_{\mathrm{sol}}(0) F_{\mathrm{sol}}(t) \rangle \,, \tag{3.17}$$

we can compute the Fourier transform $\tilde{C}_{FF}^{\mathrm{sol}}(\omega) = \int_{-\infty}^{\infty} dt\, \mathrm{e}^{-i\omega t} C_{FF}^{\mathrm{sol}}(t)$ of this correlation function by solving the GLE in Eq. 3.3 in Fourier space. The solution reads

$$\tilde{C}_{FF}^{\mathrm{sol}}(\omega) = \frac{k_{\mathrm{B}} T\, \tilde{\Gamma}(\omega)}{\left|1 - i\omega \tilde{\Gamma}_{+}(\omega)/(m\omega^2 - K)\right|^2}\,, \tag{3.18}$$

where we introduced the single-sided memory function $\Gamma_{+}(t) \equiv \Gamma(t)$ for $t \geq 0$ and $\Gamma_{+}(t) \equiv 0$ for $t < 0$. As already pointed out in the main text, the friction coefficient γ is determined by $\gamma = \int_0^{\infty} dt\, \Gamma(t)$, which in the case of confined particles ($K \neq 0$) can be used to compute the friction coefficient directly from the correlation function $C_{FF}^{\mathrm{sol}}(t)$ via

$$\gamma \equiv \frac{\tilde{\Gamma}(0)}{2} = \frac{\tilde{C}_{FF}^{\mathrm{sol}}(0)}{2k_{\mathrm{B}}T} = \frac{1}{k_{\mathrm{B}}T} \int_0^{\infty} dt\, C_{FF}^{\mathrm{sol}}(t)\,. \tag{3.19}$$

For $K = 0$, the solvent force equals the total force on the particle and the integral over the autocorrelation function $C_{FF}^{\mathrm{sol}}(t)$ becomes zero, hence this method is not applicable for unconfined particles. Using a parametrization of $\Gamma(t)$, we can compute $C_{FF}^{\mathrm{sol}}(t)$ using Eq. 3.18 and fit the parameters such that the resulting correlation function agrees with the correlation function $C_{FF}^{\mathrm{sol}}(t)$ calculated from the simulation trajectories. This fitting procedure can be done simultaneously to both $C_{FF}^{\mathrm{sol}}(t)$ and its integral, hence ensuring that the integral of the resulting memory kernel $\Gamma(t)$ fulfills the relation $\gamma = \int_0^{\infty} \mathrm{d}t\, \Gamma(t)$. For the parametrization of the memory kernel of methane we choose

$$\Gamma(t) = \sum_{i=1}^{n} A_i \exp\left(-\left|\frac{t}{\tau_i}\right|^{\alpha_i}\right) \tag{3.20}$$

with $n = 2$ for $K = 100\ \mathrm{kJ/(mol\,nm^2)}$ and $n = 3$ for $K = 25000\ \mathrm{kJ/(mol\,nm^2)}$, where the A_i, τ_i and α_i are the fit parameters.

In Fig. 3.11, we compare the memory kernels of methane computed by this method (orange lines) with the iterative method based on Eq. 3.7 (blue lines) for the spring constants $K = 100\ \mathrm{kJ/(mol\,nm^2)}$ and $K = 25000\ \mathrm{kJ/(mol\,nm^2)}$. Similarly to the results of Appendix 3.7.2, we do not see any deviation between the parameter-based method and the iterative method for $K = 100\ \mathrm{kJ/(mol\,nm^2)}$. This means that in this case indeed the parametrization in Eq. 3.20 is sufficient to describe the memory kernel. At high frequencies, the Fourier-transformed memory kernels exhibit a minimum at 6 THz, followed by a maximum at 7 THz. This feature is identically generated by both the Fourier-based method and the iterative method, whereas the parameter-based method exhibits deviations. In the time domain, we observe that in contrast to the other two methods the parameter-based method does not produce the small oscillations at times $t > 0.2$ ps. These deviations are due to the limitations caused by the choice of the parametrization in Eq. 3.20, since for an accurate modeling of all features of the memory kernel more parameters are required. These limitations are even more obvious when one considers for example the modeling of a kernel as seen in Fig. 3.2 (h), where a huge amount of parameters is needed to reproduce all features of the kernel. Thus, the parameter-based method is a good choice for simple kernels with few features, where it yields stable results, however for more complicated kernels, the iterative method should be preferred.

3.7.4 Extraction of Memory Kernels from MSD

In the case of no confinement ($K = 0$), we can integrate Eq. 3.5 twice, which then results in the equation

$$m\Delta x^2(t) - k_B T t^2 = -\int_0^t \mathrm{d}t'' \, G(t'')\Delta x^2(t - t'') \,, \tag{3.21}$$

where $\Delta x^2(t)$ is the mean-squared displacement (MSD) of the particle. A detailed derivation is given in Sec. 3.8.4. The discretization of this equation yields

$$G_i = \frac{1}{\Delta t \, \Delta x_1^2} \left[k_B T \left((i+1)\Delta t \right)^2 - m\Delta x_{i+1}^2 - \sum_{j=0}^{i-1} \Delta t \, G_j \Delta x_{i+1-j}^2 \right] . \tag{3.22}$$

With this equation, the computation of memory kernels for $K = 0$ is possible for systems where velocities are not accessible (or only via numerical differentiation). As can be seen in Fig. 3.11 (d), we obtain perfect agreement between this method (purple line) and all other methods for the memory kernel of methane.

3.8 Supplementary Material

3.8.1 Initial Time in the GLE

In order to demonstrate that the initial time in the GLE in Eq. 3.1, i.e. the choice of either t or ∞ as upper integration boundary, does not have any effect on Eqs. 3.4 and 3.5 in the main text, we first have a short revision of how Mori motivated the formulation of the GLE.

3.8.1.1 Motivation of GLE by Mori

In his original work [42], Mori considers a Brownian particle whose motion is described by a dynamic variable, which we in our notation call $\dot{x}(t)$. The dynamics of $\dot{x}(t)$ is determined by the force $F(t)$ acting on the Brownian particle, which Mori separates into a contribution $F_1(t)$, which depends on the history of $\dot{x}(t)$ up to an initial time t_0, and a contribution $F_2(t)$ that is independent of $\dot{x}(t)$ and stems from the other degrees of freedom that couple to $\dot{x}(t)$. The equation of motion thus reads

$$m\ddot{x}(t) = F(t) = F_1(\dot{x}(t'), t \geq t' \geq t_0) + F_2(t) \,. \tag{3.23}$$

In this equation, Mori splits the force F_1 into a part which is linear in $\dot{x}(t')$ and a part containing all higher orders of $\dot{x}(t')$. Denoting the sum of this second part and $F_2(t)$ as the random force $F_R(t)$, Mori arrives at

$$m\ddot{x}(t) = -\int_{t_0}^t \mathrm{d}t' \, \Gamma(t - t')\dot{x}(t') + F_\mathrm{R}(t) \,. \tag{3.24}$$

In this equation, the function $\Gamma(t)$, which we will in the following denote as the memory kernel, describes the linear coupling of the history of $\dot{x}(t)$ to the dynamics of $\dot{x}(t)$ at present time. By setting the initial time to $t_0 = 0$, we obtain Eq. 3.1 in the main text. Using the projector operator formalism Mori further showed that with this choice for the initial time the random force $F_R(t)$ is not correlated to the initial value $\dot{x}(0)$,

$$\langle F_R(t)\dot{x}(0)\rangle = 0, \tag{3.25}$$

which then leads to the relation

$$\left\langle F_R(t)F_R(t')\right\rangle = k_B T\Gamma(t-t') \tag{3.26}$$

for the correlator of the random force, which is often referred to as the fluctuation-dissipation theorem.

Equation 3.24 can be modified such that the history of the process reaches infinitely into the past, which results in

$$\begin{aligned} m\ddot{x}(t) &= -\int_{-\infty}^{t} \mathrm{d}t'\,\Gamma(t-t')\dot{x}(t') + F'_{\mathrm{R}}(t) \\ \text{with} \qquad F'_{\mathrm{R}}(t) &= \int_{-\infty}^{t_0} \mathrm{d}t'\,\Gamma(t-t')\dot{x}(t') + F_{\mathrm{R}}(t)\,, \end{aligned} \tag{3.27}$$

thus the random force $F'_{\mathrm{R}}(t)$ differs from the random force $F_{\mathrm{R}}(t)$ by the contribution of $\dot{x}(t)$ to the integral before the time t_0. Assuming that the random force $F'_{\mathrm{R}}(t)$ still obeys the fluctuation-dissipation theorem in Eq. 3.26, we in the following demonstrate that we can derive Eq. 3.4 in the main text also from Eq. 3.27.

3.8.1.2 Derivation of Eq. 3.4 from Eq. 3.27

As we investigate particles in a harmonic potential, we add a restoring force with spring constant K to Eq. 3.27, which then reads

$$\begin{aligned} m\ddot{x}(t) &= -\int_{0}^{\infty} \mathrm{d}t'\,\Gamma(t')\dot{x}(t-t') - Kx(t) + F'_{\mathrm{R}}(t) \\ &= -\int_{-\infty}^{\infty} \mathrm{d}t'\,\Gamma_+(t')\dot{x}(t-t') - Kx(t) + F'_{\mathrm{R}}(t)\,, \end{aligned} \tag{3.28}$$

with $\Gamma_+(t) = \Gamma(t)\Theta(t)$. Using the rules of Fourier transformations, which say that the time derivative in time domain corresponds to the factor $i\omega$ in frequency domain and that a convolution transforms into a product, the Fourier transform of Eq. 3.28 yields

$$\begin{aligned} -m\omega^2\tilde{x}(\omega) &= -i\omega\tilde{\Gamma}_+(\omega)\tilde{x}(\omega) - K\tilde{x}(\omega) + \tilde{F}'_{\mathrm{R}}(\omega) \\ \Leftrightarrow \qquad \tilde{x}(\omega) &= \frac{1}{i\omega\tilde{\Gamma}_+(\omega) + K - m\omega^2}\tilde{F}'_{\mathrm{R}}(\omega) = \tilde{\chi}(\omega)\tilde{F}'_{\mathrm{R}}(\omega) = \frac{\tilde{v}(\omega)}{i\omega}\,, \end{aligned} \tag{3.29}$$

where we introduced the response function $\tilde{\chi}(\omega) = 1/\left(i\omega\tilde{\Gamma}_+(\omega) + K - m\omega^2\right)$. We now make use of the assumption that Eq. 3.26 also holds for $F'_{\mathrm{R}}(t)$, hence

$$\begin{aligned}
\langle F'_{\mathrm{R}}(t)F'_{\mathrm{R}}(t')\rangle &= k_B T\,\Gamma(t-t') \\
\Leftrightarrow \quad \langle \tilde{F}'_{\mathrm{R}}(\omega)\tilde{F}'_{\mathrm{R}}(\omega')\rangle &= k_B T \int_{-\infty}^{\infty} \mathrm{d}t\, \mathrm{e}^{-i\omega t} \int_{-\infty}^{\infty} \mathrm{d}t'\, \mathrm{e}^{-i\omega' t'}\, \Gamma(t-t') \\
&= k_B T \int_{-\infty}^{\infty} \mathrm{d}t'\, \mathrm{e}^{-i(\omega'+\omega)t'} \int_{-\infty}^{\infty} \mathrm{d}t\, \mathrm{e}^{-i\omega(t-t')}\, \Gamma(t-t') \\
&= k_B T \int_{-\infty}^{\infty} \mathrm{d}t'\, \mathrm{e}^{-i(\omega'+\omega)t'} \tilde{\Gamma}(\omega) = 2\pi k_B T \delta\left(\omega+\omega'\right)\tilde{\Gamma}(\omega)\,.
\end{aligned}$$

For the velocity autocorrelation function $C^{vv}(t) = \langle v(0)v(t)\rangle$ it thus follows with Eq. 3.29

$$\begin{aligned}
\tilde{C}^{vv}(\omega) &= \int_{-\infty}^{\infty} \mathrm{d}t\, \mathrm{e}^{-i\omega t}\langle v(0)v(t)\rangle = \langle v(0)\tilde{v}(\omega)\rangle = \int_{-\infty}^{\infty} \frac{\mathrm{d}\omega'}{2\pi}\, \mathrm{e}^{-i\omega' 0}\langle \tilde{v}(\omega)\tilde{v}(\omega')\rangle \\
&= -\int_{-\infty}^{\infty} \frac{\mathrm{d}\omega'}{2\pi}\, \left\langle \omega\tilde{\chi}(\omega)\tilde{F}'_{\mathrm{R}}(\omega)\omega'\tilde{\chi}(\omega')\tilde{F}'_{\mathrm{R}}(\omega')\right\rangle \\
&= -k_B T \int_{-\infty}^{\infty} \mathrm{d}\omega'\, \omega\omega'\tilde{\chi}(\omega)\tilde{\chi}(\omega')\delta\left(\omega+\omega'\right)\tilde{\Gamma}(\omega) \\
&= k_B T\,\omega^2\,\tilde{\chi}(\omega)\tilde{\chi}(-\omega)\tilde{\Gamma}(\omega) \qquad (3.30)\\
&= k_B T\,\omega^2\,\tilde{\Gamma}(\omega)\frac{\tilde{\chi}(-\omega)-\tilde{\chi}(\omega)}{1/\tilde{\chi}(\omega) - 1/\tilde{\chi}(-\omega)} \qquad (3.31)\\
&= k_B T\omega^2\,\tilde{\Gamma}(\omega)\frac{\tilde{\chi}(-\omega)-\tilde{\chi}(\omega)}{i\omega\left(\tilde{\Gamma}_+(\omega)+\tilde{\Gamma}_+(-\omega)\right)}\,. \qquad (3.32)
\end{aligned}$$

Since the response function $\chi(t)$ is a real function, its Fourier transform obeys the relation $\tilde{\chi}(-\omega) = \tilde{\chi}^\star(\omega)$, where complex conjugated quantities are denoted with a star, therefore we get $\tilde{\chi}(-\omega) - \tilde{\chi}(\omega) = -2i\,\mathrm{Im}\left(\tilde{\chi}(\omega)\right)$. We furthermore note that for any function $f(t)$ which is symmetric in t, as for example $\Gamma(t)$, we can use

$$\begin{aligned}
\tilde{f}_+(\omega) + \tilde{f}_+(-\omega) &= \tilde{f}_+(\omega) + \tilde{f}_+^\star(\omega) = 2\,\mathrm{Re}\left(\tilde{f}_+(\omega)\right) \\
&= \int_{-\infty}^{\infty} \mathrm{d}t\, f_+(t)\,\mathrm{e}^{-i\omega t} + \int_{-\infty}^{\infty} \mathrm{d}t\, f_+(t)\,\mathrm{e}^{i\omega t} \\
&= \int_{-\infty}^{\infty} \mathrm{d}t\, f(t)\Theta(t)\,\mathrm{e}^{-i\omega t} + \int_{-\infty}^{\infty} \mathrm{d}t\, f(t)\Theta(-t)\,\mathrm{e}^{-i\omega t} = \tilde{f}(\omega)\,. \qquad (3.33)
\end{aligned}$$

Applying this identity to $\tilde{\Gamma}_+(\omega)$ in Eq. 3.32 we arrive at

$$\tilde{C}^{vv}(\omega) = 2\,\mathrm{Re}\left(\tilde{C}^{vv}_+(\omega)\right) = -2k_B T\,\omega\,\mathrm{Im}\left(\tilde{\chi}(\omega)\right)\,, \qquad (3.34)$$

which is the fluctuation-dissipation theorem in the frequency domain in terms of the velocity. We now introduce the function $\tilde{\psi}(\omega) = i\omega\tilde{\chi}(\omega)$ with the property $\mathrm{Re}\left(\tilde{\psi}(\omega)\right) = -\omega\,\mathrm{Im}\left(\tilde{\chi}(\omega)\right)$, which allows us to rewrite Eq. 3.34 as

$$\mathrm{Re}\left(\tilde{C}^{vv}_+(\omega)\right) = k_B T\,\mathrm{Re}\left(\tilde{\psi}(\omega)\right)\,. \qquad (3.35)$$

In order to obtain a relation between the full functions $\tilde{C}^{vv}_+(\omega)$ and $\tilde{\chi}(\omega)$, we employ the Kramers-Kronig relations. These tell us that for a function $\tilde{f}(\omega)$ that is analytic in the

upper complex half plane of ω and vanishes like $1/|\omega|$ or faster for $|\omega| \to \infty$ the real part and the imaginary part are connected via

$$\mathrm{Im}\left(\tilde{f}(\omega)\right) = -\frac{1}{\pi}\int_{-\infty}^{\infty} \mathrm{d}\omega' \, \frac{\mathrm{Re}\left(\tilde{f}(\omega')\right)}{\omega' - \omega}\,. \tag{3.36}$$

Thus, the real part and the imaginary part of $\tilde{f}(\omega)$ are not independent, and the full function can be reconstructed given just one of its parts. In particular, if the real parts of two analytic functions are equal, the full functions are equal. Since both $\tilde{C}_+^{vv}(\omega)$ and $\tilde{\psi}(\omega)$ converge to zero for $|\omega| \to \infty$ and per definition we know that $C_+^{vv}(t<0) = \chi(t<0) = 0$, Titchmarsh' theorem directly states that both functions fulfill the Kramers-Kronig relations. Therefore it follows from Eq. 3.34 that

$$\tilde{C}_+^{vv}(\omega) = k_B T \tilde{\psi}(\omega) = i\omega k_B T\, \tilde{\chi}(\omega) \tag{3.37}$$

and thus, after multiplication with $-i\omega\tilde{\chi}^\star(\omega)\tilde{\Gamma}(\omega)$,

$$-i\omega\tilde{C}_+^{vv}(\omega)\tilde{\chi}^\star(\omega)\tilde{\Gamma}(\omega) = \omega^2 k_B T\, \tilde{\chi}(\omega)\tilde{\chi}^\star(\omega)\tilde{\Gamma}(\omega) = \tilde{C}^{vv}(\omega)\,,$$

where we used Eq. 3.30. Inserting the definition of the response function from Eq. 3.29 yields

$$\begin{aligned}\tilde{C}_+^{vv}(\omega)\tilde{\Gamma}(\omega) = \frac{\tilde{C}^{vv}(\omega)}{-i\omega\tilde{\chi}^\star(\omega)} &= \frac{-i\omega\tilde{\Gamma}_+^\star(\omega) + K - m\omega^2}{-i\omega}\tilde{C}^{vv}(\omega) \\ &= -\left(\frac{K}{i\omega} + im\omega\right)\tilde{C}^{vv}(\omega) + \tilde{\Gamma}_+^\star(\omega)\tilde{C}^{vv}(\omega)\,.\end{aligned}$$

Using Eq. 3.33 for $\tilde{\Gamma}_+^\star(\omega) = \tilde{\Gamma}(\omega) - \tilde{\Gamma}_+(\omega)$ and rearranging terms then gives

$$-\left(\frac{K}{i\omega} + im\omega\right)\tilde{C}^{vv}(\omega) = \tilde{C}_+^{vv}(\omega)\tilde{\Gamma}(\omega) + \tilde{C}^{vv}(\omega)\tilde{\Gamma}_+(\omega) - \tilde{C}^{vv}(\omega)\tilde{\Gamma}(\omega)\,.$$

In this equation we now insert the Fourier transform of each term. The left hand side can immediately be transformed by reminding ourselves that a differentiation in the time domain corresponds to a multiplication of $i\omega$ in the frequency domain, hence

$$-\left(\frac{K}{i\omega} + im\omega\right)\tilde{C}^{vv}(\omega) = -\int_{-\infty}^{\infty}\mathrm{d}t\,\mathrm{e}^{-i\omega t}\left(KC^{vx}(t) + m\dot{C}^{vv}(t)\right)\,.$$

Also the transformation of the right hand side is straight forward, as products in the frequency domain turn into convolutions in the time domain:

$$\begin{aligned}&\tilde{C}_+^{vv}(\omega)\tilde{\Gamma}(\omega) + \tilde{C}^{vv}(\omega)\tilde{\Gamma}_+(\omega) - \tilde{C}^{vv}(\omega)\tilde{\Gamma}(\omega) \\ &= \int_{-\infty}^{\infty}\mathrm{d}t\,\mathrm{e}^{-i\omega t}\int_{-\infty}^{\infty}\mathrm{d}t'\,\left(C_+^{vv}(t-t')\Gamma(t') + C^{vv}(t-t')\Gamma_+(t') - C^{vv}(t-t')\Gamma(t')\right) \\ &= \int_{-\infty}^{\infty}\mathrm{d}t\,\mathrm{e}^{-i\omega t}\left(\int_{-\infty}^{t}\mathrm{d}t'\,C^{vv}(t-t')\Gamma(t') + \int_{0}^{\infty}\mathrm{d}t'\,C^{vv}(t-t')\Gamma(t') - \int_{-\infty}^{\infty}\mathrm{d}t'\,C^{vv}(t-t')\Gamma(t')\right) \\ &= \int_{-\infty}^{\infty}\mathrm{d}t\,\mathrm{e}^{-i\omega t}\int_{0}^{t}\mathrm{d}t'\,C^{vv}(t-t')\Gamma(t')\,.\end{aligned}$$

Combining all transforms we finally obtain

$$-\int_{-\infty}^{\infty} \mathrm{d}t\, \mathrm{e}^{-i\omega t} \left(KC^{vx}(t) + m\dot{C}^{vv}(t)\right) = \int_{-\infty}^{\infty} \mathrm{d}t\, \mathrm{e}^{-i\omega t} \int_0^t \mathrm{d}t'\, C^{vv}(t-t')\Gamma(t')\,.$$

Dropping the Fourier integrals, rearranging terms and using the symmetries of the correlation function yields Eq. 3.4 in the main text. In this calculation we have thus shown that indeed from the GLE in Eq. 3.28 together with the fluctuation-dissipation theorem it follows that Eq. 3.4 in the main text still holds.

3.8.2 Derivation of Eq. 3.14

Rewriting Eq. 3.37, it follows

$$\begin{aligned} & \tilde{C}^{vv}_{+}(\omega) = i\omega k_B T\, \tilde{\chi}(\omega) = \frac{i\omega k_B T}{\left(i\omega\tilde{\Gamma}_{+}(\omega) + K - m\omega^2\right)} \\ \Leftrightarrow \qquad & \tilde{\Gamma}_{+}(\omega) = \frac{k_B T}{\tilde{C}^{vv}_{+}(\omega)} - \frac{K - m\omega^2}{i\omega}\,. \end{aligned} \tag{3.38}$$

Using Eq. 3.33 and realizing that the second term on the right hand side is purely imaginary, we can immediately write

$$\tilde{\Gamma}(\omega) = 2\,\mathrm{Re}\left(\frac{k_B T}{\tilde{C}^{vv}_{+}(\omega)}\right)\,. \tag{3.39}$$

3.8.3 Derivation of Eq. 3.5

Integration of Eq. 3.4 yields

$$\begin{aligned} m\int_0^t \mathrm{d}t'\, \dot{C}^{vv}(t') &= -\int_0^t \mathrm{d}t' \int_0^{t'} \mathrm{d}t''\, \left[\Gamma(t'') + K\right] C^{vv}(t'-t'') \\ &= -\int_0^t \mathrm{d}t' \int_0^{t'} \mathrm{d}t''\, \left[\Gamma(t'-t'') + K\right] C^{vv}(t'') \\ &= -\int_0^t \mathrm{d}t' \int_0^{t'} \mathrm{d}t''\, \Gamma(t'-t'')C^{vv}(t'') + K\int_0^t \mathrm{d}t'\, C^{xv}(t') \\ \Leftrightarrow \qquad mC^{vv}(t) - mC^{vv}(0) &= -\int_0^t \mathrm{d}t'' \int_{t''}^t \mathrm{d}t'\, \Gamma(t'-t'')C^{vv}(t'') + KC^{xx}(t) - KC^{xx}(0) \\ &= -\int_0^t \mathrm{d}t''\, C^{vv}(t'')G(t-t'') + KC^{xx}(t) - KC^{xx}(0) \\ &= -\int_0^t \mathrm{d}t'\, G(t')C^{vv}(t-t') + KC^{xx}(t) - KC^{xx}(0)\,. \end{aligned} \tag{3.40}$$

In the upper calculation, we used the fact that $G(t=0) = C^{xv}(t=0) = 0$, since both functions are antisymmetric in t. Again we arrive at a Volterra equation of first kind, this time for the integral $G(t)$ of the memory kernel. The application of the equipartition theorem $mC^{vv}(0) = KC^{xx}(0) = k_B T$ then leads to Eq. 3.5 in the main text.

3.8.4 Mean-Squared Displacement

In the model Eq. 3.27, the mean squared displacement $\Delta x^2(t)$ of a particle can be computed by

$$\begin{aligned}\Delta x^2(t) &= \left\langle (x(t)-x(0))^2 \right\rangle = \left\langle \left(\int_0^t \mathrm{d}t'\, v(t') \right)^2 \right\rangle = \int_0^t \mathrm{d}t' \int_0^t \mathrm{d}t''\, \left\langle v(t')v(t'') \right\rangle \\ &= \int_0^t \mathrm{d}t' \int_0^t \mathrm{d}t''\, \left\langle v(0)v(t''-t') \right\rangle = \int_0^t \mathrm{d}t' \int_{-t'}^{t-t'} \mathrm{d}s\, C^{vv}(s) \\ &= \int_0^t \mathrm{d}t' \int_{-t'}^{0} \mathrm{d}s\, C^{vv}(s) + \int_0^t \mathrm{d}t' \int_0^{t-t'} \mathrm{d}s\, C^{vv}(s)\,, \end{aligned} \tag{3.41}$$

where we used the substitution $s = t'' - t'$. In order to further simplify this formula, we make use of the mathematical identity

$$\int_0^t \mathrm{d}t'\, f(t') = \int_{-u}^{t-u} \mathrm{d}t'\, f(t'+u)\,, \tag{3.42}$$

which describes how integrals change upon shifts of the integration boundaries. Applying this identity with $u = t$ on the first integral of the second term in Eq. 3.41 yields

$$\begin{aligned}\Delta x^2(t) &= -\int_0^t \mathrm{d}t' \int_0^{-t'} \mathrm{d}s\, C^{vv}(s) + \int_{-t}^0 \mathrm{d}t' \int_0^{-t'} \mathrm{d}s\, C^{vv}(s) \\ &= \int_0^t \mathrm{d}t' \int_0^{t'} \mathrm{d}s\, C^{vv}(-s) - \int_t^0 \mathrm{d}t' \int_0^{t'} \mathrm{d}s\, C^{vv}(s) \\ &= 2\int_0^t \mathrm{d}t' \int_0^{t'} \mathrm{d}s\, C^{vv}(s)\,. \end{aligned} \tag{3.43}$$

In this calculation, we twice changed the sign of the variable that we integrate over and used the symmetry $C^{vv}(-s) = C^{vv}(s)$ of the velocity autocorrelation function. Thus, in order to introduce the mean squared displacement into Eq. 3.5 in the case of a freely diffusing particle ($K = 0$) we only have to integrate it twice and multiply it with a factor 2. From Eq. 3.5, we then obtain the expression

$$2\int_0^t \mathrm{d}t' \int_0^{t'} \mathrm{d}s\, (mC^{vv}(s) - mC^{vv}(0)) = -2\int_0^t \mathrm{d}t' \int_0^{t'} \mathrm{d}s \int_0^s \mathrm{d}t''\, G(t'')C^{vv}(s-t'')\,. \tag{3.44}$$

The left hand side of this equation consists of two double integrals, which can both be computed easily,

$$2\int_0^t \mathrm{d}t' \int_0^{t'} \mathrm{d}s\, (mC^{vv}(s) - mC^{vv}(0)) = m\Delta x^2(t) - k_B T t^2\,, \tag{3.45}$$

where we used the definition of the mean squared displacement in Eq. 3.41 and the equipartition theorem $mC^{vv}(0) = k_B T$. The right hand side contains a nested triple integral, which can be transformed using another mathematical identity,

$$\int_0^t \mathrm{d}t' \int_0^{t'} \mathrm{d}t''\, f(t',t'') = \int_0^t \mathrm{d}t'' \int_{t''}^t \mathrm{d}t'\, f(t',t'')\,, \tag{3.46}$$

which expresses how the integration boundaries change if the order of integration for two nested integrals is reversed. Using this identity twice we obtain

$$\begin{aligned} m\Delta x^2(t) - k_B T t^2 &= -2\int_0^t \mathrm{d}t' \int_0^{t'} \mathrm{d}s \int_0^s \mathrm{d}t''\, G(t'')C^{vv}(s-t'') \\ &= -2\int_0^t \mathrm{d}t' \int_0^{t'} \mathrm{d}t''\, G(t'') \int_{t''}^{t'} \mathrm{d}s\, C^{vv}(s-t'') \\ &= -2\int_0^t \mathrm{d}t''\, G(t'') \int_{t''}^{t} \mathrm{d}t' \int_{t''}^{t'} \mathrm{d}s\, C^{vv}(s-t'') \\ &= -2\int_0^t \mathrm{d}t''\, G(t'') \int_0^{t-t''} \mathrm{d}t' \int_{t''}^{t'+t''} \mathrm{d}s\, C^{vv}(s-t'') \\ &= -2\int_0^t \mathrm{d}t''\, G(t'') \int_0^{t-t''} \mathrm{d}t' \int_0^{t'} \mathrm{d}s\, C^{vv}(s) \\ &= -\int_0^t \mathrm{d}t''\, G(t'')\Delta x^2(t-t'')\,, \end{aligned} \tag{3.47}$$

where the integration boundaries are shifted twice according to Eq. 3.42. This equation, which again is a Volterra equation of first kind, shows that also from the mean squared displacement the memory kernel can in principle be extracted by solving it either analytically or numerically.

3.8.5 Computing γ from Correlation Functions

The friction coefficient γ is defined as the integral over the memory kernel:

$$\gamma = \int_0^\infty \mathrm{d}t\, \Gamma(t) = \frac{1}{2}\int_{-\infty}^\infty \mathrm{d}t\, \mathrm{e}^{-i0\cdot t}\,\Gamma(t) = \frac{\tilde{\Gamma}(0)}{2}\,.$$

For unconfined particles, we can use Eq. 3.39 to compute γ:

$$\gamma = \mathrm{Re}\left(\frac{k_B T}{\tilde{C}^{vv}_+(0)}\right) = \mathrm{Re}\left(k_B T \Big/ \int_0^\infty \mathrm{d}t\, \mathrm{e}^{-i0\cdot t} C^{vv}(t)\right) = k_B T \Big/ \int_0^\infty \mathrm{d}t\, C^{vv}(t)\ . \tag{3.48}$$

For confined particles, the integral in Eq. 3.48 diverges, since the limit $\omega \to 0$ in Eq. 3.38 is not defined for a finite K. We thus employ Eq. 3.30, which we rewrite as

$$\frac{\tilde{C}^{vv}(\omega)}{\omega^2} = -\frac{\tilde{C}^{vx}(\omega)}{i\omega} = \frac{\tilde{C}^{xv}(\omega)}{i\omega} = \tilde{C}^{xx}(\omega) = k_B T \tilde{\chi}(\omega)\tilde{\chi}(-\omega)\tilde{\Gamma}(\omega)\,,$$

where we used that division by $i\omega$ in frequency domain corresponds to integration in time domain. Setting $\omega = 0$ and using the fact that $\tilde{\chi}(0) = 1/K$ we arrive at

$$\gamma = \frac{\tilde{\Gamma}(0)}{2} = \frac{K^2\tilde{C}^{xx}(0)}{2k_B T} = \frac{K^2}{2k_B T}\int_{-\infty}^\infty \mathrm{d}t\, \mathrm{e}^{-i0\cdot t}\, C^{xx}(t) = \frac{K^2}{k_B T}\int_0^\infty \mathrm{d}t\, C^{xx}(t)\,. \tag{3.49}$$

3.8.6 Discretization of Volterra Equations

The discretization of Eqs. 3.4, 3.11, 3.5 and 3.8 is straight forward. We arrive at

$$
\begin{aligned}
C_i^{vF} &= -\sum_{j=0}^{i} \Delta t\, \Gamma'_j C_{i-j}^{vv} w_{i,j}\,, \\
C_i^{FF} &= \sum_{j=0}^{i} \Delta t\, \Gamma'_j C_{i-j}^{vF} w_{i,j} + m\Gamma'_i C_0^{vv}\,, \\
mC_i^{vv} &= -\sum_{j=0}^{i} \Delta t\, G_j C_{i-j}^{vv} w_{i,j} + KC_i^{xx}\,, \\
m\Delta x_i^2 - k_B T\,(i\Delta t)^2 &= -\sum_{j=0}^{i} \Delta t\, G_j \Delta x_{i-j}^2 w_{i,j} = -\sum_{j=0}^{i-1} \Delta t\, G_j \Delta x_{i-j}^2 w_{i,j}\,,
\end{aligned}
$$

with $\Gamma'_i = \Gamma_i + K$. In each of these equations, we introduced the weighting factor $w_{i,j}$ with the values for $w_{i,i} = w_{i,0} = 1/2$ and $w_{i,j} = 1$ otherwise, which comes from the trapezoidal integration rule. Pulling out the i-th contribution from the sum in the first three equations and the $i-1$-th contribution in the last equation, respectively, and solving for Γ'_i, G_i and G_{i-1}, respectively, yields

$$
\Gamma'_i = -\frac{2}{\Delta t\, C_0^{vv}} \left[C_i^{vF} + \sum_{j=0}^{i-1} \Delta t\, \Gamma'_j C_{i-j}^{vv} w_{i,j} \right] \tag{3.50}
$$

$$
\Gamma'_i = \frac{1}{mC_0^{vv}} \left[C_i^{FF} - \sum_{j=0}^{i-1} \Delta t\, \Gamma'_j C_{i-j}^{vF} w_{i,j} \right] \tag{3.51}
$$

$$
G_i = \frac{2}{\Delta t\, C_0^{vv}} \left[KC_i^{xx} - mC_i^{vv} - \sum_{j=0}^{i-1} \Delta t\, G_j C_{i-j}^{vv} w_{i,j} \right] \tag{3.52}
$$

$$
G_{i-1} = \frac{1}{\Delta t\, \Delta x_1^2} \left[k_B T\,(i\Delta t)^2 - m\Delta x_i^2 - \sum_{j=0}^{i-2} \Delta t\, G_j \Delta x_{i-j}^2 w_{i,j} \right]\,, \tag{3.53}
$$

where we again used the symmetries of the correlation functions in the derivation. The first two equations already equal Eq. 3.12 and Eq. 3.13 in the Appendix 3.7.1. In order to derive Eq. 3.7 in the main text from Eq. 3.52 with $K \neq 0$, we employ the equipartition theorem $KC_0^{xx} = mC_0^{vv} = k_B T$ to replace the spring constant by $K = mC_0^{vv}/C_0^{xx}$. For $K = 0$ we have to discretize Eq. 3.40 instead of Eq. 3.5, which results in a replacement of the term KC_i^{xx} by mC_0^{vv}. In Eq. 3.53, we shift the index $i-1$ to i and drop the weighting factor $w_{i,j}$, since it equals 1 in every case, which then results in Eq. 3.22.

3.8.7 Determination of Plateau Value γ.

The plateau values γ are extracted via a fit of the empiric function

$$
G_{\text{fit}}(t) = \gamma \left[1 - \exp\left(-\left| t/\tau \right|^b \right) \right]
$$

to the integrals $G(t)$ in the range 0.5 ps $< t <$ 50 ps. In this fit function, the prefactor γ corresponds to the friction coefficient. The lower boundary of the fitting interval is chosen such that at this time $G(t)$ is dominated by relaxation with the longest decay time, whereas the upper boundary is determined by the noise in the plateau values. As seen in Fig. 3.12, where we present the functions $G(t)$ for methane (purple), Na^+ (yellow) and glycerol (blue) with $K = 2500$ kJ/mol nm^2, the functions $G(t)$ are perfectly described by the fits for times $t > 0.5$ ps.

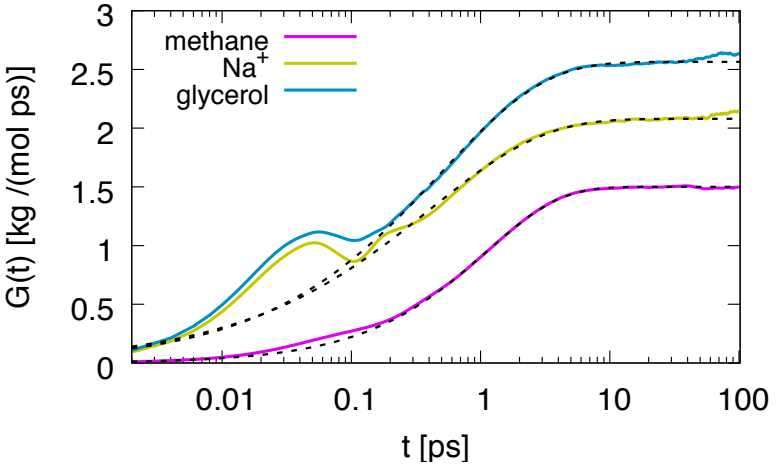

FIGURE 3.12: Fits of the function $G_{\text{fit}}(t)$ (black dashed lines) to $G(t)$ in the range 0.5 ps $< t <$ 50 ps for methane (purple), Na^+ (yellow) and glycerol (blue), which all are confined with a spring constant of $K = 2500$ kJ/mol nm^2.

3.8.8 Fitting the Long Time Decay of Memory Kernels

In order to obtain the longest decay time of the memory kernels, we fit a sum of exponentials

$$\Gamma_N^{\text{exp}}(t) = \sum_{i=1}^{N} A_i \, \mathrm{e}^{-t/\tau_i}$$

to the memory kernels. The number N of terms in the sum is increased until the longest decay time τ_N does not change any more. The method is illustrated in Fig. 3.13, where we fit the functions $\Gamma_N^{\text{exp}}(t)$ with $N = 1, \ldots, 5$ (red to green) in the range 0.6 ps $< t <$ 20 ps to the memory kernel of glycerol in a water–glycerol mixture with the viscosity $\eta = 2.26 \cdot 10^{-3}$ Ns/m^2 (purple). We observe in (a) that for $N \geq 3$ the fit functions are indistinguishable from each other. Consequently, the longest decay time remains constant with increasing N, as shown in (b). For the glycerol molecule in water–glycerol mixture we observe a monotonic dependence of the longest decay time τ_N on the solvent viscosity (see Fig. 3.7 (b) in the main text). The dependence of the parameters of the long time decay on the spring constant K however is not clear. This is illustrated in Fig. 3.14, where we see that although the long time decay is very well modeled by a sum of two exponential functions (a), neither the amplitude of the longest decay A_2 (b) nor the time constant τ_2 (c) exhibit a monotonic dependence on the spring constant. On the other hand the quantity

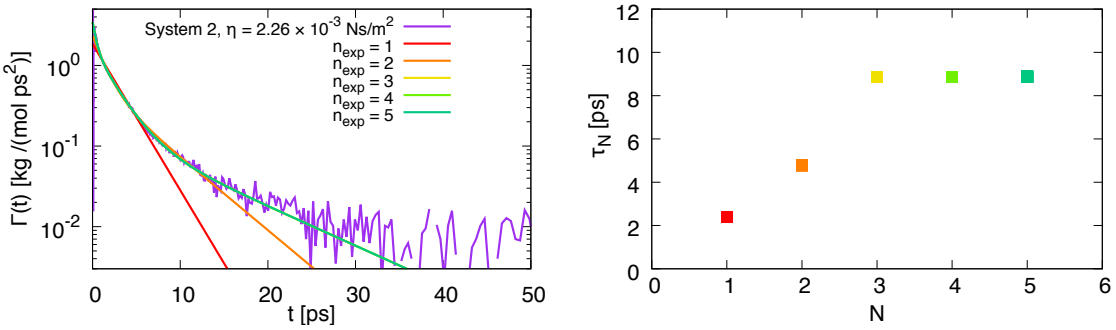

FIGURE 3.13: (a) Fits of the functions $\Gamma_N^{\mathrm{exp}}(t)$ with $N = 1, \ldots, 5$ (red to green) in the range 0.6 ps $< t <$ 20 ps to the memory kernel of glycerol in a water–glycerol mixture with the viscosity $\eta = 2.26 \cdot 10^{-3}$ Ns/m^2 (purple). (b) Longest decay time τ_N obtained from the fits in (a).

$A_1\tau_1 + A_2\tau_2$, which equals the integral over the long time decay and thus its contribution to the friction coefficient γ, increases similarly with K as the friction coefficient γ in Fig. 3.3 in the main text. Consequently, we conclude that although the parametrization Eq. 3.8.7 well describes the simulation data, it does not offer any insight into the dependence of the parameters A_i and τ_i on K.

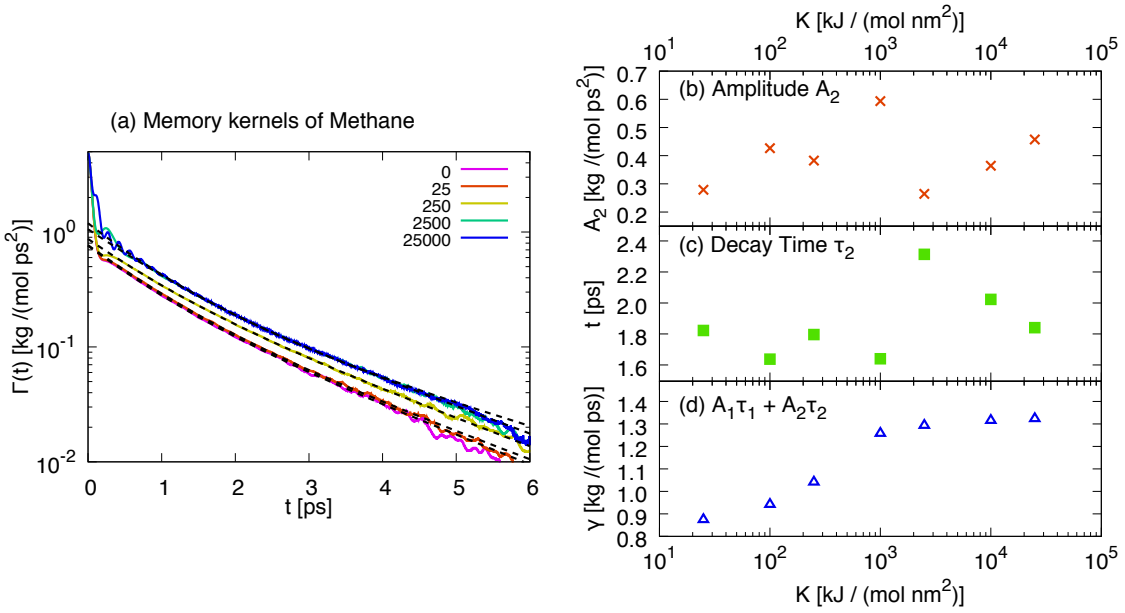

FIGURE 3.14: (a) Memory kernels Γ of methane in water in a log-lin representation for five spring constants between $K = 0$ and $K = 25000$ kJ/(mol nm^2). Black dashed lines indicate fits of a sum of two exponential functions to the long time tail with $t > 0.5$ ps. In the subfigures on the right hand side, we show the amplitude A_2 (b) and the time constant τ_2 (c) of the exponential with the slowest decay. In (d) the quantity $A_1\tau_1 + A_2\tau_2$, which equals the integral over the long time decay, is presented.

3.8.9 Radial Distribution Functions

In Fig. 3.15 we present the normalized radial distribution function

$$\rho(r)/\rho_0 = \frac{1}{4\pi\rho_0 r^2}\frac{\mathrm{d}N(r)}{\mathrm{d}r} \tag{3.54}$$

of water in the hydration shell around the solutes. In this equation ρ_0 is the bulk number density of water and $N(r)$ is the number of water molecules within the distance r around the test molecule.

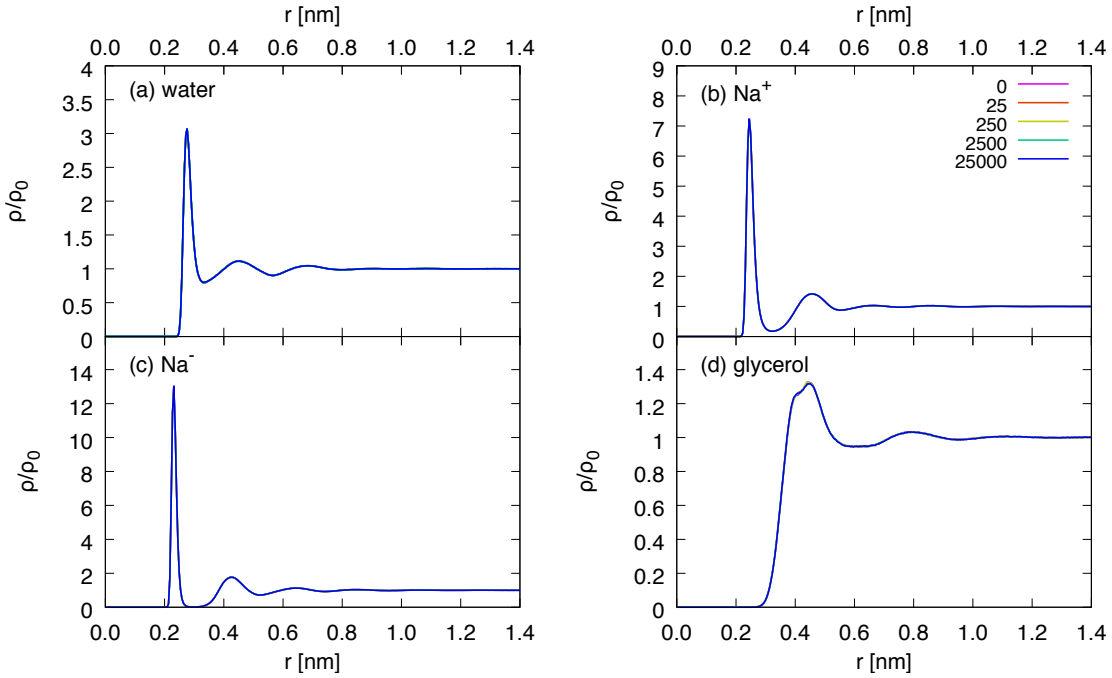

FIGURE 3.15: Radial distribution function $\rho(r)$ (Eq. 3.54) of water in the hydration shell around water (a), N^+ (b), N^- (c) and glycerol (d) for all investigated confinement strengths.

Chapter 4

Permeation of Water through a Lipid Membrane

Bibliographic information: The content of this chapter is in preparation to be submitted to a peer-reviewed journal (Ref. iii).

4.1 Introduction

Self-assembled phospholipid bilayers with embedded proteins form the outermost layer of the majority of cells [1] and serve as a barrier which keeps molecules that are crucial for the function of the cell inside the cell and toxic molecules outside. On the other hand, in order to maintain their metabolism, cells require mechanisms for the transport of molecules through the lipid bilayer, which thus has to be a selective permeable membrane. Water constitutes a special case in terms of its transport through the bilayer: Cell membranes contain aquaporin proteins, which serve as a channel for water diffusion [145]. The importance of this pathway however depends on the aquaporin concentration within the membranes, and a passive background permeation of water directly through the membrane can also contribute significantly [146]. This passive permeation of water was measured in experimental studies [6, 147–149] as well as in simulations [34, 36]. Whereas experiments can only determine the absolute value of the permeation, simulations enable us to go into more detail and examine the local resistance acting on a water molecule which diffuses through a membrane. This way, it is possible to distinguish between contributions from the free energy and the diffusivity to the permeation process, and in the simulation studies mentioned above it was found that the key factor which determines the permeation rate is the free energy barrier. The detailed understanding of the molecular mechanisms acting during the permeation is essential to link membrane and solute properties with diffusivities and free energies observed from permeation experiments on larger scales [150].

In this work, we focus on the diffusivity of the water molecule in a membrane and include memory effects in our calculations. These effects were first considered by Mori in his derivation of the generalized Langevin equation (GLE) [42], which applies to systems

where the solvent relaxation proceeds on the same time scales as the solute motion. The importance of memory effects has been proven in several fields of physics [151, 152], and they have also been considered explicitly in a study of ion diffusion through protein channels in membranes [153]. However, a detailed analysis of the memory kernels of small molecules during the permeation through bilayers has not been conducted yet. By comparing the diffusivity profiles for a water molecule in a lipid bilayer obtained from the memory kernels and the memoryless round-trip times, we show that the consideration of memory effects results in a decrease of the diffusivity by a factor of up to 20. This moves the importance of the diffusivity for the permeation process to the same level as the importance of the free energy. Fundamental consequences for drug design are expected, since memory effects are not limited to the system investigated here, but have also been observed for larger molecules [154].

4.2 Theory

We assume our system to be homogeneous perpendicular to the membrane normal, thus we can describe the permeation of molecules through the membrane as an one-dimensional problem. Let us denote the lower boundary of the membrane by the position z_1 and the upper boundary by z_2, which we place outside the membrane into the water phase. With this notation, the time-independent permeation coefficient $P(z_1, z_2)$ of molecules from z_1 to z_2 is defined by the equation

$$P(z_1, z_2) = \frac{J}{\rho(z_1) - \rho(z_2)} \,. \tag{4.1}$$

Here, $\rho(z_\mathrm{i})$ is the density of the particles at z_i, which is assumed to be constant in time, and J is the flux of the particles through the membrane. The stationary particle flux through the membrane is thus proportional to the difference in the particle density $\rho(z)$ across the membrane and the permeation coefficient is the proportionality constant between these two quantities. Since in MD simulations fluxes are generally too small to be measured directly, we transform Eq. 4.1 such that we introduce quantities that are accessible in MD simulations, which is accomplished using the Fokker–Planck equation (FPE)

$$\frac{\partial}{\partial t}\rho(z,t) = \frac{\partial}{\partial z}\left[D(z)\,\mathrm{e}^{-\beta\mathcal{F}(z)}\frac{\partial}{\partial z}\left(\mathrm{e}^{\beta\mathcal{F}(z)}\rho(z,t)\right)\right] , \tag{4.2}$$

with $\beta = k_B T$. This equation describes the time evolution of a particle density $\rho(z,t)$ in the presence of a free energy landscape $\mathcal{F}(z)$ and a diffusivity profile $D(z)$. In Appendix 4.8.1 we show that Eq. 4.1 can then be rewritten as [33, 34]

$$\frac{1}{P} = \int_{z_1}^{z_2} \mathrm{d}z\, R(z) = \int_{z_1}^{z_2} \mathrm{d}z\, \frac{\mathrm{e}^{\beta(\mathcal{F}(z)-\mathcal{F}_0)}}{D(z)} \,, \tag{4.3}$$

with the local permeation resistance $R(z) = \exp\left(\beta\mathcal{F}(z) - \beta\mathcal{F}_0\right)/D(z)$. In order to determine the permeation coefficient P of the membrane, it is thus necessary to compute both the

free energy profile $\mathcal{F}(z)$ as well as the diffusivity profile $D(z)$. In the following section, we introduce two methods that allow for the computation of the local diffusivity.

4.2.1 Round-Trip Time Method

Based on a description of the particle dynamics by FPE in Eq. 4.2, the round-trip time (RTT) method has been used to calculate diffusivity profiles of reaction coordinates of proteins [64] and water molecules at water–membrane interfaces [65]. From the one-dimensional FPE it can be deduced that the mean first passage time, which is defined as the mean time a particle needs to reach the position z_f for the first time while starting from position $z < z_f$, is given by

$$\tau_{\mathrm{FP}}(z, z_f) = \int_z^{z_f} \mathrm{d}z' \, \frac{\mathrm{e}^{\beta\mathcal{F}(z')}}{D(z')} \int_{z_{\min}}^{z'} \mathrm{d}z'' \, \mathrm{e}^{-\beta\mathcal{F}(z'')} \,. \tag{4.4}$$

In this equation, we assume a reflective boundary condition at $z_{\min} < z$, realized by $\mathcal{F}(z_{\min}) \gg \mathcal{F}(z)$, and an absorbing boundary condition at z_f. Similarly, for a reflective boundary condition at $z_{\max}$ with $z_{\max} > z > z_f$ the mean first passage time reads

$$\tau_{\mathrm{FP}}(z, z_f) = \int_{z_f}^{z} \mathrm{d}z' \, \frac{\mathrm{e}^{\beta\mathcal{F}(z')}}{D(z')} \int_{z'}^{z_{\max}} \mathrm{d}z'' \, \mathrm{e}^{-\beta\mathcal{F}(z'')} \,. \tag{4.5}$$

Combining both equations, the round-trip time

$$\begin{aligned} \tau_{\mathrm{RT}}(z, z_f) &= \mathrm{sgn}(z - z_f) \left(\tau_{\mathrm{FP}}(z, z_f) + \tau_{\mathrm{FP}}(z_f, z) \right) \\ &= Z \int_{z_f}^{z} \mathrm{d}z' \, \frac{\mathrm{e}^{\beta\mathcal{F}(z')}}{D(z')} \,, \end{aligned} \tag{4.6}$$

with $Z = \int_{z_{\min}}^{z_{\max}} \mathrm{d}z' \, \mathrm{e}^{-\beta\mathcal{F}(z')}$, is the time a particle needs to start at z, reach z_f for the first time and then return to z. From this quantity, the position-dependent diffusivity can be calculated via

$$D(z) = \frac{Z \, \mathrm{e}^{\beta\mathcal{F}(z)}}{\partial \tau_{\mathrm{RT}}(z, z_f)/\partial z} \,. \tag{4.7}$$

The FPE is based on the premise that the underlying process is markovian, which implies that the derivative of the round-trip time $\partial\tau_{\mathrm{RT}}(z, z_f)/\partial z$ and therefore also the diffusivity $D(z)$ should be independent of z_f. This requires that two conditions must be satisfied: First, $\tau_{\mathrm{RT}}(z, z_f)$ has to be larger than the time scale $\tau_m \simeq mD/k_BT$ at which the transition between inertial and diffusive motion of the particle with mass m occurs. Second, $\tau_{\mathrm{RT}}(z, z_f)$ also has to be larger than the longest time scale τ_L of the memory of the particle, which we define in the next section. Both conditions are examined in Sec. 4.5.2.

4.2.2 Autocorrelation Method

In contrast to the FPE in Eq. 4.2, which describes the time evolution of concentrations, the Langevin equation models the trajectory of a single particle in terms of a stochastic differential equation. In its generalized form, which was introduced by Mori [42], it reads

$$m\ddot{z}(t) = -\int_0^t \mathrm{d}t'\,\Gamma(t')\dot{z}(t-t') - \nabla U(z(t)) + F_\mathrm{R}(t)\,. \tag{4.8}$$

In this equation, the term $U(z(t))$ corresponds to a position-dependent potential, $\Gamma(t)$ is a memory kernel accounting for retardation effects and $F_\mathrm{R}(t)$ is the random force. The integral over the time dependent memory kernel $\int_0^\infty \mathrm{d}t\,\Gamma(t) = \gamma$ yields the friction coefficient γ, which in turn is connected to the diffusivity via the Einstein relation $D = k_B T/\gamma$. The memory kernel, and thus also the friction coefficient, are in this model assumed to be independent of the position. Furthermore, the memory kernel and the random force satisfy the fluctuation–dissipation (FT) theorem

$$\left\langle F_\mathrm{R}(t)F_\mathrm{R}(t')\right\rangle = k_B T\Gamma(t-t')\,. \tag{4.9}$$

In the limit of an infinitely stiff spring constant, $K \to \infty$, the position of the particle is restrained to the center $x = 0$ of the harmonic potential and its velocity $\dot{x}(t) = 0$ is zero. In this case the random force equals the total force $F(t) = F_R(t)$, which allows for the calculation of the memory kernel from simulations via the FT theorem, since the total force is directly accessible in a simulation. The diffusivity is then given by

$$D(z) = \frac{k_B T}{\gamma} = \frac{(k_B T)^2}{\int_0^\infty \mathrm{d}t\,\langle \Delta F(z,0)\Delta F(z,t)\rangle}\,, \tag{4.10}$$

with $\Delta F(z,t) = m\ddot{z}(t) - \nabla\mathcal{F}(z)$ in the presence of a free energy profile $\mathcal{F}(z)$. Equation 4.10 has widely been applied to compute diffusivity profiles of various molecules in membranes, for example water and other small molecules [34–36] or even fullerene [155]. With this ansatz, two difficulties emerge: First, significant long time effects can make the evaluation of the integral difficult, as then a cut-off time $t_c < \infty$ for the upper integration boundary would neglect important contributions. In this case, a theoretical model for the long time decay of the memory kernel is necessary that can be integrated analytically in order to account for the memory effects on all time scales. Second, as it was shown recently, restraining the motion of a solute particle slows down the dynamics of its hydration shell, which in turn modifies the memory kernel of the solute and increases the friction coefficient by up to 50 % in water [120], while in a more viscous environment like lipid bilayers this increase is expected to be even higher (see Chapter 3). Therefore, in this work we only apply a soft harmonic constraint with spring constants $K = 30 - 3000\ \mathrm{kJ/(mol\,nm^2)}$ on the particle (see Sec. 4.3). The method which is used for the calculation of memory kernels in such a system was introduced by Berne at al. [63] and modified for the application to particles trapped in harmonic potentials [125]. For a particle in a harmonic potential centered at position z_m with the spring constant K, the memory kernel satisfies the Volterra equation

$$m\dot{C}^{vv}(t) = -\int_0^t \mathrm{d}t'\,\Gamma(z_m,t')C^{vv}(t-t') + KC^{zz}(t)\,, \tag{4.11}$$

where $C^{vv}(t) = \langle v(t)v(0)\rangle$ and $C^{zz}(t) = \langle (z(t) - z_m)\,(z(0) - z_m)\rangle$ are the velocity and position autocorrelation functions, respectively. This equation can be derived by multiplication of the GLE in Eq. 4.8 by the initial velocity $v(0) = \dot{z}(0)$ and averaging over the random force. In literature, Eq. 4.11 [126], its first derivative [124] or its time integral (see Chapter 3) have been discretized and solved iteratively for the memory kernel, and the integrated version is used also in this work.

4.3 Simulation Setup

In this work, we perform MD simulations of fully hydrated DPPC membranes, which are simulated with the GROMACS 2016 simulation package [156]. For the DPPC membrane we use the CHARMM36UAS9 lipid force field [111, 157], where the input parameters from the NMR Lipid project [114] are converted by PyTopol in order to make this force field compatible with GROMACS. For the water model we use TIP4P 2005 [158]. All simulations are run in an NVT ensemble with a time step of 2 fs at a temperature of 323 K, which is controlled by the velocity rescaling thermostat [101] coupled with a time constant of 0.5 ps. The temperature is chosen such that it is above the melting temperature $T = 315$ K of DPPC membranes from the gel to the fluid phase [23, 103]. A snapshot of the simulation is shown in Fig. 4.1.

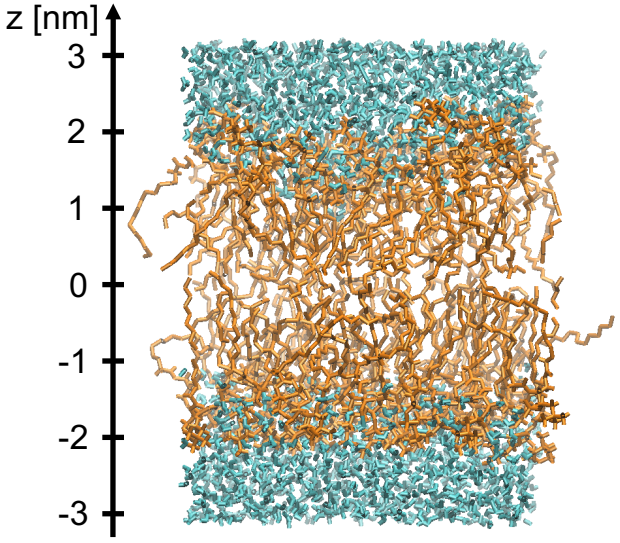

FIGURE 4.1: Simulation snapshot of the hydrated lipid bilayer.

In each simulations, one water molecule, which we do not couple to the thermostat, is confined in z-direction by a harmonic potential. The positions and the spring constants of the harmonic potential together with the simulation lengths are summarized in Table 4.1. For the RTT method, mainly the simulations with $K = 30\ \mathrm{kJ/(mol\,nm^2)}$ are used, whereas the memory kernels are computed from the simulations with the stiffer spring constants. This means that 85 % of the simulation time is spend on the calculation of memory kernels.

We write out the position, velocity and acceleration of the constrained water molecule at every time step, however only use every 20th data point for the determination of the round trip times.

Position z [nm]	0.0	0.5	1.0	1.5	2.0	2.5	3.0
K [kJ/(mol nm^2)]	simulation run time [ns]						
30	135	135	135	135	135	135	135
300	805	135	805	-	805	-	805
3000	805	-	805	-	805	-	805

TABLE 4.1: Simulation lengths in ns for each harmonic potential centered at position z with spring constant K.

4.4 Results for the Free Energy

The free energy landscape of small molecules within a lipid bilayer is well-studied in literature and numerous methods exist for its calculation [159]. Here, the free energy landscape of the lipid bilayer is determined using the Weighted Histogram Analysis Method (WHAM) [160] algorithm, which computes the free energy from the biased simulations with the parameters presented in Table 4.1. The histograms of the particle position within each biased simulation are presented in Fig. 4.2 (a), and the free energy profile calculated from the histograms is shown in Fig. 4.2 (b) in red together with the density profiles of water (blue) and the DPPC membrane (green). We observe that the lipid bilayer forms a large free energy barrier, with a small contribution of 7 kJ/mol from the headgroup region, which is indicated by an orange background, and a large contribution of 25 kJ/mol from the lipid tail region. The total height is approximately $\Delta\mathcal{F} = 32$ kJ/mol and thus a bit higher than the barrier heights $\Delta\mathcal{F} = 23 - 25$ kJ/mol measured in earlier simulation studies [34, 36], which can be explained by the use of a different force field. The free energy profile computed from the water density via $\mathcal{F}(z) = -k_\mathrm{B}T \ln(\rho(z)/\rho(z_\mathrm{w}))$ (black dashed line), with $z_\mathrm{w} = 3.3$ nm in the water phase, conforms with the WHAM profile in the water and the headgroup region, but exhibits a higher maximum in the center. This deviation can be explained by the very low statistics in the water density inside the membrane. Experimentally, the free energy of water inside a membrane cannot be measured, instead the free energy of water in hexadecane is chosen in literature for a comparison [34, 36], which has a value of $24 - 25$ kJ/mol determined from the water solubility at 40 °C [161, 162]. However, this comparison neglects possible long-range contributions from the polar headgroups of the bilayers, hence it has to be taken with care.

This barrier, which is due to the strong hydrophobicity of the hydrocarbon chains in the membrane center, causes a strong repulsion of water away from the membrane center, which can also be observed in the histograms: The maximum of the histogram, which is obtained from the simulation with the umbrella potential centered at $z = 0.5$ nm and $K = 30$ kJ/mol nm^2, is shifted to the position $z = 1.2$ nm. In order to have a sufficient sampling

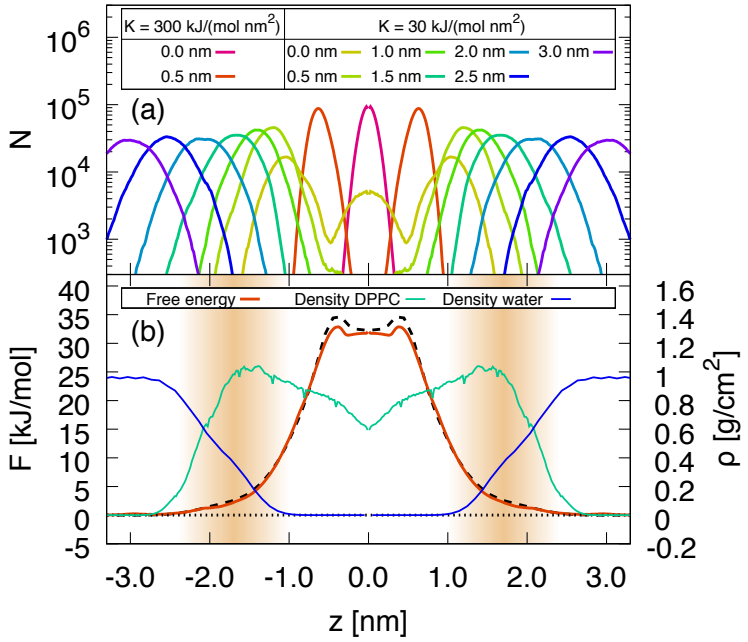

FIGURE 4.2: (a) Histograms of the particle positions in each biased simulation. The positions of the minimum of each umbrella potential are given in the key of the figure. (b) Density profiles $\rho(z)$ of water (blue) and DPPC (green) and free energy profile (red) of a water molecule in the DPPC membrane. The free energy profile is calculated by the WHAM algorithm using the data in (a) as input. A free energy profile computed via $\mathcal{F}(z) = -k_B T \ln(\rho(z)/\rho(z_w))$, with $z_w = 3.3$ nm in the water phase, is included as a black dashed line, however is based on poor statistics in the membrane center. The headgroup region is indicated by an orange background. Note that in both figures only data for the positive z-axis is simulated, which is mirrored at the symmetry point $z = 0$ to obtain the data for the negative z-axis.

in the membrane center, it is therefore important to constrain the water molecule there with a stiffer potential. We therefore also used the simulations with $K = 300\ \mathrm{kJ/mol\,nm^2}$ at the positions $z = 0$ and $z = 0.5$ nm for the calculation of the round-trip times.

4.5 Results for the Diffusivity

4.5.1 Lateral Diffusivity

In lateral direction (which in the following is denoted by the variable x) along the membrane, the free energy $\mathcal{F}_L$ and diffusivity D_L are spatially constant, hence the FPE in Eq. 4.2 simplifies to $\frac{\partial}{\partial t}\rho(x,t) = D_L \frac{\partial^2}{\partial x^2}\rho(x,t)$, which is for the initial condition $\rho(x,0) = \delta(x - x_0)$ solved by the Gaussian distribution

$$\rho(x,t) = \frac{1}{\sqrt{2\pi D_L t}} \exp\left((x - x_0)^2 / 2 D_L t\right) .$$

The width of the concentration distribution is therefore determined by the mean–squared displacement (MSD) $\left\langle (x(t) - x_0)^2 \right\rangle = \left\langle \Delta x^2(t) \right\rangle = 2D_{\mathrm{L}}t$. For processes that are non-markovian and thus not satisfy the FPE, this relation is generalized to $\left\langle \Delta x^2(t) \right\rangle \sim t^{\alpha}$, which includes the markovian case for $\alpha = 1$. The lateral MSD of the water molecule is presented in Fig. 4.3 (a) for four different positions z in the membrane, with the corresponding exponent $\alpha(t) = \mathrm{d}\ln\left\langle \Delta x^2(t) \right\rangle / \mathrm{d}\ln t$ as a function of t in Fig. 4.3 (b). Inertial motion of the particle, which is characterized by an exponent $\alpha = 2$, is observed at all positions for times $t < 0.03$ ps, in the membrane center even for $t < 0.1$ ps. The reason for the prolonged inertial dynamics in the membrane center is the low density of lipid chains at this location, which is connected to a high concentration of free volume, which is defined as the volume outside the van-der-Waals radius of any particle [34]. For times larger than 0.1 ps (headgroup region) to 0.6 ps (membrane center) the dynamics of the water molecule becomes subdiffusive, i.e. the exponent $\alpha(t)$ is smaller than unity. Within this intermediate regime, all functions $\alpha(t)$ exhibit one minimum between 0.5 ps and 3 ps and in the following increase asymptotically towards unity, which is the diffusive limit. This convergence is illustrated in the inset of Fig. 4.3 (b), where we display the quantity $1 - \alpha(t)$ in a log-log representation: In the water phase ($z = 3$ nm) this quantity is practically zero within the noise for times $t > 50$ ps, whereas at the inside of the headgroups ($z = 1$ nm) it only decays to 0.2 for $t = 300$ ps. Nevertheless, we observe that the functions $1 - \alpha(t)$ exhibit a power law behavior for all positions, which then for the MSD in the long time limit yields the functional form

$$\left\langle \Delta x^2(t) \right\rangle = 2D_{\mathrm{L}}t \exp\left[\frac{1}{b} \left(\frac{\tau}{t} \right)^b \right], \tag{4.12}$$

where τ is a time constant and b is the exponent defined by $1 - \alpha(t) \sim (t/\tau)^{-b}$ (see Appendix 4.8.2 for derivation). This function we fit with the quantities D_{L}, τ and b as parameters to the MSD in Fig. 4.3 (a). The resulting fits are indicated in Fig. 4.3 (a) as dashed lines and show perfect agreement with the data for $t > 1$ ps. The resulting parameters D_{L}, τ and b are presented in Table 4.2.

In a next step, we compute the memory kernels $\Gamma_{\mathrm{L}}(t)$ and their integrals $G_{\mathrm{L}}(t) = \int_0^t \mathrm{d}t' \, \Gamma_{\mathrm{L}}(t')$ by applying equation Eq. 4.11 to the trajectories of the water molecule. As in lateral direction no confining potential is used, we use $K = 0$ in Eq. 4.11. The results are presented in Fig. 4.4 and it can be seen that the short time behavior of the memory kernels is very similar for all positions except for $z = 0$, where the memory kernel exhibits a much smaller amplitude due to the low lipid density and thus reduced interactions in this region. Differences can be however seen in the long time behavior of the memory kernels, which can in more detail be studied in the log-log representation in the inset of Fig. 4.4 (a). The memory kernel at $z = 3.0$ nm decays the fastest and is not distinguishable from zero for times $t > 10$ ps. This is the time scale where the dynamics can be assumed to be markovian, which is in very good agreement with literature [163] and the finding that the exponent α of the MSD is close to unity at this time. For the memory kernel at $z = 1.0$ nm we obtain the slowest long time decay, also in agreement with the smallest $\alpha(t)$ for this position.

The integrals $\Gamma_{\mathrm{L}}(t)$ over the memory kernels are presented in Fig. 4.4 (b). As discussed in Sec. 4.2.2, in the limit $t \to \infty$ this integral yields the friction coefficient γ_{L}. In order to

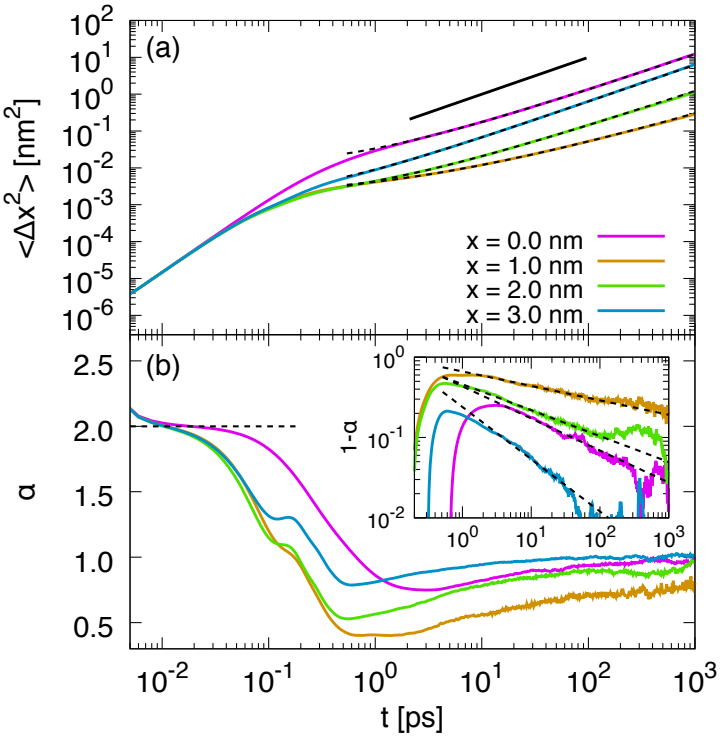

FIGURE 4.3: (a) Mean-squared displacement of water within a DPPC membrane in lateral direction at four different z-positions. The dashed lines indicate fits of the functions Eq. 4.12 to the data, whereas the black solid line represents a purely diffusive behaviour $\langle \Delta x^2 \rangle \sim t$ and serves as guide to the eye. (b) Exponent $\alpha(t) = \mathrm{d} \ln \langle \Delta x^2 \rangle / \mathrm{d} \ln t$ of the MSD as a function of time. The exponent $\alpha = 2$ of inertial dynamics $\alpha = 2$ is included as a dashed line. Inset: $1 - \alpha(t)$ as a function of time t in a log-log representation. Dashed lines indicate the expressions $(t/\tau)^{-b}$, where the parameters τ and b are obtained from the fits in (a).

estimate the value of the diffusion coefficient $D_\mathrm{L} = k_B T / \gamma_\mathrm{L}$, we fit the function

$$G_\mathrm{fit}(t) = \frac{k_B T}{D_\mathrm{L}} \exp\left[-\frac{1}{b} \left(\frac{\tau}{t} \right)^b \right] \tag{4.13}$$

to the $\Gamma_\mathrm{L}(t)$ for times $t > 2$ ps. The choice of this fit function is based on the argument that the time derivative of the MSD and $1/\Gamma_\mathrm{L}(t)$ have the same long time behavior (See Appendix 4.8.3 for more details). The resulting fits, which are in good agreement with the functions $G_\mathrm{L}(t)$ for $t > 2$ ps, are indicated by dashed lines in Fig. 4.4 (b). Also the derivatives of the functions in Eq. 4.13 match the long time tails of the memory kernels, as seen in the inset of Fig. 4.4 (a), hence we conclude that this fit function is suitable to extract the diffusion coefficient from the memory kernels.

The values of the parameters D_L, τ and b obtained from the fits of $G_\mathrm{fit}(t)$ to $G_\mathrm{L}(t)$, which are presented in Table 4.2, are all larger than the corresponding values from the MSD. For the diffusion coefficient, the deviations are about 2–10%, which is within the errors of the values. In the membrane center the lateral diffusivity of the water molecule is highest and approximately two times higher than in the water phase. Again, this can be explained by the low mass density in the membrane center. At the interface between the headgroups

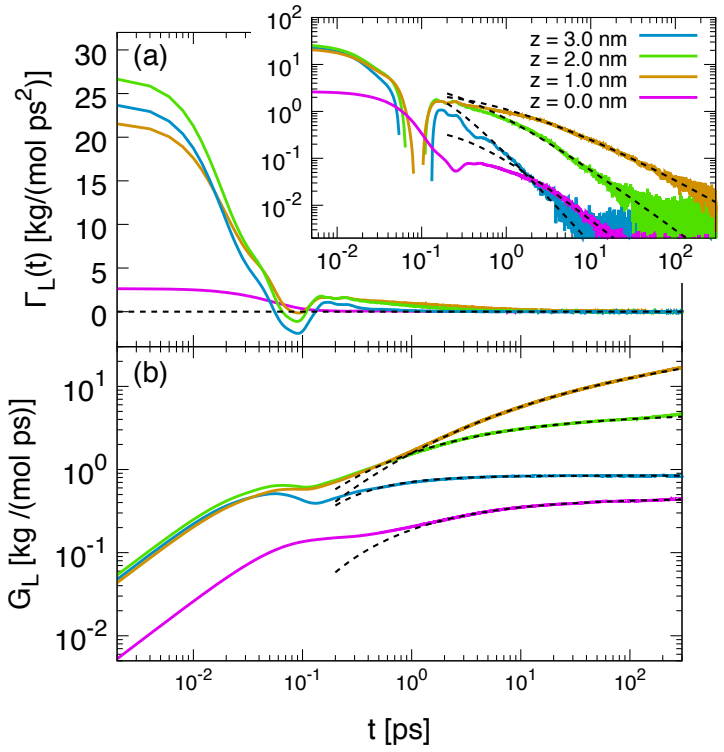

FIGURE 4.4: (a) Memory kernels $\Gamma_{\mathrm{L}}(t)$ corresponding to the MSD in Fig. 4.3 (a) in a lin-log representation. Inset: The same data in a log-log representation. (b) Running integrals $G_{\mathrm{L}}(t)$ over the memory kernels. Dashed lines indicate fits of the function in Eq. 4.13 to the long time behavior of $G_{\mathrm{L}}(t)$, and the derivatives of the resulting fit functions are also shown in the inset of (a) as dashed lines. The results for the diffusion coefficient are summarized in Table 4.2.

and the water phase the lateral diffusivity is approximately ten times lower than in the water phase, which is also the result of earlier studies [164]. A more detailed discussion of the diffusivity is found in Sec. 4.6. For τ and b, the deviations are partly larger than the errors, however the values of these parameters always exhibit the same dependence on the position z for both fits, as for example both fits yield the smallest exponent b at the position $z = 1$ nm and the largest at $z = 3$ nm. An explanation for the deviations between the MSD and $G_{\mathrm{L}}(t)$ in their values of τ and b is that these two parameters are presumably fitted such that they describe not only the long time behavior, but also parts of the intermediate time dependence of the MSD and $G_{\mathrm{L}}(t)$, respectively, which for both functions is different.

4.5.2 Transversal Diffusivity

In contrast to the lateral motion, it is not possible to directly compute the diffusivity from the MSD in the transversal direction because of the existence of a position-dependent free energy $\mathcal{F}(z)$ which has to be considered. This can be done by either using the full FPE in Eq. 4.2 or the GLE in Eq. 4.8 to describe the particle dynamics. In case that also the diffusivity $D_{\mathrm{T}}(z)$ is position dependent, the description by the GLE also requires that the particle motion is constrained to a region of constant diffusivity, which is most conveniently realized by a harmonic potential. In this section, we apply both descriptions, as we

Position [nm]	0.0	1.0	2.0	3.0
	D_L [nm^2/ns]			
from MSD	5.70 ± 0.16	0.0522 ± 0.0042	0.527 ± 0.029	3.121 ± 0.043
from $G_L(t)$	5.91 ± 0.14	0.0589 ± 0.0058	0.551 ± 0.027	3.177 ± 0.031
	τ [ps]			
from MSD	0.123 ± 0.020	0.102 ± 0.014	0.090 ± 0.025	0.111 ± 0.051
from $G_L(t)$	0.235 ± 0.027	0.184 ± 0.031	0.126 ± 0.053	0.159 ± 0.021
	exponent b			
from MSD	0.399 ± 0.020	0.180 ± 0.005	0.322 ± 0.021	0.650 ± 0.080
from $G_L(t)$	0.528 ± 0.027	0.209 ± 0.010	0.392 ± 0.036	0.964 ± 0.072

TABLE 4.2: Parameters D_L, τ and b obtained from fits of Eq. 4.12 to the MSD (first line) and from fits of Eq. 4.13 to $G_L(t)$ (second line).

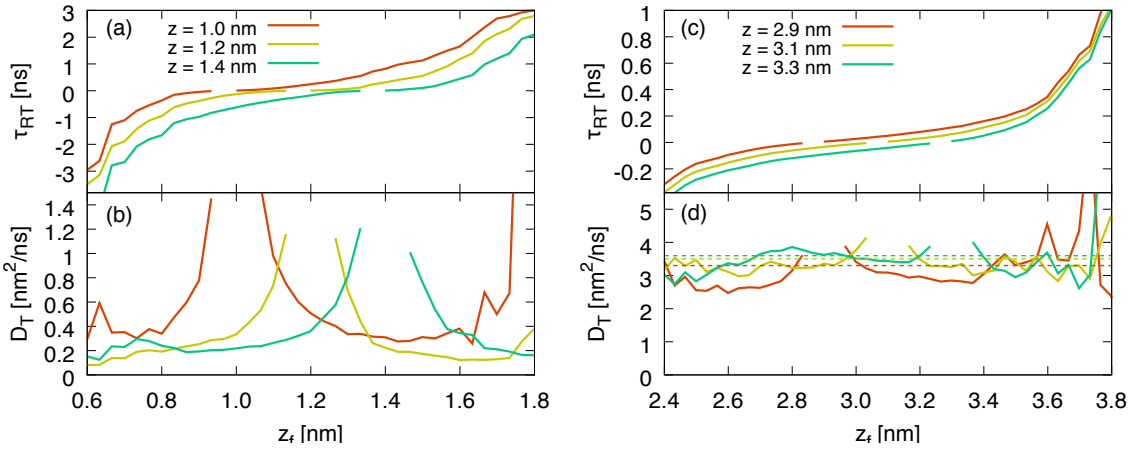

FIGURE 4.5: Return times τ_{RT} for a water molecule to go from position z to z_f and return to z (subfigures (a) and (c)) and corresponding diffusivities D_T (subfigures (b) and (d)). In (a) and (b) the the umbrella potential is centered at the position $z = 0.5$ nm, whereas in (c) and (d) the minimum is at $z = 3.0$ nm. In all figures, the quantities are shown for three starting positions z as a function of the return point z_f. The spring constant of both umbrella potentials is $K = 30$ kJ/(mol nm^2). In (d), we included the results from [164] for the the three positions as dashed lines.

compute a transversal diffusivity profile $D_{\mathrm{T}}(z)$ via the RTT method, which is based on the FPE, and additionally compute diffusivities from memory kernels based on the GLE.

In Fig. 4.5 (a) and (c) we present the round-trip times $\tau_{\mathrm{RT}}(z, z_f)$ in two umbrella windows centered at the positions $z = 0.5$ nm, which is in lipid the tail region of the membrane, and $z = 3.0$ nm, which is in the water phase. For each umbrella window the round-trip times for three positions z are displayed as a function of the return point z_f. The corresponding diffusivities $D_{\mathrm{T}}(z, z_f)$ are shown in Fig. 4.5 (b) and (d), again as a function of z_f. In the water phase (Fig. 4.5 (d)) we observe that for each position z the $D_{\mathrm{T}}(z, z_f)$ is independent of z_f, apart from statistical noise, if the separation $\Delta z = |z - z_f|$ between the position z and the return point z_f is in the range $0.1 \text{ nm} < \Delta z < 0.4$ nm. There, the dynamics of the water molecule is satisfactorily described by the memoryless FPE, and the diffusion coefficient $D_{\mathrm{T}}(z)$ is obtained by taking the mean $\langle D_{\mathrm{T}}(z, z_f) \rangle_{z_f}$ over z_f in this range. The results are in very good agreement with earlier studies, where $D_{\mathrm{T}}(z) = 3.4 \text{ nm}^2/\text{ns}$ was measured at a distance of $z = 3.0$ nm from the membrane center. For smaller separations Δz the diffusivity is slightly larger, which can be explained by inertial effects which occur at small time and length scales, whereas for separations $\Delta z > 0.4$ nm the statistical noise becomes dominant.

The picture changes in the interior of the lipid membrane (Fig. 4.5 (b)), where the diffusivity $D(z, z_f)$ decreases steadily as a function of z_f up to separations $\Delta z > 0.4$ nm. Here, non-markovian memory effects play a significant role for a much longer time than in the water phase. In order to quantify these memory effects, we compute the memory kernels $\Gamma_{\mathrm{T}}(t)$ of the water molecule in the water phase as well as in the membrane interior via Eq. 4.11 from the correlation functions $C^{vv}(t) = \langle v(t)v(0) \rangle$ and $C^{zz}(t) = \langle (z(t) - z_m)\,(z(0) - z_m) \rangle$ (see Fig. 4.6 for results). In order to keep the water dynamic within a region of constant diffusivity, we constrain the water molecules in a harmonic potential with the spring constants $K = 300 \text{ kJ}/(\text{mol nm}^2)$ and $K = 3000 \text{ kJ}/(\text{mol nm}^2)$). The reason for this choice of the spring constants is that for a modeling of the water dynamics with Eq. 4.8, the sum of the applied harmonic potential and free energy profile shown in Fig. 4.2 must in good approximation be quadratic. For positions outside the membrane center the free energy profile is very smooth and only lead to a shift of the harmonic potential in z-direction, which creates a constant offset in the correlation functions of $C^{zz}(t)$ seen in Fig. 4.6 (b). Here, a simple subtraction of this plateau value from the correlation function is sufficient to correct for the influence of the free energy on the applied potential. Contrary to that, in the central region of the membrane, the free energy profile forms two small maxima at $z = \pm 0.5$ nm. In order to keep the quadratic approximation valid, the potential has to be chosen such that the dynamics of the water molecule is not influenced by these maxima. Using spring constants smaller than $K = 300 \text{ kJ}/(\text{mol nm}^2)$ in the membrane center, the water molecules would enter or even cross the barrier, which would lead to pronounced long time tails in the position autocorrelation function and thus also in the memory kernel.

At first sight, the resulting memory kernels $\Gamma_{\mathrm{T}}(t)$ and the integrals $G_{\mathrm{T}}(t)$ of the transversal dynamics, which are displayed in Fig. 4.7, very much resemble their counterparts $\Gamma_{\mathrm{L}}(t)$ and the integrals $G_{\mathrm{L}}(t)$ of the lateral dynamics (Fig. 4.4). For times $t < 300$ ps only the memory kernel of the water molecule in the water bulk at $z = 3$ nm exhibits a plateau in

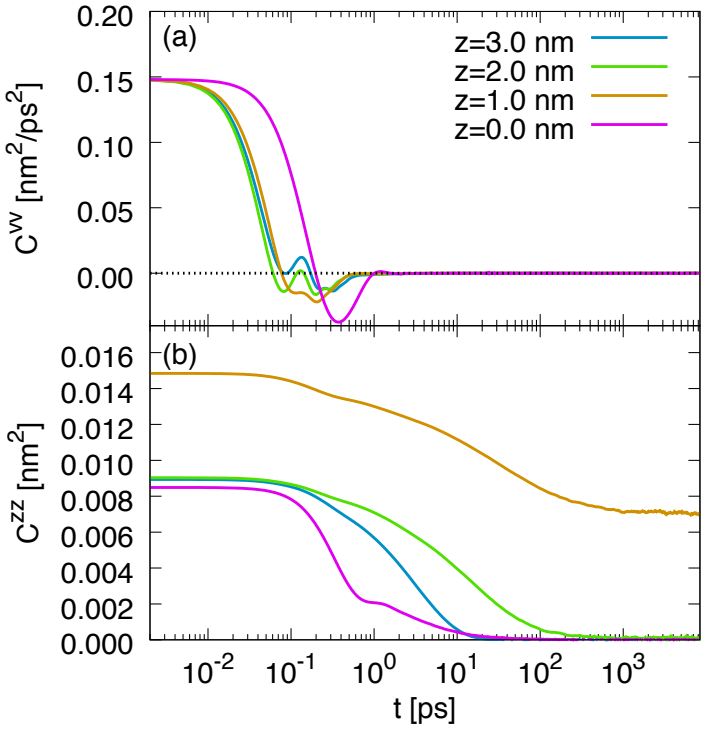

FIGURE 4.6: Autocorrelation functions $C^{vv}(t)$ (a) and $C^{zz}(t)$ (b) of the transversal particle dynamics as a function of time t for a water molecule constrained by a potential with spring constant $K = 300\,\mathrm{kJ/(mol\,nm^2)}$.

$G_\mathrm{T}(t)$, whereas for all other positions the memory kernels have not decayed to zero. This signalizes that inside the membrane memory is important for the particle dynamics up to the nanosecond scale, thus, as already seen in Fig. 4.5, the Fokker–Planck formalism is not suitable for modeling the particle trajectories there. Another important consequence is that the extraction of diffusion coefficients from MD simulations requires trajectories with a minimal length of several nanoseconds in order to resolve the long time behaviour of the particle dynamics.

The determination of the D_T from the memory kernels is again accomplished by a fit of the functions in Eq. 4.13 to the long time decay, with the results summarized in Table 4.3. We repeat this analysis for simulations with a spring constant $K = 3000\,\mathrm{kJ/(mol\,nm^2)}$ in order to obtain an estimate for the confinement-dependent effect which decreases the diffusivity of particles [120]. We observe that indeed this effect can be measured for the positions $z = 2.0$ nm and $z = 3.0$ nm, but it has the same order of magnitude as the error on D_T. For $z = 1.0$ nm, the effect is even reversed, i.e. we obtain a larger diffusivity for the stiffer spring constant, however in this case the error on D_T exceeds it. We thus conclude that the confinement-dependence of the diffusivity will not significantly change our results.

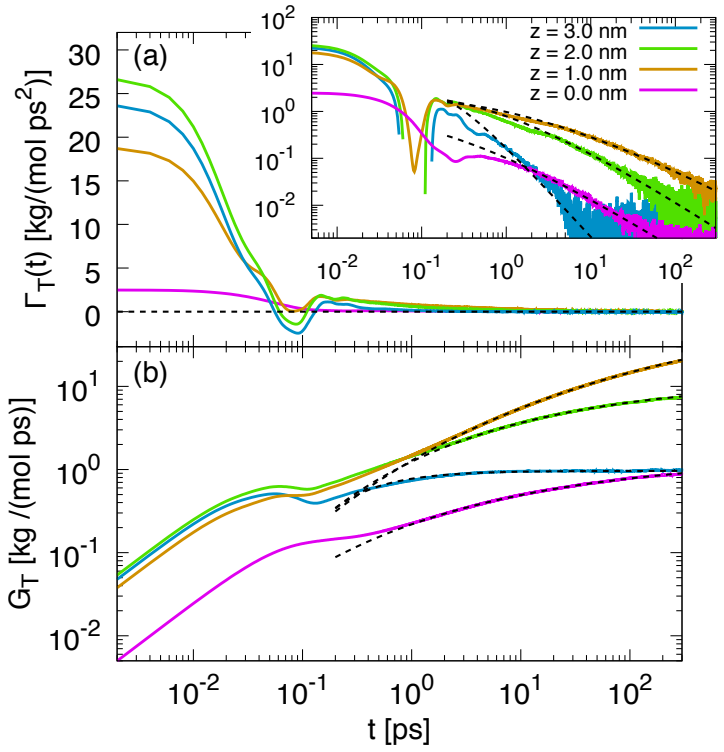

FIGURE 4.7: (a) Memory kernels $\Gamma_{\mathrm{T}}(t)$ computed from the autocorrelation functions $C^{vv}(t)$ and $C^{zz}(t)$ of the transversal particle dynamics using Eq. 4.11 in a lin-log representation. Inset: The same data in a log-log representation. (b) Running integrals $G_{\mathrm{L}}(t)$ over the memory kernels. Dashed lines indicate fits of the function in Eq. 4.13 to $G_{\mathrm{L}}(t)$ for $t > 2$ ps, and the derivatives of the resulting fit functions are also shown in the inset of (a) as dashed lines. The results for the diffusion coefficient are summarized in Table 4.3.

4.6 Discussion

All data for the diffusivity is summarized in the profile in Fig. 4.8 (a). The profile from the RTT method is determined by taking the mean $D_{\mathrm{T}}(z) = \left\langle D_{\mathrm{T}}(z, z_f) \right\rangle_{z_f}$ with respect to z_f in the range 0.1 nm $< \Delta z <$ 0.4 nm. This profile exhibits a value of $D_{\mathrm{T}}^{\mathrm{RTT}} \approx 3$ nm^2/ps in the pure water phase, which decreases towards the headgroup region. At the interface between the water phase and the headgroups, a value of $D_{\mathrm{T}}^{\mathrm{RTT}} \approx 0.75$ nm^2/ps is obtained. From this point up to a distance of 0.5 nm from the center, the diffusivity remains small with values between 0.3 and 0.8 nm^2/ps. At $z = \pm 0.5$ nm a sharp increase of the diffusivity towards the center is observed, where the diffusivity profile forms a maximum with $D_{\mathrm{T}}^{\mathrm{RTT}} \approx 3$ nm^2/ps, which is similar to the value in the water phase. This profile is qualitatively in between the results of [34], where the diffusivity in the membrane center is much larger than in bulk water, and [36], where only a small maximum in the membrane center is observed. Best agreement between the present work and the literature is obtained in the central headgroup region, where all studies yield $D_{\mathrm{T}} \approx 0.5 - 1$ nm^2/ps. A possible source for the observed deviations is, besides the higher temperature of $K = 350$ K in [34] and in general differences in the force fields, the method used for the calculation of the diffusivity: Both in [34] and [36] the diffusivity was computed via Eq. 4.10, but while in [34] it is not specified how the integral was evaluated, in [36] a double exponential function was

Position [nm]	0.0	1.0	2.0	3.0
K [kJ/(mol nm^2)]	D_T [nm^2/ns]			
300	1.88 ± 0.38	0.0227 ± 0.0075	0.223 ± 0.029	2.789 ± 0.059
3000	1.77 ± 0.21	0.0266 ± 0.0022	0.171 ± 0.016	2.671 ± 0.025
	τ [ps]			
300	0.043 ± 0.042	0.198 ± 0.091	0.192 ± 0.076	0.203 ± 0.022
	exponent b			
300	0.246 ± 0.041	0.168 ± 0.018	0.278 ± 0.028	0.972 ± 0.079

TABLE 4.3: Transversal diffusivity D_T obtained from fits of Eq. 4.13 to $G_T(t)$ for two spring constants $K = 300$ kJ/(mol nm^2) and $K = 3000$ kJ/(mol nm^2). For the first spring constant, we also present the parameters τ and b.

fitted to the force-autocorrelation function and then integrated analytically, however the fitting range is not published.

The consideration of memory effects by extrapolating the fit function in Eq. 4.13 to $t \to \infty$ results in the data denoted by green squares for the lateral motion and purple triangles for the transversal motion. We observe that in the water phase the value of D_L in lateral direction is consistent with the profile D_T^{RTT}, whereas the D_T of the transversal dynamics yields values which are 7 % smaller. This we assign to the confinement-dependent friction effect instead of an anisotropy of the water dynamics, since the former has been shown to be exactly of this magnitude for spring constants of $K = 300$ kJ/(mol nm^2) (see Chapter 3). The lateral diffusivity at $z = 2$ nm, which is the position of the interface between the water phase and the headgroups, is $D_L = 0.53$ nm^2/ps, hence not far from the value of D_T^{RTT}, whereas in contrast to this, the value D_T^{mem} from the memory kernels suggests that the transversal diffusivity rather is 0.2 nm^2/ps at this position. Since we have seen that the RTT method neglects important memory effects, we conclude that indeed D_T is smaller than D_L by a factor of more than two, which means that the water dynamics is highly anisotropic in the headgroup region. Going further inwards, the discrepancy between D_T^{mem} and D_T^{RTT} even increases to a factor of twenty, as we measure $D_L \approx 0.055$ nm^2/ps and $D_T^{mem} \approx 0.025$ nm^2/ps, with their ratio remaining at a value of 2.5. The discrepancy between the diffusion coefficients D_T^{RTT} and D_T^{mem} can be seen best in the log-lin representation in Fig. 4.8 (b). At the inside of the head groups, memory effects are most pronounced, therefore the discrepancy does not come as a surprise. The jump of the diffusivity at the membrane center is reproduced by all three methods. The lateral diffusivity is highest with a value of $D_L \approx 6$ nm^2/ps, which is twice as high as in the water phase, and for the transversal direction it is $D_T^{mem} \approx 1.88$ nm^2/ps, thus only off by a factor of 1.6 from D_T^{RTT}.

The similarity of the transversal diffusivities computed by the two methods indicates that memory effects are less important here than in the headgroup region, which has already been deduced from the memory kernels in Figs. 4.4 and 4.7. Still, our results imply that also in the membrane center the diffusion is anisotropic.

The anisotropy of the water dynamics inside the membrane can be caused by either a structural or dynamical anisotropy of the lipid chains. As discussed in [34], free volume pockets exist in the lipid bilayer, in which the small solutes can move in a more inertial fashion. The effect of the free volume has already been seen in the prolonged inertial dynamics in the lateral direction at $z = 0$ nm (see Sec. 4.5.1), which translates into a low memory kernel $\Gamma(t)$ at short times and manifests in the high diffusivity in this region. If such pockets aligned preferably in lateral direction, corresponding to a structural anisotropy of the membrane, this would result in an increased lateral mobility of solutes. However, no striking difference in the short time behavior is observed between memory kernels $\Gamma_{\mathrm{L}}(t)$ in lateral direction (Fig. 4.4) and $\Gamma_{\mathrm{T}}(t)$ in transversal direction (Fig. 4.7). For $z = 1$ nm, the memory kernel $\Gamma_{\mathrm{T}}(t)$ at times $t < 0.01$ ps is even smaller than $\Gamma_{\mathrm{L}}(t)$, suggesting that such pockets rather align in transversal direction. Indeed, such a preferred alignment along the membrane normal was found in earlier studies of the membrane structure [165]. We thus address the anisotropic diffusion to an anisotropic dynamical viscosity of the membrane, originating in longer relaxation times of the lipid tails in transversal direction compared to the lateral direction, which are also reflected in the longer decay times τ and smaller exponents b of the memory kernels in transversal direction.

Using the profile $D_{\mathrm{T}}^{\mathrm{RTT}}(z)$ for the diffusivity and the free energy profile from Fig. 4.8 (b), we compute the local resistance $R(z) = \exp\left(\beta\left(\mathcal{F}(z) - \mathcal{F}_0\right)\right)/D(z)$. We observe that the resistance is maximal at a distance of 0.5 nm from the membrane center, which approximately is at the same position as the maximum of the free energy. This finding, which confirms the results of earlier studies of this system [34, 36], indicates that the permeation process across the membrane is mainly determined by the barrier in the free energy profile $\mathcal{F}(z)$. This is illustrated by the black dashed line, which corresponds to a hypothetical resistance $R_{\mathrm{hyp}}(z)$ assuming a flat diffusivity of $D = 2.8$ nm^2/ns. We observe that $R(z)$ to a large degree follows the shape of $R_{\mathrm{hyp}}(z)$, which can be explained by the fact that $D_{\mathrm{T}}^{\mathrm{RTT}}(z)$ exhibits a variation of less than one order of magnitude throughout the entire membrane, whereas the factor $\exp\left(\beta\mathcal{F}(z)\right)$ increases by 6 orders from outside to inside. The picture changes when we look at the resistance computed from the $D_{\mathrm{T}}^{\mathrm{mem}}$; This quantity varies about two orders of magnitude within a distance of 1 nm from the membrane center, in which the factor $\exp\left(\beta\mathcal{F}(z)\right)$ exhibits changes of similar size. Although we have not calculated the memory kernels at the maximum at $z = 0.5$ nm due to the uneven free energy profile (this would require a very stiff potential to keep the sum of both terms harmonic, which would then again induce strong confinement-dependent effects), we are confident that the contribution of the diffusivity to the resistance is significant also at this position.

The permeation coefficient calculated via Eq. 4.3 from $D_{\mathrm{T}}^{\mathrm{RTT}}(z)$ (thus not accounting for memory) is $P = 9.84 \pm 0.59$ μm/s, while experimental values between $20 - 150$ μm/s have been measured at slightly lower temperatures [6, 147–149]. The low value from our simulation can be explained by the difference in the free energy. As the main contribution to the permeation coefficient stems from the center of the membrane, the difference of

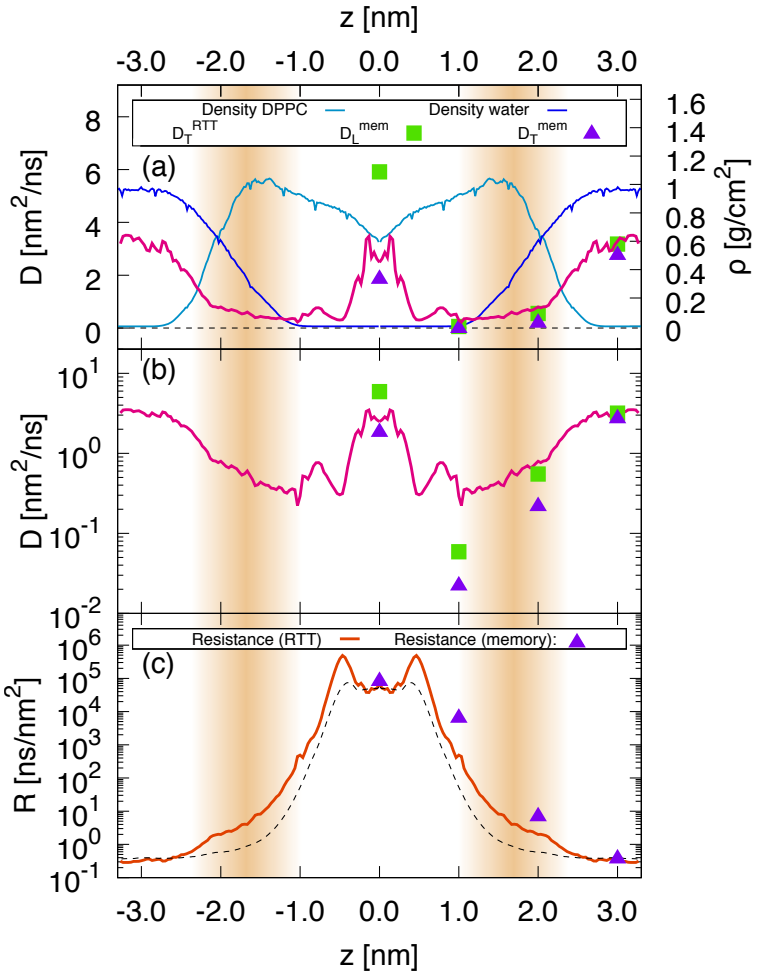

FIGURE 4.8: (a) Diffusivity profile $D(z)$ of a water molecule within the DPPC membrane computed from the round trip times using Eq. 4.7 (red). For three positions, the lateral diffusivity is included (green squares), and in the water phase also the transversal diffusivity computed from the transversal memory kernels (purple triangles). The blue lines indicate the water and the lipid density, and the orange background highlights the headgroup region. (b) The same data in a log-lin representation. (c) Local resistance $R(z)$ computed from the free energy profile $\mathcal{F}(z)$ in Fig. 4.2 and the diffusivity profile in $D_T^{RTT}(z)$ (red line) and from $D_T^{mem}(z)$ (purple triangles). The dashed black line indicates a hypothetical resistance $R_{hyp}(z)$ assuming a flat diffusivity of $D = 2.8$ nm^2/ns and serves as an illustration of the influence of $\mathcal{F}(z)$ and $D_T(z)$ on $R(z)$.

8 kJ/mol between the free energy barrier in our simulations and the experimental value of 24 kJ/mol from water solubility in hexadecane (see Sec. 4.4) corresponds to a factor of approximately 20 in the permeability. This puts our result into the range of earlier simulation studies, which yielded 700 ± 300 μm/s at 350 K [34] with a free energy barrier of 25 kJ/mol and 133 ± 28 μm/s at 323 K [36] with a free energy barrier of 23 kJ/mol. In general, the simulation results are at the upper boundary of the experimental values for the permeability or even above. It thus emerges that in order to compute the correct diffusivity profile $D_T(z)$ it is important to take into account the memory effects discussed in this work, since they can reduce the permeability up to one order of magnitude, which then places the simulation results in the middle of the experimental range.

4.7 Summary

In this work we have shown that it is possible to model the permeation of water through lipid membranes by atomistic molecular dynamics simulations. We have first computed a diffusivity profile of the water molecules within the membrane by the round-trip time (RTT) method, which assumes memoryless water dynamics. From the results of this method, which is computationally least expensive, a permeation resistance profile $R(z)$ has been determined. In agreement with literature [34, 36], the RTT method has yielded the result that the permeation process is mainly determined by the free energy profile, which exhibits a maximum in the membrane center, as the diffusivity only changes by one order of magnitude. The permeation coefficient from the RTT method is by a factor of 20 smaller than in literature, which can be explained by difference of 7 kJ/mol in the free energy maximum. In a next step, we have computed the memory kernels of the water dynamics at 4 positions within the system and have found an approximate functional expression for the long time behaviour of the memory kernels. These expressions have been integrated in order to compute a diffusivity which takes into account long time memory effects. We have seen that the diffusion of water inside the membrane is highly anisotropic, as the lateral diffusivity is a factor of $2 - 2.5$ higher than the transversal diffusivity. This anisotropy has been related to a slower relaxation of the lipid chain dynamics in transversal direction compared to the lateral direction. Moreover, the transversal diffusivity obtained by this method is, depending on the position, a factor of up to 20 lower than the diffusivity in the memoryless model, and exhibits a variation of more than two orders of magnitude along the membrane normal. Thus, the influence of the diffusivity on the permeation coefficient is heavily underestimated in memoryless models. Nevertheless, the memoryless RTT method provides useful information about the permeation process, as it correctly produces all maxima and minima of the diffusivity and yields a complete profile at computational costs which are only about 10 % of the calculation of memory kernels. In contrast to this, the determination of the memory kernels is only possible at particular positions where the free energy profile is smooth. We thus conclude that the application of both methods in parallel is the best strategy to tackle the determination of permeation coefficients.

4.8 Appendix

4.8.1 Derivation of Eq. 4.3

Assuming a stationary process $\frac{\partial}{\partial t}\rho(z,t) = 0$, we see from the FPE in Eq. 4.2 that the flux

$$J = -D(z)\,\mathrm{e}^{-\beta\mathcal{F}(z)}\frac{\partial}{\partial z}\left(\mathrm{e}^{\beta\mathcal{F}(z)}\rho(z,t)\right)$$

is constant. A rearrangement of terms and integration over the entire membrane from z_1 to z_2 results in

$$J \int_{z_1}^{z_2} \mathrm{d}z \, \frac{\mathrm{e}^{\beta \mathcal{F}(z)}}{D(z)} = -\,\mathrm{e}^{\beta \mathcal{F}(z_2)} \rho(z_2) + \mathrm{e}^{\beta \mathcal{F}(z_1)} \rho(z_1) \,.$$

We now use the fact that outside the membrane the free energy is constant $\mathcal{F}(z_1) = \mathcal{F}(z_2) = \mathcal{F}_0$, hence

$$J \int_{z_1}^{z_2} \mathrm{d}z \, \frac{\mathrm{e}^{\beta (\mathcal{F}(z) - \mathcal{F}_0)}}{D(z)} = \rho(z_1) - \rho(z_2) \,.$$

With the definition of the permeation coefficient in Eq. 4.1, we finally arrive at

$$\frac{1}{P} = \int_{z_1}^{z_2} \mathrm{d}z \, \frac{\mathrm{e}^{\beta (\mathcal{F}(z) - \mathcal{F}_0)}}{D(z)} \,, \tag{4.14}$$

which is identical to Eq. 4.3.

4.8.2 Derivation of Eq. 4.12

From the inset of Fig. 4.3 we observe that the exponent $\alpha(t)$ of the MSD has for large times t the functional form $1 - \alpha(t) = (t/\tau)^{-b}$. Integrating the definition $\alpha(t) = \mathrm{d} \ln \left\langle \Delta x^2(t) \right\rangle / \mathrm{d} \ln t$ it thus follows

$$\begin{aligned} \int_{\ln t_0}^{\ln t} \mathrm{d} \ln t \frac{\mathrm{d} \ln \left\langle \Delta x^2(t) \right\rangle}{\mathrm{d} \ln t} &= \int_{\ln t_0}^{\ln t} \mathrm{d} \ln t \, \left[1 - \mathrm{e}^{-b \ln(t/\tau)} \right] \\ &= \ln t - \ln t_0 + \frac{t^{-b} - t_0^{-b}}{b \tau^{-b}} \\ &= \ln \left\langle \Delta x^2(t) \right\rangle - \ln \left\langle \Delta x^2(t_0) \right\rangle \,, \end{aligned}$$

where t_0 is an arbitrary integration boundary. Solving this for $\left\langle \Delta x^2(t) \right\rangle$ we obtain

$$\left\langle \Delta x^2(t) \right\rangle = \left\langle \Delta x^2(t_0) \right\rangle \frac{t}{t_0} \exp \left(\frac{t^{-b} - t_0^{-b}}{b \tau^{-b}} \right) \,. \tag{4.15}$$

The time derivative of the MSD is then given by

$$\frac{\mathrm{d} \left\langle \Delta x^2(t) \right\rangle}{\mathrm{d}t} = \frac{\left\langle \Delta x^2(t_0) \right\rangle}{t_0} \exp \left(\frac{t^{-b} - t_0^{-b}}{b \tau^{-b}} \right) \left(1 - \frac{\tau^b}{t^b} \right) \,.$$

In the limit $t \to \infty$ this expression is proportional to the diffusion coefficient D_L, since for a markovian system the diffusion coefficient is defined as $2 D_\mathrm{L} t = \left\langle \Delta x^2(t) \right\rangle$. Hence, for the diffusion coefficient we obtain

$$D_\mathrm{L} = \frac{\left\langle \Delta x^2(t_0) \right\rangle}{2 t_0} \exp \left[-\frac{1}{b} \left(\frac{\tau}{t_0} \right)^b \right] \,.$$

Inserting this into Eq. 4.15 immediately yields Eq. 4.12.

4.8.3 Motivation of Eq. 4.13

In the previous section we have shown that the time derivative of the MSD follows the functional form

$$\frac{\mathrm{d}\left\langle \Delta x^2(t)\right\rangle}{\mathrm{d}t} = 2D_{\mathrm{L}} \exp\left[\frac{1}{b}\left(\frac{\tau}{t}\right)^b\right]\left(1-\frac{\tau^b}{t^b}\right),$$

which in the limit $t \to \infty$ yields the lateral diffusion coefficient. The Einstein relation tells that the diffusion coefficient D and the friction coefficient γ are related via $D = k_B T/\gamma$. We now assume that this relation, at least approximately, also holds for the long time behavior of both quantities, i.e. $D(t) \overset{t\,\text{large}}{\approx} k_B T/\gamma(t)$, where the time-dependent diffusion coefficient is given by $D(t) = \mathrm{d}\left\langle \Delta x^2(t)\right\rangle /2\mathrm{d}t$ and the time-dependent friction coefficient is connected with the memory kernel by $\Gamma(t) = \mathrm{d}\gamma(t)/\mathrm{d}t$. For memory kernels with a power law behavior this relation has been proven explicitly [166], and it also follows for the long time behavior of kernels with exponential decay [167]. Using this assumption, the time-dependent friction coefficient reads

$$\begin{aligned}\gamma(t) &= \frac{k_B T}{D}\exp\left[-\frac{1}{b}\left(\frac{\tau}{t}\right)^b\right]\left(\frac{(t/\tau)^b}{(t/\tau)^b-1}\right)\\ &\overset{t\gg\tau}{\approx} \frac{k_B T}{D}\exp\left[-\frac{1}{b}\left(\frac{\tau}{t}\right)^b\right].\end{aligned}$$

Taking the time derivative of this expression we arrive at an equation for the long time behaviour of the memory kernel, which reads

$$\Gamma(t) = \frac{k_B T}{D\tau}\left(\frac{\tau}{t}\right)^{b+1}\exp\left[-\frac{1}{b}\left(\frac{\tau}{t}\right)^b\right].$$

Chapter 5

Summary and Outlook

In this thesis, we have addressed the question of permeation processes through lipid bilayers with molecular dynamics (MD) simulations. An emphasis has been put on the inclusion of memory effects in the motion of the solute particle, which has been described by the generalized Langevin equation. In the scope of this work we have investigated the interactions between bilayers and the permeation of water through the bilayer, and discussed our results by comparing them to other simulations or, if available, experiments found in literature. A second focus of this thesis has been the development of a method to extract memory kernels from particle trajectories generated by MD simulations, thus this work has both a physical as well as methodological aspect.

Since the lipid phase determines the permeation properties of lipid membranes, we have studied the hydration pressure between lipid bilayers in the gel and fluid phase in Chapter 2. We have shown that the disagreement between the experimental works on the hydration pressures between membranes disappears when all data is expressed as a function of the repeat distance. In order to compare the experiments with our simulations, we have then consistently transformed the experimentally measured pressure from a function of the repeat distance to a function of the membrane separation. In this representation our data simulation data reproduces the experimental results and reveals a factor of roughly two between the decay lengths in the gel and the fluid phase. We have then decomposed the hydration pressure p into a direct membrane–membrane interaction p_{dir} and an indirect water-mediated interaction p_{ind}. For both phases the attractive pressure p_{dir} and the repulsive pressure p_{ind} are approximately one order of magnitude larger than p and nearly cancel each other. Thus, we have concluded that the hydration repulsion is the result of a subtle interplay of highly attractive membrane–membrane interactions and highly repulsive water-mediated interactions, with the repulsion slightly overcompensating the attraction. The result of the near-cancellation of the two contributions is the hydration pressure measured in the experiments.

The influence of confinements on the friction coefficient of molecules solvated in water has been investigated in Chapter 3. We have constrained the motion of several molecules by harmonic potentials and have computed their position and velocity autocorrelation functions. From these quantities, we have determined the memory kernels of the solutes

and their integrals by the application of a modified iterative method based on the work of Berne at al. [63]. As solutes we have chosen methane, water, Na^+-ions, Na^--ions and glycerol, which provide a variation in hydrophilicity, charge and size. By extrapolating the integrals of the memory kernels to $t \to \infty$, it has been observed that for all molecules the friction coefficient increases with the stiffness of confining potential. This effect is most pronounced for water and methane, where an increase of up to 50 % has been obtained, in comparison to 5 % for glycerol. The increase of the friction, which mainly stems from the long time behavior of the memory kernels, is accompanied by a simultaneous slowdown of the solvent dynamics around the solutes. By replacing the water by water-glycerol mixtures, we have changed the viscosity of the solvent and observed that the longest relaxation time τ^L of the memory kernel of the solute increases with the solvent viscosity. We have thus concluded that τ^L corresponds to the time scale of the solvent relaxation. A second important observation has been that the friction increase in confinement is enhanced in viscous fluids. This result has been explained by a scaling argument: If the relaxation time of the solvent, which increases with the viscosity, is larger than the time scale of the transition from inertial to diffusive dynamics, confinement-dependent friction emerges. The picture goes beyond Stokes' law, where it is assumed that the solvent friction on a particle is a function of the hydrodynamic particle radius and the solvent viscosity only.

Using the method of kernel extraction developed in Chapter 3, it has been shown in Chapter 4 that the consideration of memory effects significantly decreases the calculated diffusion coefficient. In the interior of the membrane, a reduction of the diffusion coefficient by a factor of up to 20 has been observed compared to a memoryless model for the description of the molecule motion. Whereas earlier studies [34, 36] suggested that the permeation barrier of a lipid bilayer for water is mainly determined by the free energy, the results of this thesis indicate that the permeation process is more complicated. Indeed, in a region of 2 nm around the central plane of the membrane, contributions from the free energy and from the diffusivity to the permeation resistance both vary by approximately two orders of magnitude along the membrane normal. In addition, a strong anisotropy in the water diffusion has been observed inside the membrane, which is linked to an extended long time decay of the memory kernel in transversal direction. Following our argumentation in Chapter 3, we have concluded that this indicates that the relaxation of the lipid chains in the bilayer interior is slower in transversal direction than in lateral direction.

In conclusion we have demonstrated that MD simulations are able to give insight into the molecular mechanisms of permeation processes of molecules through a lipid bilayer. We have also proven that memory effects are important during the permeation and their explicit consideration leads to a decrease of the diffusivity by more than one order of magnitude. This result is of particular importance for transdermal drug delivery, since it serves as a connection between molecular properties of molecules and macroscopic free energies and diffusivities extracted from concentration profiles which are measured in experiments [150]. Consequently, since the outermost layers of skin, the stratum corneum, includes domains which are in the gel phase, a simulation study of the permeation of molecules through gel membranes is the next step towards a complete picture of drug transport through skin.

Appendix A

Constructing Membranes in Gel Phase

Schubert et al. [100] have demonstrated that, within a reasonable simulation time, a simple freezing of a membrane in fluid phase provides a membrane that exhibits large differences in its structural parameters when compared to experimental values of membranes in the gel phase. It is therefore necessary to construct membranes in the gel phase manually while ensuring that the resulting structure is as little biased as possible. The method presented here generates membranes whose structural as well as thermodynamic properties are close to the values measured in experiments of membranes in the gel phase.

As a starting structure, we use two DPPC molecules that are orientated such that their hydrocarbon chains are pointing towards each other (Fig. A.1 (a)). In both molecules we restrain all dihedrals of the hydrocarbon chains to the trans position. In a first step, each of the lipid molecules is copied eight times and arranged on a hexagonal lattice, thus forming a small bilayer. Subsequently, each of the 18 molecules is rotated by a random angle around its principle axis (Fig. A.1 (b)). The solvation of this structure is technically realized as follows: We first increase the van-der-Waals-radii of the carbon atoms, such that it becomes energetically highly unfavourable to place water molecules into the chain region. Into the free space of the simulation box we then insert water molecules, which are consequently only placed outside the membrane structure. At this point, we perform a first energy minimization of the system in order to remove overlaps between the molecules. Next we restrain the x- and y-coordinates of all atoms of the lipid molecules, introduce a weak harmonic potential on their z-coordinates and let the water propagate freely through the system. This way we allow for small configurational changes in the bilayer while the water diffuses in between the headgroups. This equilibration run is very short ($\sim$ 50 ps, $T = 270\,\mathrm{K}$) and is only necessary to put the bilayer and the water molecules into contact with each other.

After removing all restraints on lipid molecules except for the dihedrals, we equilibrate the system for 500 ps in order to allow the hydrocarbon chains to tilt their vertical orientation. This tilt is a result of tendency of the chains to minimize the free volume in the

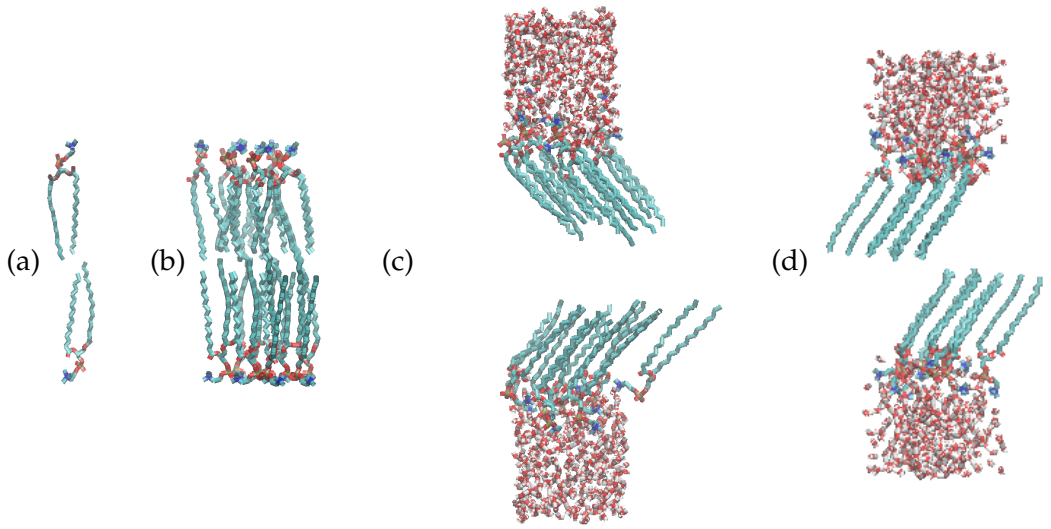

FIGURE A.1: Construction of a gel membrane. (a) The starting structure, which consists of two DPPC molecules pointing towards each other. Copying these two molecules eight times, arranging all of the molecules on two opposing hexagonal lattices and rotating each molecule by a random angle around its principle axis yields structure (b). In (c), the structure is hydrated and equilibrated with fixed dihedral angles. In the next step, one of the resulting leaflets is then removed, while the other is copied, flipped and rotated by 180° (d). This structure is then heated from $T = 270$ K up to $T = 300$ K with loose dihedrals, which produces the final bilayer system in Fig. 2.2 (a).

membrane interior. Additionally, we impose a pressure coupling of 1 bar in lateral direction to make the bilayer adopt its intrinsic area per lipid and close small pores that might have arisen during the construction, thus preventing water molecules from diffusing into the hydrophobic chain region. The tilting of the chains creates an empty space between both leaflets of the bilayer (Fig. A.1 (c)). Consequently the leaflets of the bilayer decouple and each leaflet independently adopts a configuration that is energetically most favorable, which for DPPC corresponds to the arrangement of the chains on a hexagonal lattice. Due to the decoupling of both leaflets, the orientation of the chains in lateral (xy-) direction will differ between both leaflets. The application of a pressure coupling to the z-dimension of simulation box, which removes the free volume between the membranes by scaling down the simulation box, prevents the two leaflets from decoupling. However this often (but not always) leads to structures that are in a metastable states: One of the leaflets attains its preferred lattice structure first and, due to interactions of the chains of both leaflets, imposes its lattice structure on the chains of the other leaflet. Since this second leaflet thus becomes frustrated, it is therefore not advisable to choose this procedure.

For the system with decoupled leaflets, there are two options to put the leaflets into contact: The first way is to rotate one layer, remove the free space and execute an equilibration run of sufficient length such the lattices arrange themselves in a configuration of minimal energy. Since the cubic simulation box is incompatible with the hexagonal lattice, rotations

of the box by multiples of 90° create mismatches in the lattice structure, which then again may create strong frustrations in one of the layers. We therefore choose a different way, which is simply replacing one layer by a flipped and rotated copy of the other. Thus, it is ensured that both leaflets preserve their configuration of minimal energy even after getting into contact with each other. We then remove the empty space between the leaflets and perform another energy minimization, since there might exist overlaps of the chains of the leaflets. This is then followed by another equilibration run of 500 ps. The resulting bilayer (Fig. A.1 (d)) should now have reached the correct configuration of minimal energy.

In the last step, we copy the simulation box once in x- and y-directions, hence obtaining four times the amount of lipids in the system. In a following simulation we heat the system slowly ($\sim$ 20 ns) from a temperature of 270 K up to 300 K, now with unrestrained dihedrals. This last equilibration run should be performed carefully enough not to destroy the ordering of the lipid chains. In order to check the properties of the final structure, it is possible to heat it to higher temperatures ($T \approx 330$ K) and measure the transition enthalpy from the gel to the fluid state, which in experiments is measured to be $35 - 40$ kJ/mol [17, 19, 168–170]. Additionally, global system parameters like the mean tilt angle, the area per lipid or the number of gauche bonds per lipid chain can be determined and compared to experiments [171, 172].

List of Publications

The present thesis is based on the following manuscripts, which have been published or are in preparation for publication in peer-reviewed journals:

i Bartosz Kowalik, Alexander Schlaich, Matej Kanduč, Emanuel Schneck, and Roland R. Netz, "Hydration Repulsion Difference between Ordered and Disordered Membranes due to Cancellation of Membrane–Membrane and Water-mediated Interactions", *J. Phys. Chem. Lett.*, vol. 8, pp 2869-2874, **2017**, doi:10.1021/acs.jpclett.7b00977

ii Bartosz Kowalik, Jan O. Daldrop, Julian Kappler, Julius C. F. Schulz, Alexander Schlaich, and Roland R. Netz, "Confinement-induced Increase of Molecular Friction is Measured for Small Solute Molecules in Water and Enhanced by Viscous Solvents", *in preparation*

iii Bartosz Kowalik, and Roland R. Netz, "Memory Effects in the Permeation of Water through a Lipid Bilayer", *in preparation*

Publications not discussed within this thesis

iv Alexander Schlaich, Bartosz Kowalik, Matej Kanduč, Emanuel Schneck, and Roland R. Netz, "Physical Mechanisms of the Interaction between Lipid membranes in the Aqueous Environment" *Physica A*, vol. 418, pp 105-125, **2015**

v Bartosz Kowalik, Thomas Schubert, Hirofumi Wada, Motomu Tanaka, Roland R. Netz, and Emanuel Schneck, "Combination of MD Simulations with Two-State Kinetic Rate Modeling Elucidates the Chain Melting Transition of Phospholipid Bilayers for Different Hydration Levels", *J. Phys. Chem. B*, vol. 119(44), pp 14157-14167, **2015**

vi Jan O. Daldrop, Bartosz Kowalik, and Roland R. Netz, "External Potential Modifies Friction of Molecular Solutes in Water" *Phys. Rev. X*, vol. 7, p 041065, **2017**

In preparation

vii Alexander Schlaich, Jan O. Daldrop, Bartosz Kowalik, Matej Kanduč, Emanuel Schneck, and Roland R. Netz, "Landau Ginzburg Theory for Membrane Interactions", *in preparation*

Book chapters

viii Alexander Schlaich, Bartosz Kowalik, Matej Kanduč, Emanuel Schneck, and Roland R. Netz, "Simulation Techniques for Solvation-Induced Surface-Interactions at Prescribed Water Chemical Potential", in *Computational Trends in Solvation and Transport in Liquids*, vol. 28, Godehard Sutmann, Johannes Grotendorst, Gerhard Gompper, and Dominik Marx, Eds. Jülich: Forschungszentrum Jülich GmbH, pp. 155-185, **2015**

Bibliography

[1] Singer, S. J. & Nicolson, G. L. The fluid mosaic model of the structure of cell membranes. *Science* **175**, 720–731 (1972).

[2] Stein, W. *Transport and diffusion across cell membranes* (Elsevier, 2012).

[3] Doherty, G. J. & McMahon, H. T. Mechanisms of endocytosis. *Annual Review of Biochemistry* **78**, 857–902 (2009).

[4] SKou, J. C. Enzymatic basis for active transport of na+ and k+ across cell membrane. *Physiological reviews* **45**, 596–618 (1965).

[5] Souba, W. W. & Pacitti, A. J. Review: How amino acids get into cells: Mechanisms, models, menus, and mediators. *Journal of Parenteral and Enteral Nutrition* **16**, 569–578 (1992).

[6] Finkelstein, A. Water and nonelectrolyte permeability of lipid bilayer membranes. *The Journal of General Physiology* **68**, 127–135 (1976).

[7] Van Meer, G., Voelker, D. R. & Feigenson, G. W. Membrane lipids: where they are and how they behave. *Nat. Rev. Mol. Cell Bio.* **9**, 112–124 (2008).

[8] Tanford, C. *et al.* The hydrophobic effect and the organization of living matter. *Science* **200**, 1012–1018 (1978).

[9] Luzzati, V. & Tardieu, A. Lipid phases: Structure and structural transitions. *Annual Review of Physical Chemistry* **25**, 79–94 (1974).

[10] Seddon, J. M. Structure of the inverted hexagonal (hii) phase, and non-lamellar phase transitions of lipids. *Biochimica et Biophysica Acta (BBA) - Reviews on Biomembranes* **1031**, 1 – 69 (1990).

[11] Luisi, P. L., Walde, P. & Oberholzer, T. Lipid vesicles as possible intermediates in the origin of life. *Current Opinion in Colloid and Interface Science* **4**, 33 – 39 (1999).

[12] Yeagle, P. L. *The membranes of cells* (Academic Press, 2016).

[13] Pierce, K. L., Premont, R. T. & Lefkowitz, R. J. Seven-transmembrane receptors. *Nature reviews. Molecular cell biology* **3**, 639 (2002).

[14] Benoit, M., Gabriel, D., Gerisch, G. & Gaub, H. E. Discrete interactions in cell adhesion measured by single-molecule force spectroscopy. *Nature cell biology* **2**, 313–317 (2000).

[15] Monnard, P.-A. & Deamer, D. W. Membrane self-assembly processes: Steps toward the first cellular life. *The Anatomical Record* **268**, 196–207 (2002).

[16] Segré, D., Ben-Eli, D., Deamer, D. W. & Lancet, D. The lipid world. *Origins of Life and Evolution of the Biosphere* **31**, 119–145 (2001).

[17] Janiak, M. J., Small, D. M. & Shipley, G. G. Nature of the thermal pretransition of synthetic phospholipids: dimyristoyl-and dipalmitoyllecithin. *Biochemistry* **15**, 4575–4580 (1976).

[18] Nagle, J. F. & Tristram-Nagle, S. Structure of lipid bilayers. *Biochimica et Biophysica Acta (BBA) - Reviews on Biomembranes* **1469**, 159 – 195 (2000).

[19] Mabrey, S. & Sturtevant, J. M. Investigation of phase transitions of lipids and lipid mixtures by sensitivity differential scanning calorimetry. *Proceedings of the National Academy of Sciences* **73**, 3862–3866 (1976).

[20] Lee, A. Lipid phase transitions and phase diagrams i. lipid phase transitions. *Biochimica et Biophysica Acta (BBA) - Reviews on Biomembranes* **472**, 237 – 281 (1977).

[21] Nagle, J. F. Theory of the main lipid bilayer phase transition. *Annual Review of Physical Chemistry* **31**, 157–196 (1980).

[22] Mouritsen, O. Theoretical models of phospholipid phase transitions. *Chemistry and Physics of Lipids* **57**, 179 – 194 (1991).

[23] Kowalik, B. *et al.* Combination of md simulations with two-state kinetic rate modeling elucidates the chain melting transition of phospholipid bilayers for different hydration levels. *The Journal of Physical Chemistry B* **119**, 14157–14167 (2015).

[24] Madison, K. C. Barrier function of the skin: „La Raison d'Être“ of the epidermis. *Journal of Investigative Dermatology* **121**, 231 – 241 (2003).

[25] Tristram-Nagle, S. *et al.* Measurement of chain tilt angle in fully hydrated bilayers of gel phase lecithins. *Biophysical journal* **64**, 1097–1109 (1993).

[26] Sparr, E. & Wennerström, H. Responding phospholipid membranes-interplay between hydration and permeability. *Biophysical journal* **81**, 1014–1028 (2001).

[27] Elias, P. M. Epidermal barrier function: intercellular lamellar lipid structures, origin, composition and metabolism. *Journal of Controlled Release* **15**, 199 – 208 (1991).

[28] Cevc, G. & Vierl, U. Nanotechnology and the transdermal route: A state of the art review and critical appraisal. *Journal of Controlled Release* **141**, 277 – 299 (2010). Pharmaceutical Nanotechnology: Unmet Needs in Drug Delivery.

[29] Blanco, E., Shen, H. & Ferrari, M. Principles of nanoparticle design for overcoming biological barriers to drug delivery. *Nature biotechnology* **33**, 941–951 (2015).

[30] Hanai, T. & Haydon, D. The permeability to water of bimolecular lipid membranes. *Journal of Theoretical Biology* **11**, 370 – 382 (1966).

[31] Orbach, E. & Finkelstein, A. The nonelectrolyte permeability of planar lipid bilayer membranes. *The Journal of General Physiology* **75**, 427–436 (1980).

[32] Finkelstein, A. & Cass, A. Permeability and electrical properties of thin lipid membranes. *The Journal of General Physiology* **52**, 145–172 (1968).

[33] Diamond, J. M. & Katz, Y. Interpretation of nonelectrolyte partition coefficients between dimyristoyl lecithin and water. *The Journal of Membrane Biology* **17**, 121–154 (1974).

[34] Marrink, S.-J. & Berendsen, H. J. C. Simulation of water transport through a lipid membrane. *J. Phys. Chem.* **98**, 4155–4168 (1994).

[35] Marrink, S. J. & Berendsen, H. J. C. Permeation process of small molecules across lipid membranes studied by molecular dynamics simulations. *The Journal of Physical Chemistry* **100**, 16729–16738 (1996).

[36] Bemporad, D., Essex, J. W. & Luttmann, C. Permeation of small molecules through a lipid bilayer: A computer simulation study. *The Journal of Physical Chemistry B* **108**, 4875–4884 (2004).

[37] Ulander, J. & Haymet, A. Permeation across hydrated dppc lipid bilayers: simulation of the titrable amphiphilic drug valproic acid. *Biophysical journal* **85**, 3475–3484 (2003).

[38] Van Kampen, N. G. *Stochastic processes in physics and chemistry*, vol. 1 (Elsevier, 1992).

[39] Zwanzig, R. *Nonequilibrium statistical mechanics* (Oxford University Press, 2001).

[40] Coffey, W. T. & Kalmykov, Y. P. *The Langevin equation: with applications to stochastic problems in physics, chemistry and electrical engineering* (World Scientific, 2004).

[41] Kubo, R. The fluctuation-dissipation theorem. *Reports on progress in physics* **29**, 255 (1966).

[42] Mori, H. Transport, collective motion, and brownian motion. *Progress of Theoretical Physics* **33**, 423 (1965).

[43] Adelman, S. A. & Doll, J. D. Generalized langevin equation approach for atom/solid-surface scattering: General formulation for classical scattering off harmonic solids. *The Journal of Chemical Physics* **64**, 2375–2388 (1976).

[44] Panja, D. Anomalous polymer dynamics is non-markovian: memory effects and the generalized langevin equation formulation. *Journal of Statistical Mechanics: Theory and Experiment* **2010**, P06011 (2010).

[45] Bloom, M. & Sternin, E. Transverse nuclear spin relaxation in phospholipid bilayer membranes. *Biochemistry* **26**, 2101–2105 (1987).

[46] Langmuir, I. The role of attractive and repulsive forces in the formation of tactoids, thixotropic gels, protein crystals and coacervates. *J. Chem. Phys.* **6**, 873–896 (1938).

[47] Klein, J. Hydration lubrication. *Friction* **1**, 1–23 (2013).

[48] Lis, L., McAlister, M., Fuller, N., Rand, R. & Parsegian, V. Interactions between neutral phospholipid bilayer membranes. *Biophys. J.* **37**, 657 (1982).

[49] Marra, J. & Israelachvili, J. Direct measurements of forces between phosphatidylcholine and phosphatidylethanolamine bilayers in aqueous electrolyte solutions. *Biochemistry* **24**, 4608–4618 (1985).

[50] Rand, R. & Parsegian, V. Hydration forces between phospholipid bilayers. *Biochim. Biophys. Acta - Biomembranes* **988**, 351 – 376 (1989).

[51] Leikin, S., Parsegian, V. A., Rau, D. C. & Rand, R. P. Hydration forces. *Annu. Rev. Phys. Chem.* **44**, 369–395 (1993).

[52] Israelachvili, J. N. & Pashley, R. M. Molecular layering of water at surfaces and origin of repulsive hydration forces. *Nature* **306**, 249–250 (1983).

[53] Parsegian, V., Fuller, N. & Rand, R. Measured work of deformation and repulsion of lecithin bilayers. *Proc. Natl. Acad. Sci.* **76**, 2750–2754 (1979).

[54] Marčelja, S. & Radić, N. Repulsion of interfaces due to boundary water. *Chem. Phys. Lett.* **42**, 129–130 (1976).

[55] Parsegian, V. & Zemb, T. Hydration forces: Observations, explanations, expectations, questions. *Curr. Opin. Colloid Interface Sci.* **16**, 618–624 (2011).

[56] Israelachvili, J. & Wennerström, H. Role of hydration and water structure in biological and colloidal interactions. *Nature* **379**, 219–225 (1996).

[57] Schneck, E., Sedlmeier, F. & Netz, R. R. Hydration repulsion between biomembranes results from an interplay of dehydration and depolarization. *Proc. Natl. Acad. Sci.* **109**, 14405–14409 (2012).

[58] Kanduč, M., Schneck, E. & Netz, R. R. Hydration interaction between phospholipid membranes: Insight into different measurement ensembles from atomistic molecular dynamics simulations. *Langmuir* **29**, 9126–9137 (2013).

[59] Veldhuizen, R., Nag, K., Orgeig, S. & Possmayer, F. The role of lipids in pulmonary surfactant. *Biochimica et Biophysica Acta (BBA) - Molecular Basis of Disease* **1408**, 90 – 108 (1998).

[60] McIntosh, T. J. Short-range interactions between lipid bilayers measured by x-ray diffraction. *Curr. Opin. Struct. Biol.* **10**, 481 – 485 (2000).

[61] Burling, F. T., Weis, W. I., Flaherty, K. M. & Brünger, A. T. Direct observation of protein solvation and discrete disorder with experimental crystallographic phases. *Science* **271**, 72–77 (1996).

[62] Ebbinghaus, S. *et al.* An extended dynamical hydration shell around proteins. *Proceedings of the National Academy of Sciences of the United States of America* **104**, 20749–20752 (2007).

[63] Berne, B. J. & Harp, G. D. *On the Calculation of Time Correlation Functions*, 63–227 (John Wiley and Sons, Inc., 1970).

[64] Hinczewski, M., von Hansen, Y., Dzubiella, J. & Netz, R. R. How the diffusivity profile reduces the arbitrariness of protein folding free energies. *J. Chem. Phys.* **132**, 245103+ (2010).

[65] Sedlmeier, F., von Hansen, Y., Mengyu, L., Horinek, D. & Netz, R. R. Water dynamics at interfaces and solutes: Disentangling free energy and diffusivity contributions. *Journal of Statistical Physics* **145**, 240–252 (2011).

[66] Kowalik, B., Schlaich, A., Kanduč, M., Schneck, E. & Netz, R. R. Hydration repulsion difference between ordered and disordered membranes due to cancellation of membrane-membrane and water-mediated interactions. *J. Phys. Chem. Lett.* **8**, 2869–2874 (2017).

[67] Israelachvili, J. N. & Wennerström, H. Entropic forces between amphiphilic surfaces in liquids. *J. Phys. Chem.* **96**, 520–531 (1992).

[68] Ducker, W. A., Senden, T. J. & Pashley, R. M. Direct measurement of colloidal forces using an atomic force microscope. *Nature* **353**, 239 (1991).

[69] Rau, D., Lee, B. & Parsegian, V. Measurement of the repulsive force between polyelectrolyte molecules in ionic solution: hydration forces between parallel dna double helices. *Proc. Natl. Acad. Sci.* **81**, 2621–2625 (1984).

[70] Leikin, S., Rau, D. & Parsegian, V. Direct measurement of forces between self-assembled proteins: temperature-dependent exponential forces between collagen triple helices. *Proc. Natl. Acad. Sci.* **91**, 276–280 (1994).

[71] Leikin, S. L., Kozlov, M. M., Chernomordik, L. V., Markin, V. S. & Chizmadzhev, Y. A. Membrane fusion: Overcoming of the hydration barrier and local restructuring. *J. Theor. Biol.* **129**, 411 – 425 (1987).

[72] Lu, D. R., Lee, S. J. & Park, K. Calculation of solvation interaction energies for protein adsorption on polymer surfaces. *J. Biomater. Sci. Polym. Ed.* **3**, 127–147 (1992).

[73] Gaisinskaya, A. *et al.* Hydration lubrication: exploring a new paradigm. *Farad. Discuss.* **156**, 217–233 (2012).

[74] Chen, H., Cox, J. R., Ow, H., Shi, R. & Panagiotopoulos, A. Z. Hydration repulsion between carbohydrate surfaces mediated by temperature and specific ions. *Sci. Rep.* **6**, 28553 (2016).

[75] Cevc, G., Podgornik, R. & Žekš, B. The free energy,enthalpy and entropy of hydration of phospholipid bilayer membranes and their difference on the interfacial separation. *Chem. Phys. Lett.* **91**, 193–196 (1982).

[76] Israelachvili, J. & McGuiggan, P. Forces between surfaces in liquids. *Science* **241**, 795 – 800 (1988).

[77] Pashley, R. Hydration forces between mica surfaces in aqueous electrolyte solutions. *J. Colloid Interface Sci.* **80**, 153 – 162 (1981).

[78] LeNeveu, D. M., Rand, R. P. & Parsegian, V. A. Measurement of forces between lecithin bilayers. *Nature* **259**, 601–603 (1976).

[79] Horn, R., Israelachvili, J., Marra, J., Parsegian, V. & Rand, R. Comparison of forces measured between phosphatidylcholine bilayers. *Biophys. J.* **54**, 1185 (1988).

[80] Evans, E. & Parsegian, V. Thermal-mechanical fluctuations enhance repulsion between bimolecular layers. *Proc. Natl. Acad. Sci.* **83**, 7132–7136 (1986).

[81] Pabst, G., Katsaras, J., Raghunathan, V. A. & Rappolt, M. Structure and interactions in the anomalous swelling regime of phospholipid bilayers. *Langmuir* **19**, 1716–1722 (2003).

[82] Ichimori, H., Hata, T., Yoshioka, T., Matsuki, H. & Kaneshina, S. Thermotropic and barotropic phase transition on bilayer membranes of phospholipids with varying acyl chain-lengths. *Chem. Phys. Lipids* **89**, 97 – 105 (1997).

[83] Edidin, M. The state of lipid rafts: from model membranes to cells. *Annu. Rev. Biophys. Biomol. Struct* **32**, 257–283 (2003).

[84] McIntosh, T. J. & Simon, S. A. Contributions of hydration and steric (entropic) pressures to the interactions between phosphatidylcholine bilayers: Experiments with the subgel phase. *Biochemistry* **32**, 8374–8384 (1993).

[85] Gawrisch, K. *et al.* Membrane dipole potentials, hydration forces, and the ordering of water at membrane surfaces. *Biophys. J.* **61**, 1213 – 1223 (1992).

[86] Petrache, H. I. *et al.* Interbilayer interactions from high-resolution x-ray scattering. *Phys. Rev. E* **57**, 7014–7024 (1998).

[87] McIntosh, T. J. & Simon, S. A. Hydration force and bilayer deformation: a reevaluation. *Biochemistry* **25**, 4058–4066 (1986).

[88] Markova, N., Sparr, E., Wadsö, L. & Wennerström, H. A calorimetric study of phospholipid hydration. simultaneous monitoring of enthalpy and free energy. *J. Phys. Chem. B* **104**, 8053–8060 (2000).

[89] Tieleman, D., Marrink, S. & Berendsen, H. A computer perspective of membranes: molecular dynamics studies of lipid bilayer systems. *Biochim. Biophys. Acta - Biomembranes* **1331**, 235 – 270 (1997).

[90] Essmann, U., Perera, L. & Berkowitz, M. L. The origin of the hydration interaction of lipid bilayers from md simulation of dipalmitoylphosphatidylcholine membranes in gel and liquid crystalline phases. *Langmuir* **11**, 4519–4531 (1995).

[91] Hua, L., Zangi, R. & Berne, B. J. Hydrophobic interactions and dewetting between plates with hydrophobic and hydrophilic domains. *J. Phys. Chem. C* **113**, 5244–5253 (2009).

[92] Hayashi, T., Pertsin, A. J. & Grunze, M. Grand canonical monte carlo simulation of hydration forces between nonorienting and orienting structureless walls. *J. Chem. Phys.* **117**, 6271–6280 (2002).

[93] Pertsin, A., Fedyanin, I. & Grunze, M. Computer simulation of water-mediated forces between gel-phase phospholipid bilayers. *J. Chem. Phys.* **131**, 12B607 (2009).

[94] Attard, P., Mitchell, D. J. & Ninham, B. W. The attractive forces between polar lipid bilayers. *Biophys. J.* **53**, 457–460 (1988).

[95] Hess, B., Kutzner, C., Van Der Spoel, D. & Lindahl, E. Gromacs 4: algorithms for highly efficient, load-balanced, and scalable molecular simulation. *Journal of chemical theory and computation* **4**, 435–447 (2008).

[96] Tieleman, D. & Berendsen, H. J. C. Molecular dynamics simulations of a fully hydrated dipalmitoyl phosphatidylcholine bilayer with different macroscopic boundary conditions and parameters. *J. Chem. Phys.* **105**, 4871 (1996).

[97] Berger, O., Edholm, O. & Jahnig, F. Molecular dynamics simulations of a fluid bilayer of dipalmitoylphosphatidylcholine at full hydration, constant pressure, and constant temperature. *Biophys. J.* **72**, 2002 (1997).

[98] Lindahl, E. & Edholm, O. Mesoscopic undulations and thickness fluctuations in lipid bilayers from molecular dynamics simulations. *Biophys. J.* **79**, 426–433 (2000).

[99] Berendsen, H., Grigera, J. & Straatsma, T. The missing term in effective pair potentials. *Journal of Physical Chemistry* **91**, 6269–6271 (1987).

[100] Schubert, T., Schneck, E. & Tanaka, M. First order melting transitions of highly ordered dipalmitoyl phosphatidylcholine gel phase membranes in molecular dynamics simulations with atomistic detail. *J. Chem. Phys.* **135**, – (2011).

[101] Bussi, G., Donadio, D. & Parrinello, M. Canonical sampling through velocity rescaling. *The Journal of chemical physics* **126**, 014101 (2007).

[102] Coppock, P. S. & Kindt, J. T. Determination of phase transition temperatures for atomistic models of lipids from temperature-dependent stripe domain growth kinetics. *J. Phys. Chem. B* **114**, 11468–11473 (2010).

[103] Ulminus, J., Wennerstrom, H., Lindblom, G. & Arvidson, G. Deuteron nuclear magnetic resonance studies of phase equilibriums in a lecithin-water system. *Biochemistry* **16**, 5742–5745 (1977).

[104] Grabielle-Madelmont, C. & Perron, R. Calorimetric studies on phospholipid-water systems: I. dl-dipalmitoylphosphatidylcholine (dppc)-water system. *J. Colloid Interface Sci.* **95**, 471–482 (1983).

[105] Berendsen, H. J., Postma, J. v., van Gunsteren, W. F., DiNola, A. & Haak, J. Molecular dynamics with coupling to an external bath. *The Journal of chemical physics* **81**, 3684–3690 (1984).

[106] Darden, T., York, D. & Pedersen, L. Particle mesh ewald: An n log(n) method for ewald sums in large systems. *J. Chem. Phys.* **98**, 10089 (1993).

[107] Widom, B. Some topics in the theory of fluids. *J. Chem. Phys* **39**, 2808 (1963).

[108] Shirts, M. R. & Chodera, J. D. Statistically optimal analysis of samples from multiple equilibrium states. *J. Chem. Phys.* **129**, 124105 (2008).

[109] Tardieu, A., Luzzati, V. & Reman, F. Structure and polymorphism of the hydrocarbon chains of lipids: A study of lecithin-water phases. *J. Mol. Biol.* **75**, 711 – 733 (1973).

[110] McIntosh, T. J., Magid, A. D. & Simon, S. A. Steric repulsion between phosphatidylcholine bilayers. *Biochemistry* **26**, 7325–7332 (1987).

[111] Lee, S. *et al.* Charmm36 united atom chain model for lipids and surfactants. *The journal of physical chemistry B* **118**, 547–556 (2014).

[112] Jorgensen, W. L., Chandrasekhar, J., Madura, J. D., Impey, R. W. & Klein, M. L. Comparison of simple potential functions for simulating liquid water. *J. Chem. Phys.* **79**, 926–935 (1983).

[113] Loison, C. Hydrated dppc, md simulation trajectory and related files for ua charmm36 model by lee et al 2014 (2015).

[114] Botan, A. *et al.* Toward atomistic resolution structure of phosphatidylcholine headgroup and glycerol backbone at different ambient conditions. *J. Phys. Chem. B* **119**, 15075–15088 (2015).

[115] Bhushan, B., Israelachvili, J. N. & Landman, U. Nanotribology: friction, wear and. *Nature* **374**, 13 (1995).

[116] Nair, R. R., Wu, H. A., Jayaram, P. N., Grigorieva, I. V. & Geim, A. K. Unimpeded permeation of water through helium-leak–tight graphene-based membranes. *Science* **335**, 442–444 (2012).

[117] Cheng, P. Y. & Schachman, H. K. Studies on the validity of the einstein viscosity law and stokes' law of sedimentation. *Journal of Polymer Science* **16**, 19–30 (1955).

[118] Edward, J. T. Molecular volumes and the stokes-einstein equation. *Journal of Chemical Education* **47**, 261 (1970).

[119] Zwanzig, R. & Harrison, A. K. Modifications of the stokes-einstein formula. *J. Chem. Phys.* **83**, 5861–5862 (1985).

[120] Daldrop, J. O., Kowalik, B. G. & Netz, R. R. External potential modifies friction of molecular solutes in water. *Phys. Rev. X* **7**, 041065 (2017).

[121] Sterpone, F., Stirnemann, G. & Laage, D. Magnitude and molecular origin of water slowdown next to a protein. *J. Am. Chem. Soc.* **134**, 4116–4119 (2012).

[122] Mattea, C., Qvist, J. & Halle, B. Dynamics at the protein-water interface from ^{17}o spin relaxation in deeply supercooled solutions. *Biophys. J.* **95**, 2951–2963 (2008).

[123] Gottwald, F., Karsten, S., Ivanov, S. D. & Kühn, O. Parametrizing linear generalized Langevin dynamics from explicit molecular dynamics simulations. *The Journal of chemical physics* **142**, 244110 (2015).

[124] Shin, H. K., Kim, C., Talkner, P. & Lee, E. K. Brownian motion from molecular dynamics. *Chemical Physics* **375**, 316–326 (2010).

[125] Straub, J. E., Borkovec, M. & Berne, B. J. Calculation of dynamic friction on intramolecular degrees of freedom. *Journal of Physical Chemistry* **91**, 4995–4998 (1987).

[126] Gordon, D., Krishnamurthy, V. & Chung, S.-H. Generalized langevin models of molecular dynamics simulations with applications to ion channels. *The Journal of Chemical Physics* **131**, 134102 (2009).

[127] Lange, O. F. & Grubmüller, H. Collective langevin dynamics of conformational motions in proteins. *The Journal of Chemical Physics* **124** (2006).

[128] Abraham, M. J. *et al.* Gromacs: High performance molecular simulations through multi-level parallelism from laptops to supercomputers. *SoftwareX* **1-2**, 19 – 25 (2015).

[129] Oostenbrink, C., Villa, A., Mark, A. E. & Van Gunsteren, W. F. A biomolecular force field based on the free enthalpy of hydration and solvation: The gromos force-field parameter sets 53a5 and 53a6. *Journal of Computational Chemistry* **25**, 1656–1676 (2004).

[130] Dang, L. X. Mechanism and thermodynamics of ion selectivity in aqueous solutions of 18-crown-6 ether: A molecular dynamics study. *Journal of the American Chemical Society* **117**, 6954–6960 (1995).

[131] Malde, A. K. *et al.* An automated force field topology builder (atb) and repository: Version 1.0. *Journal of Chemical Theory and Computation* **7**, 4026–4037 (2011).

[132] Gubbins, K. E., Bhatia, K. K. & Walker, R. D. Diffusion of gases in electrolytic solutions. *AIChE Journal* **12**, 548–552 (1966).

[133] Schulz, J. C. F., Schlaich, A., Heyden, M., Netz, R. R. & Kappler, J. Non-newtonian viscous behavior of water at high frequencies (2018). In preparation.

[134] Haynes, W. M. *CRC handbook of chemistry and physics* (CRC press, 2014).

[135] Mahoney, M. W. & Jorgensen, W. L. Diffusion constant of the tip5p model of liquid water. *The Journal of Chemical Physics* **114**, 363–366 (2001).

[136] Mark, P. & Nilsson, L. Structure and dynamics of the tip3p, spc, and spc/e water models at 298 k. *The Journal of Physical Chemistry A* **105**, 9954–9960 (2001).

[137] Halle, B. & Davidovic, M. Biomolecular hydration: from water dynamics to hydrodynamics. *Proceedings of the National Academy of Sciences* **100**, 12135–12140 (2003).

[138] Cheng, N.-S. Formula for the viscosity of a glycerol-water mixture. *Industrial & Engineering Chemistry Research* **47**, 3285–3288 (2008).

[139] Schultz, S. G. & Solomon, A. K. Determination of the effective hydrodynamic radii of small molecules by viscometry. *The Journal of General Physiology* **44**, 1189–1199 (1961).

[140] Hayduk, W. & Laudie, H. Prediction of diffusion coefficients for nonelectrolytes in dilute aqueous solutions. *AIChE Journal* **20**, 611–615 (1974).

[141] de Gennes, P.-G. *Scaling Concepts in Polymer Physics* (Cornell University Press, Ithaca, N.Y, 1979).

[142] Hansen, P. M., Bhatia, V. K., Harrit, N. & Oddershede, L. Expanding the Optical Trapping Range of Gold Nanoparticles. *Nano Lett.* **5**, 1937–1942 (2005).

[143] Balazs, A. C., Emrick, T. & Russell, T. P. Nanoparticle polymer composites: Where two small worlds meet. *Science* **314**, 1107–1110 (2006).

[144] Lee, C. T. *et al.* Simulation-based approaches for determining membrane permeability of small compounds. *Journal of Chemical Information and Modeling* **56**, 721–733 (2016).

[145] Murata, K. *et al.* Structural determinants of water permeation through aquaporin-1. *Nature* **407**, 599–605 (2000).

[146] Verkman, A. *et al.* Water transport across mammalian cell membranes. *American Journal of Physiology-Cell Physiology* **270**, C12–C30 (1996).

[147] Fettiplace, R. & Haydon, D. Water permeability of lipid membranes. *Physiological Reviews* **60**, 510–550 (1980).

[148] Paula, S., Volkov, A., Van Hoek, A., Haines, T. & Deamer, D. W. Permeation of protons, potassium ions, and small polar molecules through phospholipid bilayers as a function of membrane thickness. *Biophysical journal* **70**, 339–348 (1996).

[149] Mathai, J. C., Tristram-Nagle, S., Nagle, J. F. & Zeidel, M. L. Structural determinants of water permeability through the lipid membrane. *The Journal of General Physiology* **131**, 69–76 (2008).

[150] Schulz, R. *et al.* Data-based modeling of drug penetration relates human skin barrier function to the interplay of diffusivity and free-energy profiles. *Proceedings of the National Academy of Sciences* **114**, 3631–3636 (2017).

[151] Zuckerman, D. M. & Woolf, T. B. Transition events in butane simulations: Similarities across models. *J. Chem. Phys.* **116**, 2586–2591 (2002).

[152] Kou, S. & Xie, X. S. Generalized langevin equation with fractional gaussian noise: subdiffusion within a single protein molecule. *Physical Review Letters* **93**, 180603 (2004).

[153] Mamonov, A. B., Kurnikova, M. G. & Coalson, R. D. Diffusion constant of k+ inside gramicidin a: A comparative study of four computational methods. *Biophysical Chemistry* **124**, 268 – 278 (2006). Ion Hydration Special Issue.

[154] Min, W., Luo, G., Cherayil, B. J., Kou, S. C. & Xie, X. S. Observation of a power-law memory kernel for fluctuations within a single protein molecule. *Phys. Rev. Lett.* **94**, 198302 (2005).

[155] Wong-Ekkabut, J. *et al.* Computer simulation study of fullerene translocation through lipid membranes. *Nature Nanotechnology* **3**, 363–368 (2008).

[156] Abraham, M. J. *et al.* Gromacs: High performance molecular simulations through multi-level parallelism from laptops to supercomputers. *SoftwareX* **1-2**, 19 – 25 (2015).

[157] Loison, C. Hydrated DPPC, MD simulation trajectory and related files for UA charmm36 model by Lee et al 2014 (2015).

[158] Abascal, J. L. F. & Vega, C. A general purpose model for the condensed phases of water: Tip4p/2005. *The Journal of Chemical Physics* **123**, 234505 (2005).

[159] Frenkel, D. & Smit, B. Chapter 7 - free energy calculations. In Frenkel, D. & Smit, B. (eds.) *Understanding Molecular Simulation (Second Edition)*, 167 – 200 (Academic Press, San Diego, 2002), second edition edn.

[160] Kumar, S., Rosenberg, J. M., Bouzida, D., Swendsen, R. H. & Kollman, P. A. The weighted histogram analysis method for free-energy calculations on biomolecules. i. the method. *Journal of Computational Chemistry* **13**, 1011–1021 (1992).

[161] Schatzberg, P. Solubilities of water in several normal alkanes from c7 to c161. *The Journal of Physical Chemistry* **67**, 776–779 (1963).

[162] Zhu, T., Li, J., Hawkins, G. D., Cramer, C. J. & Truhlar, D. G. Density functional solvation model based on cm2 atomic charges. *The Journal of Chemical Physics* **109**, 9117–9133 (1998).

[163] von Hansen, Y., Sedlmeier, F., Hinczewski, M. & Netz, R. R. Friction contribution to water-bond breakage kinetics. *Phys. Rev. E* **84**, 051501 (2011).

[164] von Hansen, Y., Gekle, S. & Netz, R. R. Anomalous anisotropic diffusion dynamics of hydration water at lipid membranes. *Phys. Rev. Lett.* **111**, 118103 (2013).

[165] Marrink, S. J., Sok, R. M. & Berendsen, H. J. C. Free volume properties of a simulated lipid membrane. *The Journal of Chemical Physics* **104**, 9090–9099 (1996).

[166] Morgado, R., Oliveira, F. A., Batrouni, G. G. & Hansen, A. Relation between anomalous and normal diffusion in systems with memory. *Phys. Rev. Lett.* **89**, 100601 (2002).

[167] Indei, T., Schieber, J. D., Córdoba, A. & Pilyugina, E. Treating inertia in passive microbead rheology. *Phys. Rev. E* **85**, 021504 (2012).

[168] Biltonen, R. L. A statistical-thermodynamic view of cooperative structural changes in phospholipid bilayer membranes: their potential role in biological function. *The Journal of Chemical Thermodynamics* **22**, 1 – 19 (1990).

[169] Hinz, H.-J. & Sturtevant, J. M. Calorimetric studies of dilute aqueous suspensions of bilayers formed from synthetic l-α-lecithins. *Journal of Biological Chemistry* **247**, 6071–6075 (1972).

[170] Blume, A. Apparent molar heat capacities of phospholipids in aqueous dispersion. effects of chain length and head group structure. *Biochemistry* **22**, 5436–5442 (1983).

[171] Marsh, D. General features of phospholipid phase transitions. *Chemistry and physics of lipids* **57**, 109–120 (1991).

[172] Sun, W., Tristram-Nagle, S., Suter, R. & Nagle, J. Structure of gel phase saturated lecithin bilayers: temperature and chain length dependence. *Biophysical journal* **71**, 885–891 (1996).

Abstract

Permeation processes of molecules through lipid bilayers have a high physiological relevance, and a theoretical description of such processes is essential for the understanding of transport mechanisms of drugs in human tissue. In experiments, only integrated permeation coefficients of membranes are accessible, hence computer simulations are necessary to obtain a position–resolved picture of molecular permeation. Since the bilayer interior is a highly viscous medium, the time scales of both the lipid relaxation and the molecule motion overlap, which induces memory effects to the molecule dynamics. The aim of this thesis is the analysis of the modifications of current models for the passive permeation if memory effects are considered.

Since the lipid phase significantly determines the permeability of lipid membranes, we begin with a comparison of the hydration repulsion between membranes in the gel and fluid phase. We show that inconsistencies between experimental data from literature disappear if the interaction pressures are plotted as a function of the repeat distance instead of the water layer thickness. Subsequently, we compare our simulations to the converted experimental data and obtain quantitative agreement. We observe that the decay length of the hydration pressure in the gel phase is by a factor of two smaller than in the fluid phase. A decomposition of the hydration pressures into membrane–membrane interactions and water-mediated interactions reveals that these two contributions have opposite signs and are one order of magnitude larger than their sum. We conclude that in both phases the hydration repulsion is a result of a subtle interplay between the direct attraction of membranes and a slightly stronger water-mediated repulsion.

In the second part we perform simulations of five different molecules in water, which we confine by harmonic potentials. We modified an existing iterative method from literature for the extraction of memory kernels from trajectories and applied it to compute the friction coefficients of the molecules. We observe that for all molecules the friction increases with the confinement strength due to changes in the long time tail of the memory kernel. The increase of the friction is amplified in water–glycerol mixtures as solvent, which are more viscous than pure water. This result is explained by a dynamic coupling between the solvent relaxation and the molecule diffusion, which emerges when both processes proceed on the same time scale.

In the last part we compute the permeation coefficient of water through a lipid membrane. We first determine the free energy and diffusivity profiles of water inside the membrane using a description of the water dynamics based on the memoryless Fokker-Planck equation. We then apply our method developed in part two to calculate the memory kernels of water inside the membrane. The resulting diffusion coefficients are compared to the memoryless model and to literature values from simulations, yielding a reduction of the diffusivity by a factor of up to 20 in the membrane interior when memory effects are considered. This indicates that both the free energy as well as the diffusivity are equally important for the permeation process.

Kurzfassung

Permeationsprozesse von Molekülen durch Lipiddoppelschichten sind von hoher physiologischer Relevanz, und eine theoretische Beschreibung solcher Prozesse ist essentiell für das Verständnis von Transportmechanismen von Medikamenten in menschlichem Gewebe. Für ein ortsaufgelöstes Bild molekularer Permeation sind Computersimulationen notwendig, da experimentell nur integrierte Permeationskoeffizienten messbar sind. Aufgrund der hohen Viskosität im Inneren der Doppelschichten besteht ein Überlapp zwischen den Zeitskalen der Lipidrelaxation und der Molekülbewegung, was Memory-Effekte in der Moleküldynamik erzeugt. Das Ziel dieser Dissertation ist eine Analyse der Konsequenzen für die derzeitigen Modelle der passiven Permeation bei der Berücksichtigung der Memory-Effekte.

Die Permeabilität von Lipidmembranen ist in erheblichem Maße durch die Lipidphase bestimmt, daher beginnen wir mit einem Vergleich der Hydrationsrepulsion zwischen Membranen in der Gel- und der Flüssigphase. Wir zeigen, dass Inkonsistenzen zwischen experimentellen Daten aus der Literatur verschwinden, wenn der Wechselwirkungsdruck als Funktion des Wiederholungsabstandes anstatt der Wasserschichtdicke dargestellt wird. Ein Vergleich unserer Simulationen mit den konvertierten experimentellen Daten ergibt quantitative Übereinstimmung. Wir beobachten, dass die Zerfallslänge des Hydrationsdrucks in der Gelphase um den Faktor zwei kleiner ist als in der Flüssigphase. Eine Aufspaltung des Hydrationsdrucks in eine Membran–Membran Wechselwirkung und eine vom Wasser vermittelte Wechselwirkung offenbart, dass beide Beiträge ein entgegengesetztes Vorzeichen besitzen und um eine Größenordnung größer sind als ihre Summe. Daraus folgern wir, dass die Hydrationsrepulsion in beiden Phasen ein Ergebnis eines subtilen Wechselspiels zwischen einer direkten Attraktion der Membranen und einer leicht stärkeren, vom Wasser vermittelten Repulsion ist.

Im zweiten Teil führen wir Simulationen von fünf verschiedenen Molekülen, die in harmonische Potentiale einsperrt sind, in Wasser durch. Wir modifizieren eine iterative Methode aus der Literatur zur Extraktion der Memory-Kernel aus Trajektorien und wenden diese zur Berechnung der Reibungskonstanten an. Wir beobachten, dass die Reibung für alle Moleküle mit der Potentialstärke zunimmt, verursacht durch Veränderungen im Langzeitverhalten der Memory-Kernel. Die Zunahme der Reibung verstärkt sich in Wasser–Glyzerin-Mischungen als Lösungsmittel, welche eine höhere Viskosität als reines Wasser aufweisen. Dieses Ergebnis wird durch eine dynamische Kopplung der Lösungsmittelrelaxation und der Moleküldiffusion erklärt, die hervortritt, wenn beide Prozesse auf der gleichen Zeitskala ablaufen.

Im letzten Teil berechnen wir den Permeationskoeffizienten von Wasser durch eine Lipidmembran. Mit Hilfe einer Beschreibung der Wasserdynamik basierend auf der memorylosen Fokker-Planck-Gleichung bestimmen wir das Profil der Freien Energie und der Diffusivität von Wasser innerhalb der Lipidmembran. Im Anschluß verwenden wir unsere Methode aus dem zweiten Teil zur Berechnung der Memory-Kernel des Wassers innerhalb der Membran. Die resultierenden Diffusionskoeffizienten vergleichen wir mit dem memorylosen Modell und mit Literaturwerten aus Simulationen, was eine Abnahme der Diffusivität um einen Faktor von bis zu 20 im Inneren der Membran aufzeigt, wenn Memory-Effekte berücksichtigt werden. Dies deutet darauf hin, dass die Freie Energie und die Diffusivität einen gleichwertigen Einfluss auf Permeationsprozesse haben.

Hiermit erkläre ich, dass ich die vorliegende Dissertationsschrift mit dem Titel

Memory Effects in the Permeation of Molecules through Lipid Bilayers

selbständig angefertigt und hierfür keine anderen als die angegebenen Hilfsmittel verwendet habe. Die Arbeit ist weder in einem früheren Promotionsverfahren angenommen noch als ungenügend beurteilt worden.

Berlin, den 25. Januar 2018

Danksagung

An dieser Stelle möchte ich mich bei all denjenigen bedanken, die mich während meiner Promotion unterstützt haben. Ein besonderer Dank gilt meinem Doktorvater, Herrn Prof. Dr. Roland Netz, der mir das Erstellen dieser Arbeit ermöglichte, mir in meiner Forschung viel Freiraum gelassen hat und mich trotzdem mit seinen Ratschlägen aus vielen wissenschaftlichen Sackgassen geführt hat.

Ein großer Dank gebührt auch Emanuel Schneck, Matej Kanduč und vor allem meinem langjährigen Bürokollegen Alexander Schlaich, die mir besonders in der Anfangszeit bei vielen physikalischen, aber auch technischen Problemen unter die Arme gegriffen haben und mit denen ich während eines großen Teils meiner Promotion zusammenarbeiten durfte.

Ein weiterer besonderer Dank gilt Jan Daldrop, der nicht nur ein Kollege war, mit dem ich anregende wissenschaftliche Diskussionen führen konnte, sondern mich auch bei sich in die Wohnung aufnahm und somit ein Mitbewohner und guter Freund wurde.

Auch allen anderen Mitgliedern der AG Netz möchte ich für das herausragende Arbeitsklima und das hohe Fachwissen danken, dass sie mit mir geteilt haben, dabei insbesondere Julian Kappler und Robert Schulz, die mich oft bei mathematischen Fragestellungen beraten haben.

Vor allem danke ich aber meinen Eltern und meinem Bruder Jakob, die mich seit jeher auf jede erdenkliche Art und Weise unterstützen und ohne die ich den Schritt in die Wissenschaft nicht geschafft hätte.